University of Bath

PHD

Atomistic Modelling Studies of Fluorite- and Perovskite-Based Oxide Materials

Stokes, Stephen

Award date:
2010

Awarding institution:
University of Bath

Link to publication

General rights
Copyright and moral rights for the publications made accessible in the public portal are retained by the authors and/or other copyright owners and it is a condition of accessing publications that users recognise and abide by the legal requirements associated with these rights.

- Users may download and print one copy of any publication from the public portal for the purpose of private study or research.
- You may not further distribute the material or use it for any profit-making activity or commercial gain
- You may freely distribute the URL identifying the publication in the public portal ?

Take down policy
If you believe that this document breaches copyright please contact us providing details, and we will remove access to the work immediately and investigate your claim.

Download date: 23. May. 2019

Atomistic Modelling Studies of Fluorite- and Perovskite-Based Oxide Materials

Submitted by

Stephen James Stokes

for the degree of Doctor of Philosophy of the

University of Bath

Department of Chemistry

July 2010

Copyright

Attention is drawn to the fact that the copyright of this thesis rests with its author. This copy of the thesis has been supplied on condition that anyone who consults it is understood to recognise that its copyright rests with its author and that no quotation from the thesis and no information derived from it may be published without the prior written consent of the author.

Restrictions

This thesis may be made available for consultation within the University Library and may be photocopied or lent to other libraries for the purposes of consultation.

Signature of author: .....

Dedication

I dedicate this thesis to my family, which includes my partner Keeley, son Andrew, parents Frank and Susan, brother Jonathan and sister Hannah. Without their love and support, reaching for this level would have been a far more difficult task.

Acknowledgements

I would like to thank my supervisor, Prof. Saiful Islam, for his continued support, advice and patience throughout the duration of my Ph.D studies. I would like to thank the EPSRC for providing the funding for this study. I would also like to thank my colleagues who have helped during this work. In particular, Dr. Craig Fisher, who helped me understand the computational theory and techniques during the first half of this work. I would also like to thank Dr Pooja Panchmatia, Paul Weaver and Grahame Gardiner for their useful discussions regarding not only my own work, but their own, that allowed me to develop my knowledge of this field of chemistry.

Abstract

Fast oxide-ion and proton conductors are the subject of considerable research due to their technological applications in sensors, ceramic membranes and solid oxide fuel cells (SOFCs). This thesis describes the use of computer modelling techniques to study point defects, dopants and clustering effects in fluorite- and perovskite-type ion conductors with potential SOFC applications. Bi_2O_3 related phases are being developed with the objective of high oxide-ion conductivities at lower operating temperatures than 1000°C, as in current generation SOFC electrolytes. Doped Bi_2O_3 phases have shown promise as materials capable of accomplishing this goal. First, the Y-doped phase, Bi_3YO_6, has been investigated including the ordering of intrinsic vacancies. The defect and dopant characteristics of Bi_3YO_6 have been examined and show that a highly mobile oxygen sub-lattice exists in this material. A preliminary structural modelling study of a new Re-doped Bi_2O_3 phase was also undertaken. A comprehensive investigation of the proton-conducting perovskites $BaZrO_3$, $BaPrO_3$ and $BaThO_3$ is then presented. Our results suggest that intrinsic atomic disorder in $BaZrO_3$ and $BaThO_3$ is unlikely, but reduction of Pr^{4+} in $BaPrO_3$ is favourable. The water incorporation energy is found to be less exothermic for $BaZrO_3$ than for $BaPrO_3$ and $BaThO_3$, but in all cases the results suggest that the proton concentration would decrease with increasing temperature, in accord with experimental data. The high binding energies for all the dopant-OH pair clusters in $BaPrO_3$ and $BaThO_3$ suggest strong proton trapping effects. Finally, a study of multiferroic $BiFeO_3$ is presented, in which the defect, dopant and migration properties of this highly topical phase are investigated. The reduction process involving the formation of oxygen vacancies and Fe^{2+} is the most favourable redox process. In addition, the results suggest that oxide-ion migration is anisotropic within this system.

Publications and Presentations

(A) Publications

1. **S J Stokes**, M S Islam, 'Defect Chemistry and Proton Dopant Association in $BaZrO_3$ and $BaThO_3$', *J. Mater. Chem.*, **20**, 6528 (2010) [**Appendix C**]

2. I Abrahams, X Liu, S Hull, S T Norberg, A Kozanecka-Szmigiel, F Krok, M S Islam, **S J Stokes**, 'A Combined Total Scattering and Simulation Approach to Analysing Defect Structure in Bi_3YO_6' *Chem. Mater.*, **22**, 4435 (2010) [**Appendix D**]

3. **S J Stokes**, M S Islam, 'Structural and Defect Properties of $BiFeO_3$' *Adv. Funct. Mater., to be submitted (2010)*

4. **S J Stokes**, M S Islam, 'Dopants and Defect Clustering in Bi_3YO_6, *in preparation*

(B) Presentations - Talks

1. RSC Solid State Chemistry Group Christmas Meeting, Open University, Milton Keynes, UK (Dec 2009) *'Bismuth-Oxide and Perovskite Ionic Conductors : Atomic Scale Insight into Defect Properties'*

2. Postgraduate Final Year Symposium, University of Bath, UK (May 2009) *'Atomistic Modelling of New Ion Conductors for Solid Oxide Fuel Cells'* **Best Talk Prize Winner**

3. 2nd Year Talks Program, University of Bath, UK (Nov 2007) *'Atomistic Modelling of New Fluorite-based Bismuth Oxides'*

(C) Presentations - Posters

1. Workshop on SOFCs: Materials and Technology, Albacete, Spain (Nov 2009) *'Defects, Dopants and Water Incorporation in Bismuth Oxide and Perovskite-*

type Ionic Conductors'

2. Solid State Ionics 17, Toronto, Canada (Jun 2009) *'Structural and Defect Characteristics of Bismuth-Oxide Based Ionic Conductors'*

3. The Royal Society - Energy Materials to Combat Climate Change, London, UK (Jun 2009) *'Atomic-Scale Insight into New Ion Conductors for Solid Oxide Fuel Cells'*

4. RSC Solid State Group Christmas Meeting 2008, University of Southampton, UK (Dec 2008) *'Structural and Defect Properties of Bismuth-Oxide Based Oxide-Ion Conductors'*

5. C. Greaves Solid State Chemistry Symposium, University of Birmingham, UK (Apr 2008) *'Structural and Defect Properties of Bismuth-Oxide Based Oxide-Ion Conductors'*

6. RSC Solid State Annual Conference 2008, UCL, London, UK (Jun 2008) *'Structural and Defect Characteristics of Bismuth-Oxide Based Oxide-Ion Conductors'*

7. RSC Solid State Group Christmas Meeting 2007, University of Durham, UK (Dec 2007) *'Structural and Defect Characteristics of Bismuth-Oxide Based Oxide-Ion Conductors'*

8. RSC Solid State Group Annual Conference 2007, UCL, London, UK (Jun 2007) *'Structural and Defect Characteristics of Bismuth-Oxide Based Oxide-Ion Conductors'*

Contents

Chapter 1

Introduction

1.1 Background

One of the major challenges in the twenty-first century is the development of cleaner, sustainable sources of energy. With ever increasing environmental and political pressure to cut carbon emissions and to meet energy demand, alternatives to our current energy production technologies are required. Alternative energy systems are also crucial in order to deal with the environmental threat of global warming [1] and declining reserves of fossil fuels. But there is no one universal solution. There is a range of energy conversion and storage technologies, including fuel cells, lithium batteries and solar cells, which are being developed to help cut carbon emissions. The efficiency and commercial viablity of these technologies are dependant upon the properties of the component materials, and therefore the developement of new materials is crucial [2].

A promising "green" technology is the fuel cell. There are many types of fuel cell that have a number of uses, from handheld portable devices and transport power solutions, to full scale power station electricity generation. A fuel cell system that is attracting considerable attention due to its multipurpose nature is the solid oxide fuel cell (SOFC) due to the high efficiency and fuel flexibility [3–15]. Within an SOFC, the solid oxide electrolyte that gives the fuel cell its name is of critical importance. The electrolyte is usually made of an electroceramic material that allows fast ionic conduction, specifically of oxide-ions or protons, but inhibits electronic conduction. Fast oxide ion conductors are important not only for their role in SOFCs, but also as ceramic membranes within ceramic oxygen generators (COGs). In both cases the electroceramic material has increased ion conduction as temperature increases. Most conventional solid electrolytes have operating temperatures of near to 1300K. Reducing this operating temperature without a loss of ion conductance (perhaps through the discovery of new fast ionic conductors) would allow SOFCs to become more commonplace. Most recent studies have been concerned with the two main structure types of solid electrolyte: those based upon the

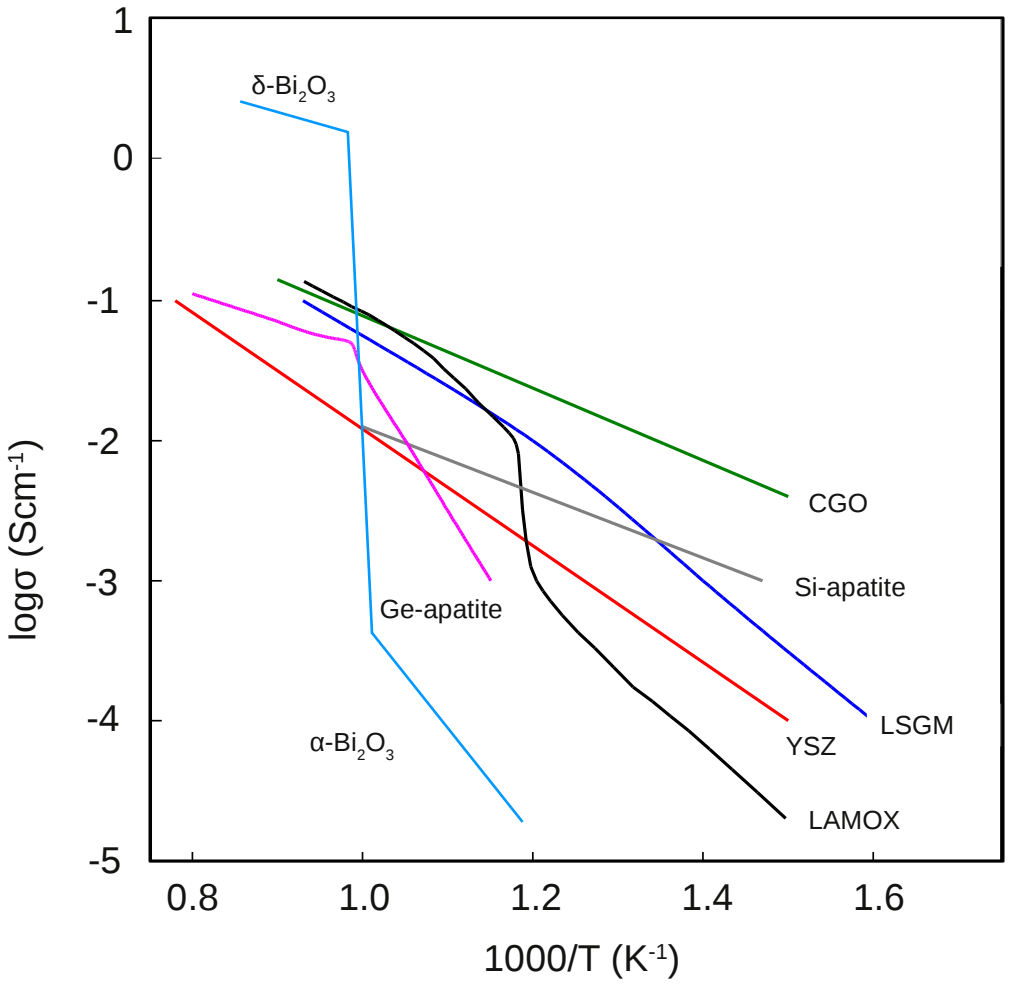

Figure 1.1: Temperature dependence of ion conductivity for various fast oxygen ion conductors: Bi_2O_3 YSZ, $(ZrO_2)_{0.92}(Y_2O_3)_{0.08}$; CGO, $Ce_{0.8}Gd_{0.2}O_{1.9}$; LSGM, $La_{0.9}Sr_{0.1}Ga_{0.8}Mg_{0.2}O_{2.85}$; LAMOX, $La_2Mo_2O_9$; Si-apatite, $La_{10}(SiO_4)_6O_3$ and Ge-apatite, $La_{10}(GeO_4)_6O_3$, from Malavasi et al. [16]

fluorite structure, such as Y_2O_3 doped ZrO_2, and those based upon the perovskite structure, such as strontium and magnesium doped $LaGaO_3$.

Figure 1.1 shows a plot comparing the oxide-ion conductivity with varying temperature of common fast oxide-ion conductors, from which we can see that the Bi_2O_3-based fast ion oxide conductors have the potential to exhibit higher conductivities at lower temperatures if the delta phase is stabilised, which is discussed in greater detail in chapter 3.

Proton conductors have more applications than just SOFCs, such as gas sensors,

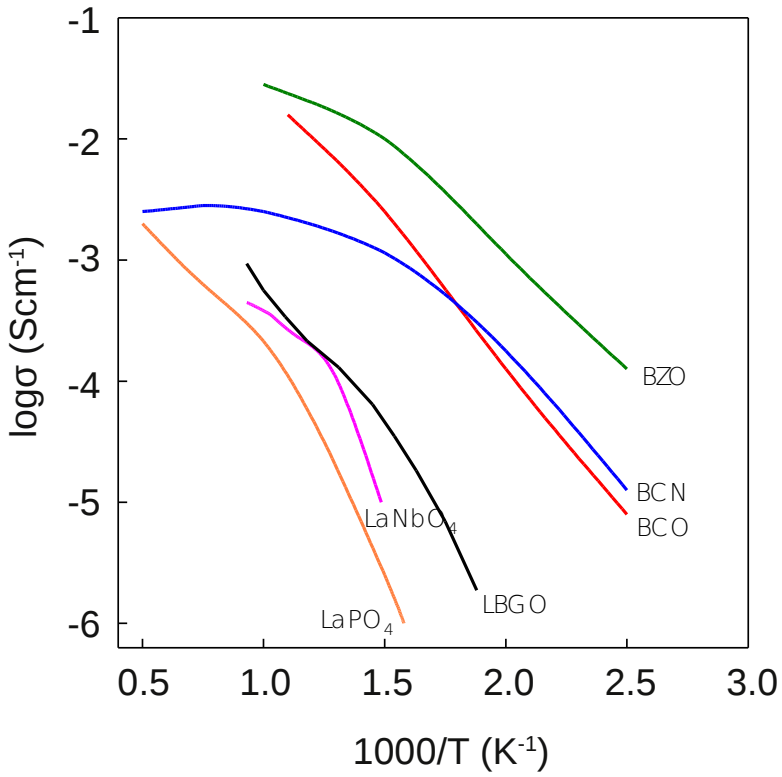

Figure 1.2: Temperature dependence of ion conductivity for various protonic conductors: 10 mol% Y-doped $BaCeO_3$ (BCO); 20 mol% Y-doped $BaZrO_3$ (BZO); 10% Sr-doped $LaPO_4$; $Ba_3Ca_{1.18}Nb_{1.82}O_{8.73}$ (BCN); 1 mol% Ca-doped $LaNbO_4$; $La_{0.8}Ba_{1.2}GaO_{3.9}$ (LBGO) from [16].

mixed conducting membranes for hydrogen separation and solid oxide electrolyser cells (SOECs). Proton conduction in ABO_3 perovskites was discovered by Iwahara et al. [17] in 1981 and has since attracted great attention. By comparing the proton conductivity of some well known proton conductors in Figure 1.2, we can see that barium perovskites ($BaZrO_3$ and $BaCeO_3$) show some of the highest proton-conductivities and are worthy of further investigation.

The role of materials science is fundamental for discovering and developing new materials that support good ion conductivities at lower temperatures, together with improved chemical stability and sinterability. Such breakthroughs underpin applied research, and depend simultaneously upon exploring new classes of compounds and gaining a better understanding of the structural, defect and mechanistic features of fast-ion conductors at the atomic level.

Intense research in this field, has led to the discovery of several new classes of materials with excellent ion conducting properties, which in some cases exhibit different conduction mechanisms than the vacancy-mediated transport of well-known oxide-ion conductors such as yttria-stabilized zirconia (YSZ) [18–23]. This has triggered a vast amount of research aimed not only at improving performance but also at understanding phenomena on a fundamental level by experimental and theoretical methods.

1.2 Solid Oxide Fuel Cells

One leading technology for future power generation is the fuel cell. These are electrochemical devices which convert chemical energy into electricity and, in the simplest case, are based on the reduction/oxidation reactions between hydrogen and oxygen, at the electrodes to produce water. Fuel cells are made up of two electrodes (cathode and anode) separated by an electrolyte, with the two electrodes attached to an external circuit (shown in Figure 1.3). The role of the anode is to oxidise fuel with the aid of a catalyst. The aim of the electrolyte, be it polymer or ceramic-based, is to conduct ions between the electrodes to complete the circuit, but not to conduct electrons. This means that the only route to the positively charged cathode is through the external circuit, creating electron flow. To complete the circuit an oxidant must be added at the cathode; this is then reduced using the electrons from the external circuit.

As noted, SOFCs use oxide ions or protons as the charge carrier within a solid oxide (ceramic) electrolyte. The oxide-ion SOFC uses H_2 and CO as its fuel at the anode and O_2 as the oxidant at the cathode. Hydrocarbons can also be used as a fuel source making SOFCs an ideal "bridging" technology from the hydrocarbon economy to a hydrogen infrastructure. The reactions that occur in the oxide-ion

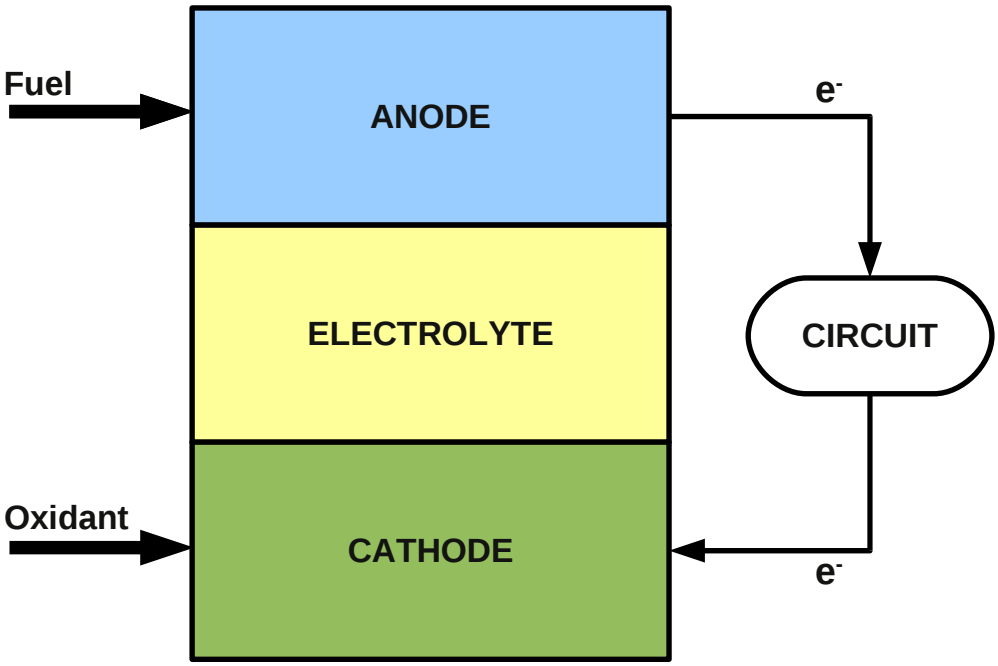

Figure 1.3: General schematic of a fuel cell.

conducting fuel cell are as follows:

$$\textbf{Anode:} \quad \mathrm{CO} + \mathrm{H_2O} \rightarrow \mathrm{CO_2} + \mathrm{H_2} \tag{1.1}$$

$$\textbf{Anode/Electrolyte Boundary:} \quad \mathrm{O^{2-}} + \mathrm{H_2} \rightarrow \mathrm{H_2O} + 2\,\mathrm{e^-} \tag{1.2}$$

$$\textbf{Cathode:} \quad \mathrm{O_2} + 4\,\mathrm{e^-} \rightarrow 2\,\mathrm{O^{2-}} \tag{1.3}$$

$$\textbf{Overall Reactions:} \quad \mathrm{H_2} + \tfrac{1}{2}\mathrm{O_2} \rightarrow \mathrm{H_2O} \tag{1.4}$$

$$\mathrm{CO} + \tfrac{1}{2}\mathrm{O_2} \rightarrow \mathrm{CO_2} \tag{1.5}$$

As fuel is added more oxide ions are removed from the electrolyte and are oxidised, releasing electrons into the anode. This process promotes the flow of oxide-ions across the electrolyte. The electrons (from oxidisation) are then required at the cathode to reduce O_2 to oxide ions. The only route these electrons can take is via an external circuit as the electrolyte is an electronic insulator. This flow of electrons in the external circuit provides electrical energy. These processes are illustrated in Figure 1.4.

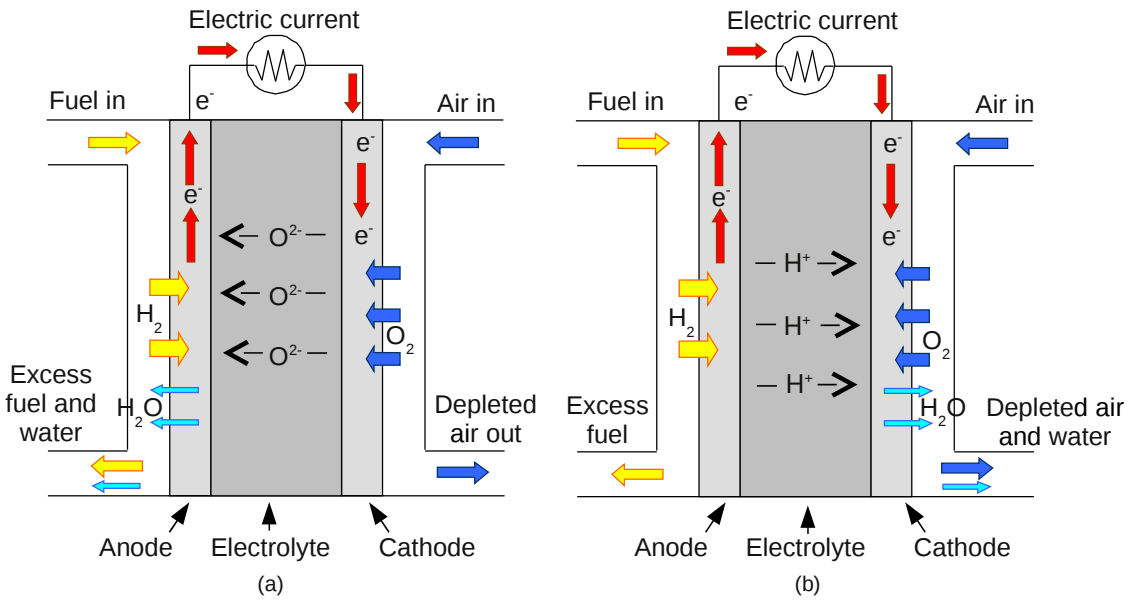

Figure 1.4: Schematic diagram of the processes taking place in a solid oxide fuel cell (SOFC) during operation; (a) oxide-ion conducting electrolyte, and (b) proton conducting electrolyte. A key advantage of SOFCs is that they also allow hydrocarbons to be used as a fuel source. from [16]

The proton-conducting SOFC uses hydrogen as the fuel at the anode and oxygen at the cathode [24, 25]. In this case the reactions are:

$$\textbf{Anode:} \qquad 2\,H_2 \rightarrow 4\,H^+ + 4\,e^- \tag{1.6}$$

$$\textbf{Cathode:} \qquad O^{2-} + 4\,H^+ + 4\,e^- \rightarrow 2\,H_2O \tag{1.7}$$

$$\textbf{Overall Reactions:} \qquad 2\,H_2 + O_2 \rightarrow 2\,H_2O \tag{1.8}$$

Hydrogen in the anode is broken down into its constituent protons and electrons. At the cathode O_2 is reduced and reacts with protons from the electrolyte to form waste water. This in turn creates a flow of protons through the electrolyte. Through these processes a potential difference is created across the external circuit and when connected electrons flow from the anode to the cathode. These processes are shown in Figure 1.4.

This thesis is not intended to provide a comprehensive review of fuel cell technology as excellent reviews on SOFCs can be found elsewhere [3–7, 16, 26, 27].

1.2.1 Electrodes and Interconnect

Both the anode and cathode are porous to allow the relevant gases to reach their reaction sites at the electrode-electrolyte interface, and to allow waste gases to leave the fuel cell. The cathode of an SOFC needs to have high electronic conductivity under oxidising conditions and a good catalytic activity toward promoting oxygen dissociation. The traditional materials for cathodes are perovskites based on $LaMnO_3$ and $LaCoO_3$ [28]. In lanthanum manganate the p-type electronic conductivity arises from mixed valence Mn (Mn^{3+}/Mn^{4+}), which is improved by doping with alkaline earth metals, notably Sr [29, 30]. A drawback to $La_{1-x}Sr_xMnO_3$ (LSM) is that it has poor oxide ion conduction, which limits the redox reactions to the triple phase boundary. It is desirable to have ionic conduction within the cathode to allow reactions to occur deeper in the cathode. The analogous cobalt phase $La_{1-x}Sr_xCoO_3$ (LSC) offers improved cathode performance due to increased oxide-ion conductivity and catalytic activity. A more detailed summary of perovskite materials for cathode applications can be found in a comprehensive review by Skinner [31].

An anode material must be able to remain stable at high temperatures and in the highly reducing atmosphere created by the fuel gases. A candidate material must also be able to catalyse the relevant reaction that occurs within its structure, which in the case of the anode is the oxidisation of the fuel. Traditionally, the most widely used anodes for SOFCs consist of a metallic component dispersed into a matrix of the electrolyte material. The operating conditions of the SOFC usually limit the choice of metals to Co, Ni, Pt and Ru, with Ni being the current choice [32]. However, a metal alone would not be porous enough at sustained high temperatures to function as an anode. For the current generation of SOFCs, where YSZ is the electrolyte, the anode is usually made up of Ni and YSZ to create a porous metal network.

Another important component of a fuel cell system is the interconnect that links

individual fuel cells to allow creation of fuel cell series and then stacks. This is usually metallic or ceramic based, such as $LaCrO_3$ [33]. The interconnect is used to separate reactant gases from both the anode and cathode and as such is exposed to both reductive and oxidative atmospheres at high temperatures, meaning that the material used must be very stable, making a metallic interconnect less attractive.

The major issue with current generation SOFCs is the high operating temperatures required for the electrolytes to carry sufficient ionic flux, which limits the choice of materials for the other components within the fuel cell. A decrease in the operating temperatures from near 1270K to closer to 870K would allow the use of more cost effective and efficient materials for the electrodes and interconnects.

1.2.2 Electrolyte

The electrolyte is a key element of the SOFC and requires high ion conductivity. The drawback of current solid electrolyte materials is that high ionic conductivity usually occurs at high temperatures (870-1370K). These high temperatures have to be taken into account when choosing materials for all other components within the SOFC. The other properties that are important for candidate electrolyte materials are that they have to be electronic insulators, as otherwise the cell will be short-circuited; to have high stability at low and high temperatures; and also to have a high density to prevent a chemical short circuiting of gasses passing through the electrolyte. Due to the high operating and processing temperatures it is desirable for all materials that are used in the fuel cell system to have very similar thermal expansion coefficients, as non-matching coefficients can lead to physical failure of the fuel cell, which is a common problem between current generation anode materials and electrolytes.

The two main structure types of SOFC electrolyte are described in the next two sections, as well as the materials studied in this thesis.

1.3 Fluorite-type Oxides

The first generation of solid state ion conductors to be discovered and extensively investigated were fluorite based structures (AO_2) (illustrated in Figure 1.5), where A is a tetravalent cation. The cations occupy face-centred positions (4a wykoff position) in a cubic unit cell with anions in the eight tetrahedral sites (8c wykoff position) between them. Doped CeO_2 and stabilised ZrO_2 are the most commonly used electrolytes. Also, stabilised forms of δ-Bi_2O_3 are of significant interest as these fluorite-related phases show such high oxide-ion conductivity, as mentioned in section 1.1. Pure zirconia is not a good ion conductor and does not adopt the cubic structure below 2300°C [34]. A common procedure in materials development is doping of other cations into the lattice. Acceptor doping is used to stabilise the cubic symmetry of ZrO_2 and to introduce oxygen vacancies (which are required for ion conduction via vacancy hopping) [18, 19, 35]. Substitution of Zr^{4+} ion with a Y^{3+} ion is charge compensated by the formation of highly mobile oxygen vacancies.

It is widely observed that an increase in dopant percentage leads to an increase in ionic conductivity. It has also been shown that as dopant concentration increases ionic conductivity peaks and then decreases [37] (Figure 1.6). A combination of atomistic simulation [38, 39] and experimental studies [40] have shown that strong defect association or clustering occurs between the dopant ions and oxygen vacancies. Early modelling work [38, 39] indicated that a key factor for the interaction between these defects is the elastic strain introduced into the lattice by size mismatch between the dopant and host cation. Recently, however, systematic comparison of conductivities of 10 mol% trivalent cation-doped cerias has suggested that the structure-property relationships are more complex, and that the observed trends in ionic conductivity cannot be explained in terms of minimum elastic strain alone [41].

The role of defects, dopants, and the transport mechanism for ions is very important, and by using computer simulation we can learn more about these atomic-scale

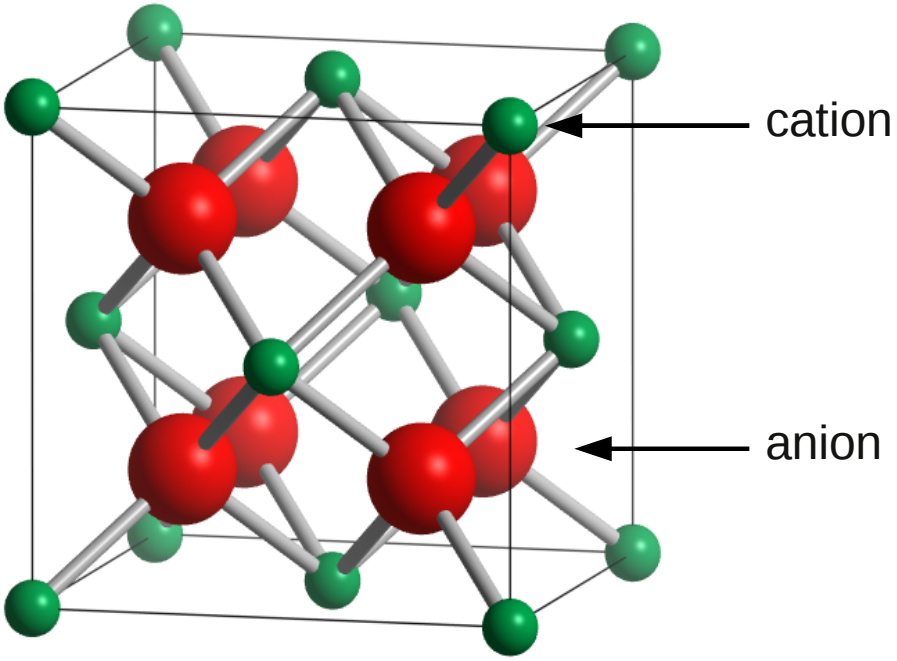

Figure 1.5: Fluorite structure (CaF_2) adopted by ZrO_2. Zr = green, O = red. This figure and many other in this thesis were created using the free graphics software VESTA [36].

properties that shape the macroscopic behaviour of the materials investigated

In section 3.3 we apply atomistic simulation techniques, detailed in chapter 2, to a stabilised δ-Bi_2O_3 phase, Bi_3YO_6, as this phase adopts a fluorite-type structure at room temperature and exhibits fast-ion conduction. We examine the highly debated structural dilemma of intrinsic disorder presented by Bi_3YO_6. We address a range of defects and dopants, including dopants not usually considered experimentally, such as Pb^{2+}. In section 3.4, an attempt is made to model the fluorite-related complex phase, $Bi_{28}Re_2O_{49}$.

1.4 Perovskite-type Oxides

Since the late 1980s-perovskite type ion conductors have been investigated intensively. Perovskites have the general formula ABO_3 where the large A cation is

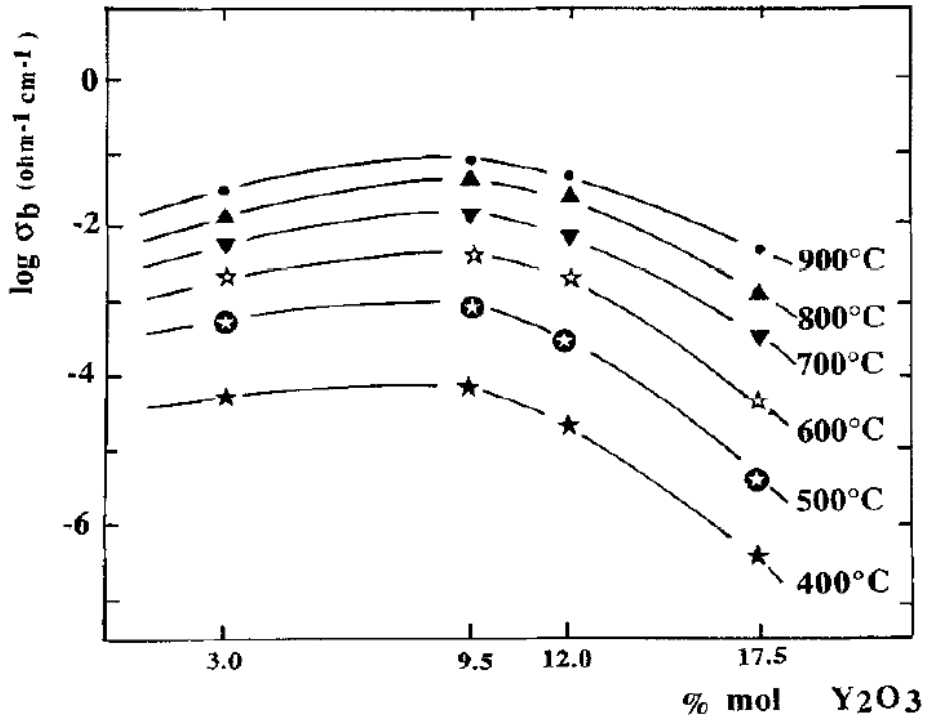

Figure 1.6: Influence of the amount of Y_2O_3, on the ionic conductivity of zirconia single crystals, taken from Filal et al. [37]

coordinated to twelve anions, with the B cation occupying a six coordinate site, forming a network of corner sharing BO_6 octahedra (Figure 1.7). It is usually through distortions of these octahedra that deviations from cubic symmetry occur.

A widely studied perovskite-structured oxide is doped lanthanum gallate, $LaGaO_3$. The high oxide-ion conductivity of (Sr,Mg)-doped $LaGaO_3$ (often termed LSGM) was reported in 1994 by Ishihara et al. [42], and by Feng and Goodenough [43]. This material exhibits pure ionic conductivity over a very wide range of oxygen partial pressures. The majority of proton-conducting oxides are perovskite based. A significant amount of research in the late 1980s focussed upon (Sr/Ba)-doped CeO_3 systems [44, 45].

The perovskite structure has been dubbed an "inorganic chameleon" as the structure displays a rich diversity of chemical compositions and properties. Perovskites are developed for a vast array of electrochemical devices such as sensors, dielectrics,

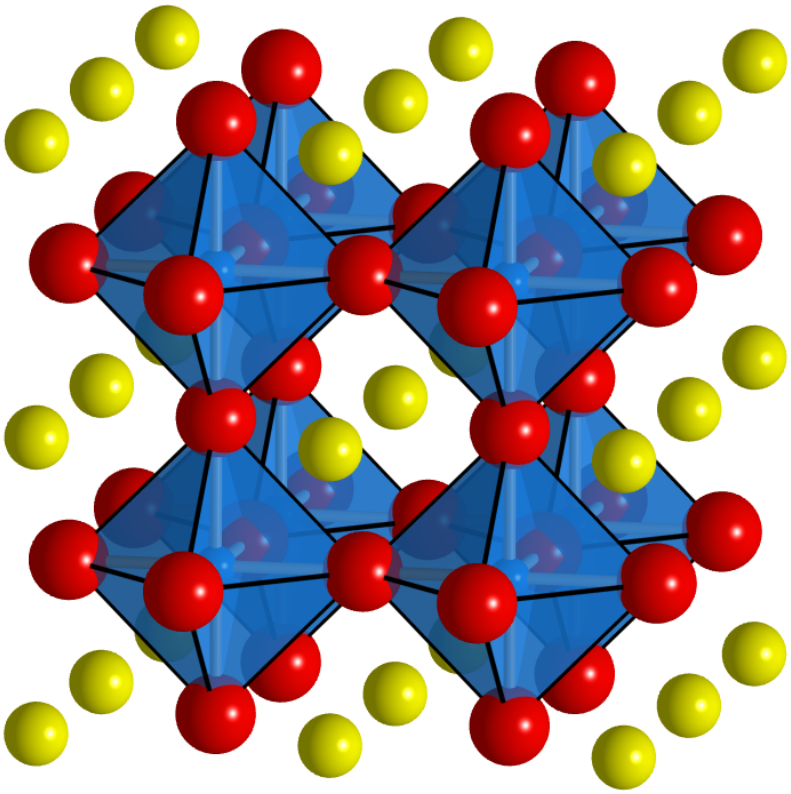

Figure 1.7: Perovskite structure ($CaTiO_3$) adopted by $BaZrO_3$ showing corner sharing ZrO_6 octahedra. Ba = yellow, Zr = blue. O = red.

multiferroics, ceramic membranes and both the electrolyte and cathode of SOFCs. The perovskite structure is ideally cubic, though many are distorted and exist in an orthorhombic space group, with the A site cation existing in a 12-coordinate position and the B-site in a six-coordinate environment.

Oxide-ion migration within perovskites is known to occur by vacancy hopping. Depending upon the perovskite and dopants a common motif of these migrations is a non-linear pathway first predicted for $LaGaO_3$ using the same techniques as used in this work [46]. This curved path was then confirmed experimentally using the maximum entropy method [47].

Acceptor doping of perovskites also allows new properties to be explored, such as hydration and proton conduction. A range of perovskites exhibit high proton conductivity, such as cerates and zirconates. Further to this, perovskites that

contain transition metal elements can also exhibit interesting electronic properties arising from redox reactions. This work will encompass all of these possibilities.

In chapter 4 we have investigated the defect and dopant properties of $BaMO_3$ (M = Pr, Th, Zr) proton conductors. The aim of this chapter is also to give insight into the atomic scale properties that give rise to proton conduction, such as the energy of hydration, proton local structure and proton-dopant interactions. Further to this, we also investigate oxide-ion migration within these phases.

In chapter 5, computer modelling techniques were applied to the perovskite-like $BiFeO_3$ phase, which has potential uses in magnetoelectrical devices and computer components due to its known multiferroic characteristics. However, a major drawback of $BiFeO_3$ is high leakage currents which are thought to be related to mobile oxygen vacancies. These vacancies have lead to the suggestion that this phase has potential as a mixed oxide-ion-electronic conductor in SOFC electrodes. Here we study the atomic scale phenomena that may give rise to these interesting properties. With a large amount of debate ongoing regarding the existence of Fe^{2+} within doped $BiFeO_3$ and the possibility of a related oxygen non-stoichiometry, special focus was paid to the multi-valent nature of iron and the effects this may have upon defect and dopant reactions. We also assess the suitability of $BiFeO_3$ as an oxide-ion conductor by probing the oxygen vacancy migration paths and the likelihood of vacancy-dopant binding interactions.

Chapter 2

Methodology

Computer modelling techniques are now well-established tools in the field of solid-state chemistry and have been applied successfully to studies on the atomic- and nano-scale. These studies have achieved a high degree of accuracy in calculating energetic and dynamic properties, such as the prediction of crystal structures and examination of defect chemistry. The increase in the use of computer simulation methods has been assisted by the ready availability of evermore powerful computers. A major theme of modelling work has been the strong interaction with experimental studies. The principal aims of computer modelling are to complement and assist in the interpretation of experimental studies (e.g., diffraction, conductivity), to investigate atomic-scale features that cannot be attained from experimental analysis alone (e.g., conduction paths, point defects, lithium insertion sites), and to have a predictive role in the improvement of materials. In this chapter a review of the computational modelling techniques used throughout this thesis are presented, although more substantial reviews are given elsewhere [48–50].

In general, three main classes of technique have been employed in the study of solid-state ionic materials: atomistic (static lattice), molecular dynamics (MD), and quantum mechanical (ab initio) methods. Atomistic techniques have been used to study many types of structure, with a range of possible uses, such as superconductors [51, 52], catalysts [53, 54] and ionic conductors [55–58]. For this study, where ion migration and large scale defects are required atomistic modelling is the most suitable technique. Atomistic techniques use pair potentials to simulate the interactions within a system, this chapter aims to explain the general theories on which the simulation packages are based. The specific program used in this study is GULP General Utility Lattice Program) code developed by Julian Gale [59].

2.1 Potential Model

The basis of the atomistic computer simulation techniques used in this work is the specification of a potential model. This is the description in mathematical terms, of the energy of the system as a function of particle coordinates. The Born model representation is the basis for our potential model:

$$U_L = \sum_{i,j} \frac{q_i q_j}{r_{ij}} + \sum_{i,j} \Phi(r_{ij}) + \sum_{i,j,k} \Phi(r_{i,j,k}) \tag{2.1}$$

where U_L is the lattice energy, and where the summations refers to ions i, j and k. The first term on the right side of the equation refers to the long-range Coulombic interactions, and the second term the short-range (usually repulsive) interactions. In some materials a third term is required, known as a three-body term which provides a degree of directionality and is a function of the coordinates of three atoms. A three-body term is usually used in less ionic systems, and has been used successfully in systems containing SiO_4^{4-} and PO_4^{3-} moieties, such as zeolites [60] and iron-phosphates [61].

2.1.1 Long-range Coulombic Interactions

The long range Coulombic term in the calculation requires that each discrete ion is assigned a charge. The majority of studies undertaken in this work employs integral charges and refer to the ions in their relevant oxidation state. This term is the sum of all of Coulomb interactions between pairs of ions i and j separated by r_{ij} where $\boldsymbol{l}$ is the set of lattice vectors representing the periodicity of the lattice.

$$\Psi = \sum_{\boldsymbol{l},i,j} = \frac{q_i q_j}{4\pi\epsilon_0(r_{ij} + \boldsymbol{l})} \tag{2.2}$$

The summation is related to $1/r$, meaning that it is conditionally convergent when

treated conventionally. Conditional convergence is defined as the series cannot find absolute convergence due to the positive series diverging to infinity and the negative series to negative infinity. To counteract this conditionally convergent series the Ewald summation [62, 63] is used.

The Ewald summation speeds up convergence of the Coulombic energy in a three dimensional periodic system by splitting the sum into two significant parts: a term in real space and a term in reciprocal space.

$$\varphi = \varphi_{\text{real}} + \varphi_{\text{reciprocal}} + \varphi_{\text{correction}} \tag{2.3}$$

The key to the Ewald summation is the use of Gaussian charge distributions. These allow faster convergence of the real space term. In real space, for every particle i, with charge q_i, a diffuse charge distribution is applied so that q_i is neutralised. This in effect "screens" the original point charges at large separation, meaning that the interaction rapidly tends towards zero, thus removing the slowly converging Coulombic $(1/r)$ term from the calculation. This allows the interactions to be addressed with the interaction in equation 2.2. The form of the Gaussian distribution representing the screening charge cloud is:

$$\rho_i = \frac{q_i \alpha^3}{\pi^{3/2}} \exp(-\alpha^2 r^2) \tag{2.4}$$

where α is related to the width of the distribution. This means the sum over point charges is now treated as a sum of the interactions between the charges and the corresponding neutralising distribution. Therefore the real space (φ_{real}) summation can be shown as:

$$V = \frac{1}{2} \sum_{i=1}^{N} \sum_{j=1}^{N} \sum_{|n|=0}{}' \frac{q_i q_j}{4\pi\varepsilon_0} \frac{\operatorname{erfc}(\alpha|\mathbf{r}_{ij} + \mathbf{n}|)}{|\mathbf{r}_{ij} + \mathbf{n}|} \tag{2.5}$$

where $\mathbf{n}$ is a cubic lattice point ($\mathbf{n} = n_x L, n_y L, n_z L$), with erfc being the comple-

mentary error function

$$\mathrm{erfc(x)} = \frac{2}{\sqrt{\pi}} \int_{\mathrm{x}}^{\infty} \exp(-t^2) dt \tag{2.6}$$

The real-space component is then added to the reciprocal-space component ($\varphi_{reciprocal}$) that comprises of a second charge distribution. This reciprocal charge distribution exactly counteracts the first neutralising charge distribution, and is defined as:

$$V = \frac{1}{2} \sum_{k \neq 0} \sum_{i=1}^{N} \sum_{j=1}^{N} \frac{1}{\pi L^3} \frac{q_i q_j}{4\pi\varepsilon_0} \frac{4\pi^2}{k^2} \exp\left(-\frac{k^2}{4\alpha^4}\right) \cos(\mathbf{k} \cdot \mathbf{r}_{ij}) \tag{2.7}$$

where **k** represents the reciprocal lattice vectors. This reciprocal sum now converges rapidly because it can be represented as a fourier series and can as such be represented by a smaller number of reciprocal vectors. When the real space and reciprocal space components are summed the result is the Coulombic point charge interaction energy, as summarised in Figure 2.1.

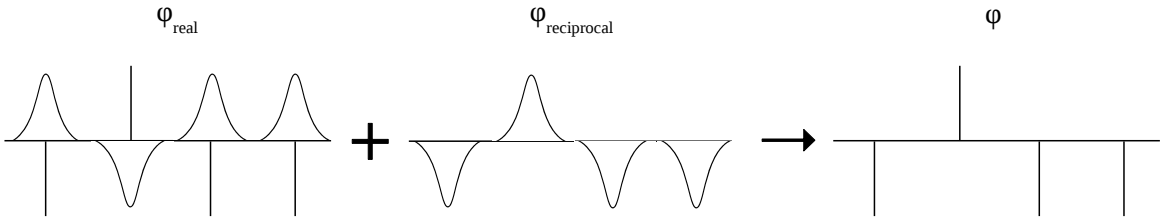

Figure 2.1: Schematic of the Ewald summation showing the sum of the real and reciprocal space components.

Furthermore a correction term must be added to the entire summation to take into account an interaction of the real space Gaussian cloud with itself. This is defined as:

$$V = -\frac{\alpha}{\sqrt{\pi}} \sum_{k=1}^{N} \frac{q_k^2}{4\pi\varepsilon_0} \tag{2.8}$$

It is interesting to note that the width of the Gaussian charge distribution has an impact upon the speed of convergence of both real and reciprocal components. The

wider the applied Gaussians the faster the real-space component converges, but the more terms that must be included in the reciprocal-space component meaning a slower convergence. This means the Gaussian width must be a compromise to allow the most efficient convergence of the entire summation. A more detailed derivation of the Ewald summation can be found in Leach [64].

2.1.2 Short-range Interactions

The short range interactions can be summed up using potential models that attempt to describe the forces at short distances. These potentials are described by parameterised functions. All short-range interaction potentials occur within real-space, and have a cut-off point meaning there is no problem with convergence that Coulombic terms have.

Buckingham Potential

The short-range potential used in this work is the Buckingham potential.

$$V_{ij}(r) = A\exp^{(-r/\rho)} - \frac{C}{r^6} \tag{2.9}$$

where A, ρ and C are the potential parameters, that have individual values for each type of i and j ion interaction. The first part of the Buckingham potential is the exponential term, which is the Pauli repulsion term that attempts to describe repulsion of two atomic charge clouds interacting at small r (Figure 2.2). This is supplemented by the second term (containing C) which is attractive and represents the van der Waals forces. These van der Waals interactions are normally small and highly dependant upon the polarisability of an ion. Therefore a C parameter is normally only included for very polarisable ions such as O^{2-} and are very rare for metal ions. The Buckingham potential has routinely been selected to model ionic

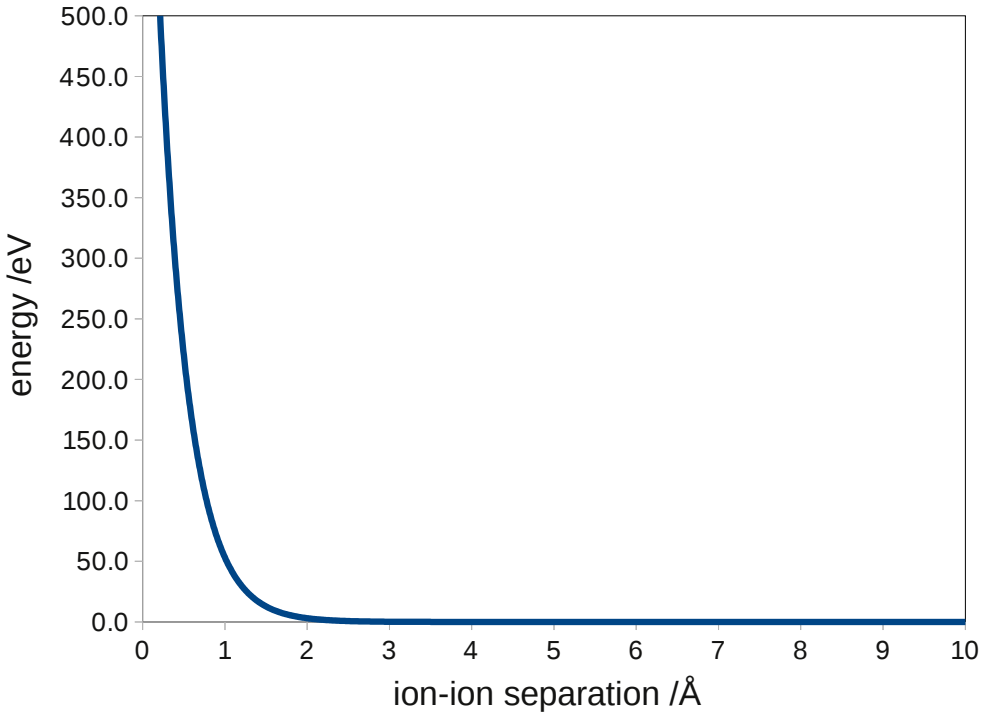

Figure 2.2: Plot of a Buckingham potential showing the repulsive effect at short ion-ion separations

solids.

Morse Potential

The Buckingham potential is ideally suited for describing ionic interactions, but less so when describing interactions that have a higher degree of covalent character. In our work the Morse potential is used for the interaction within the O-H group in water incorporation calculations. The Morse potential can be described as:

$$V_{ij}(r) = A_{ij}(1 - \exp^{[-B_{ij}(r_{ij}-C_{ij}]})^2 - A_{ij} \tag{2.10}$$

where A_{ij} is the binding dissociation energy, B_{ij} is related to the curvature of the potential energy well, and C_{ij} is the equilibrium bond distance. The Morse potential is ideal for use when the bond separations vary away from equilibrium.

Three-body potential

A three-body potential is used in conjunction with a two-body potential when it is necessary to take into account the angle dependant nature of a moiety such as SiO_4 and PO_4 tetrahedral units. The potential takes the form of a harmonic angle-bending term about the central ion and can be described with:

$$V_{ijk} = \frac{K_{ijk}}{2}(\theta - \theta_0)^2 \tag{2.11}$$

where K_{ijk} is a harmonic force constant and θ is the bond angle.

Shell Model

A problem with considering the system as a point charge model is the omission of the effects of polarisability. An accurate polarisability model is essential to the modelling of defects within crystals, as defects are known to polarise the lattice around them. The simplest model of polarisability is the point polarisable ion (PPI) model. A polarisability is assigned to each ion (α), with the dipole moment μ in a field of magnitude E given as:

$$\mu = \alpha E \tag{2.12}$$

There are issues with this model, it is known to perform poorly in calculating lattice dynamical properties of solids, which is largely due to this model not taking into account the relationship between short-range repulsion and polarisation.

The shell model, developed by Dick and Overhauser [65], is used in modern calculations, which consists of a large core, connected to a massless shell by a harmonic spring with force constant k (Figure 2.3). Both the shell and core have individual charges associated with them, with the total charge matching that of the discrete

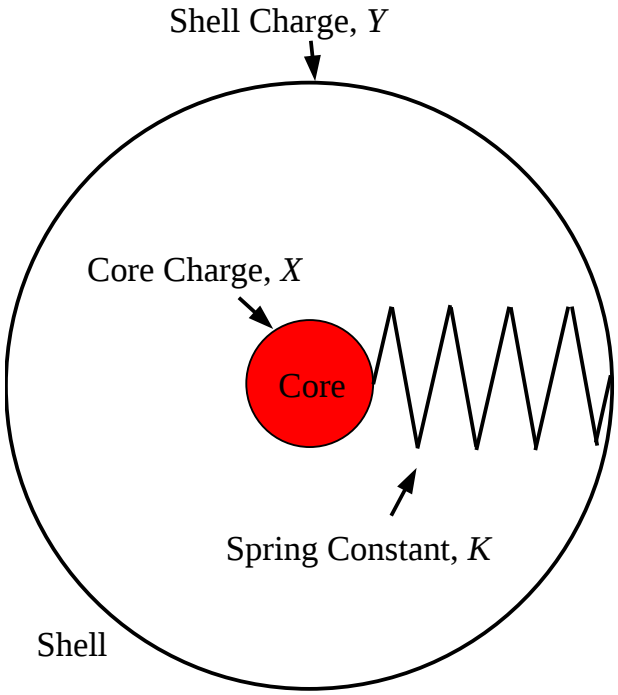

Figure 2.3: Dick and Overhauser shell model

ion. The repulsive term of the Buckingham potential only acts upon the shells of ions, meaning short range repulsion and polarisability are coupled.

When an electric field is applied to the ion the shell is displaced relative to the core, creating a dipole moment. The overall free-ion polarisability of the ion can be calculated with equation 2.13. This method also adds two new parameters that must be specified and evaluated for the calculations.

$$\alpha = \frac{Y^2}{k} \tag{2.13}$$

Where α is the polarisability of the ion, Y is the charge of the shell, and k is the harmonic force constant.

2.2 Derivation of Interatomic Potentials

Atomistic modelling techniques are inherently dependant upon the quality and reliability of the interatomic potentials available. The complexity of the structures investigated in current research also demands that the interatomic potentials are transferable. There are two procedures to derive new interatomic potentials; these are empirical and theoretical methods and are described below.

2.2.1 Empirical

Empirical potentials are usually derived by fitting the five potential parameters, A, ρ, C, Y (charge on the shell) and k (harmonic spring force constant) to try and reproduce the crystal structure and at least one other property of the system. This is usually achieved by adjusting the parameters using the least-squares procedure, which minimises the difference between the calculated and experimental properties.

$$F = \sum_{observable} \omega(f_{calc} - f_{obs})^2 \tag{2.14}$$

where F is the sum of squares f_{calc} and f_{obs} are calculated and observed quantities, respectively and ω is the weighting factor. The parameters can be fitted singularly or in groups and the more properties that the potential can accurately reproduce then the more likely it is that the potential is transferable to other systems. GULP empirically fits potentials by minimising the forces applied to each atom thought the alteration of the potential parameters. The user specifies which parameter is to be fitted and this is then altered to minimise these forces. A fitting study will consist of the sequential fitting of the parameters of the potential which is being derived until the accuracy of the reproduction of the structure can no longer be improved upon.

A problem can occur when using the shell model, in that the core positions we

wish to fit are accurate and known, whereas the shells cannot be assumed to be centred at the same coordinates than that of the core. GULP automatically fits by simultaneously relaxing core and shells as a work around for this problem. A drawback of empirical fitting is that derived potentials created using information about a specific crystal structure may not be valid for other structures. This means that the potential is only known to be accurate for its parent crystal structures interatomic spacings. The validity of the potential when applied to different crystal structures or defects where different interatomic spacings occur may be suspect. The validity of a potential can be proven by its transferability to other systems with accurate reproduction of experimental data. This validity issue may not arise for systems where there are a number of interatomic spacings, i.e. highly disordered or low symmetry systems. The potentials developed in this work have been done so by empirical methods.

2.2.2 Theoretical

Another approach to derive an interatomic potential is by fitting the parameters to data obtained from *ab initio* calculations, usually an energy surface. The most common of the theoretical approaches are based upon the electron-gas methods of Gordon and Kim [66] and Wedepohl [67]. The potential parameters are derived by calculating the interaction energy by solving the wave equations for each ion and then using the equation:

$$E_{ij}(r) = E_{ij}^{C}(r) + E_{ij}^{KE}(r) + E_{ij}^{COR}(r) + E_{ij}^{EX}(r) \tag{2.15}$$

where $E_{ij}^{C}(r)$ is the coulombic interaction term and $E_{ij}^{KE}(r)$, $E_{ij}^{COR}(r)$ and the $E_{ij}^{EX}(r)$ are the kinetic energy, correlation and exchange contributions to the interaction energy, respectively. To determine these terms the electron densities for each ion is needed. There are a series of approximations in this process, which are

detailed elsewhere [66]. Potentials developed in this way have shown to give good reproduction of interactions. However, a further modification to this method has been developed to increase accuracy, this is to perform the above method within a crystal environment. The effect of which modifies the electron densities and hence the resulting interatomic potentials.

2.3 Energy Minimisation

Once a good potential model has been obtained for the system to be investigated, it is then possible to acquire structural and defect properties. This can be accomplished by using energy minimisation techniques which calculate the equilibrium geometry of the system. The principles of energy minimisation are simple: the structural parameters of the solid are altered, including the ion coordinates, until the lowest energy configuration is discovered. This is performed for all ions simultaneously, until all ions are in their energy minima.

An issue with energy minimisation is that the energy profile of the crystal structure is very complex, being a multidirectional function of the ionic coordinates. The nature of energy minimisation algorithms can lead to local minima and global energy minima being indistinguishable (Figure 2.4). Typically, a global minima is what is needed. Once a local minima is found, energy is required to calculate bypass an energy barrier. Another drawback to energy minimisation techniques are that the vibrational properties are ignored, even the zero point energy, as the system is run at zero kelvin. Even with these drawbacks it has been shown that this method gives very good agreement with experimental results and observations.

There are a number of techniques to find the lowest energy minima and choosing the right one to balance accuracy and computational resources is key. The simplest minimisation technique is a simple search and scan until the minimum is discovered. This is overcomes the problem of local minima, but it is highly inefficient, using a

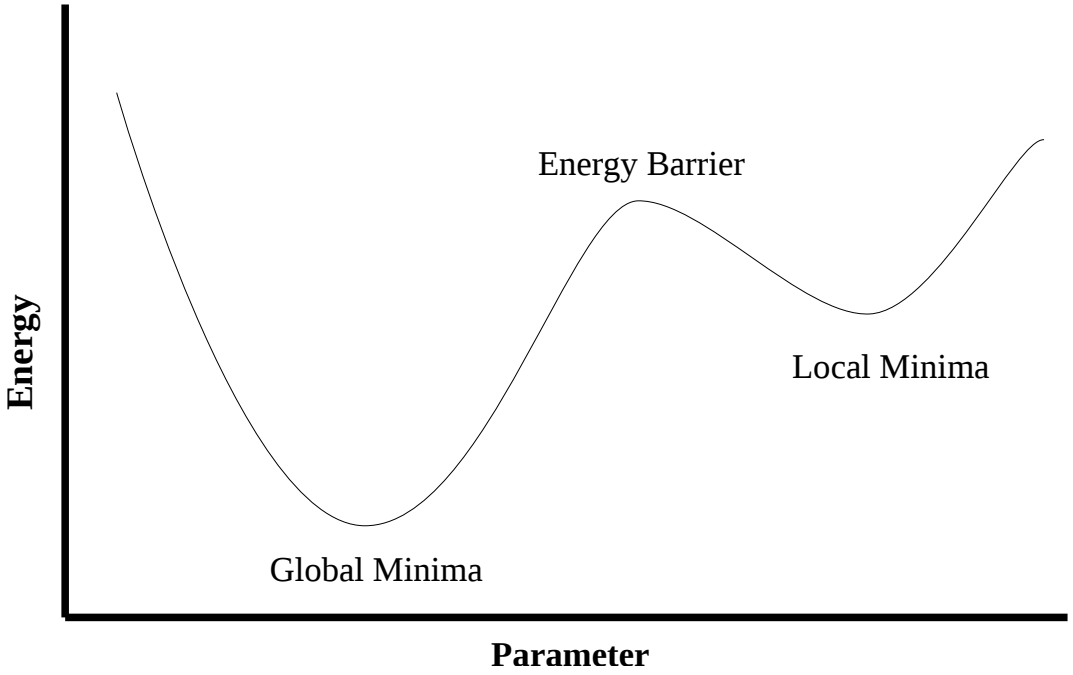

Figure 2.4: Local and global minima in a 1-dimensional energy surface.

lot of processor time; with no real direction in searching. This technique is never used.

The algorithms used to find energy minima can be separated into two main types, ones that use derivatives of the energy with respect to position, known as gradient techniques, and others that do not. The advantage of using gradient techniques is that they can provide a more efficient minimisation by using information derived from the shape of the energy surface. The most basic of gradient techniques can be represented as:

$$x_{(p+1)} = x_p - g_p\delta \tag{2.16}$$

Where $x_{(p+1)}$ is a vector for the p+1 iteration; x and g are variables along with their gradients for the p–th iteration. The choice of δ is important as it determines the speed of convergence (how many iterations occur to find the minima). This is known as the steepest descent method and can be seen in Figure 2.5.

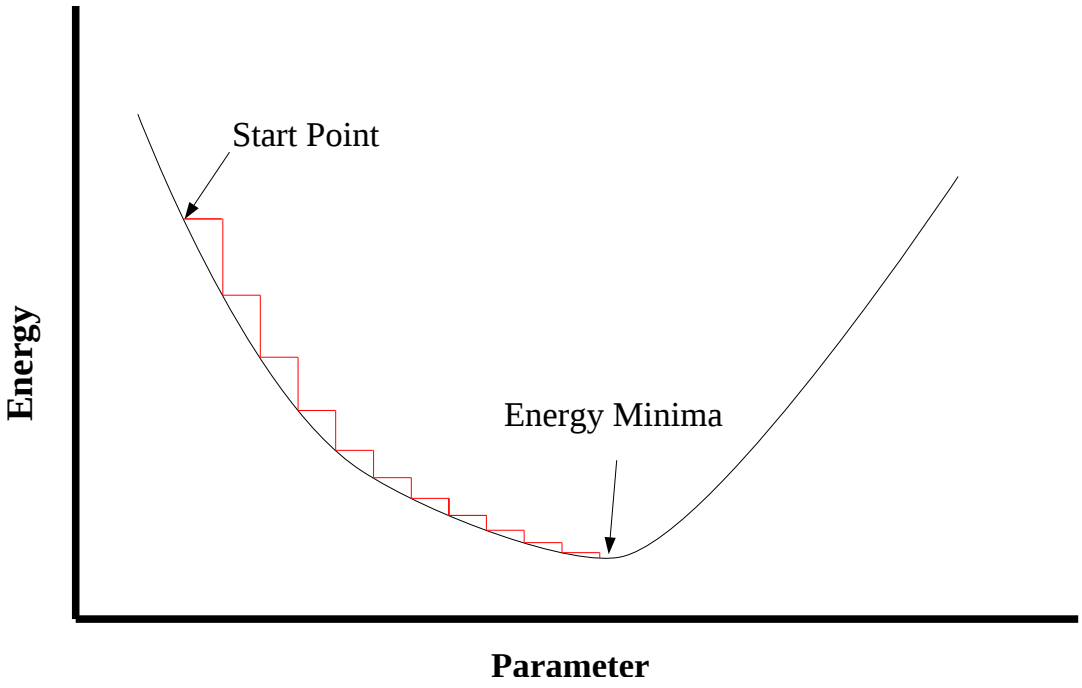

Figure 2.5: 1-D schematic of the steepest descent method

To speed up the convergence the second derivatives may be used in what is known as the Newton-Raphson method. This method is very efficient and is used by default by the GULP program used in this work and is represented as:

$$x_{(p+1)} = x_p - (W_p)^{-1} g_p \tag{2.17}$$

The W is a matrix of second derivatives and is known as the Hessian matrix and is required to be inverted. In the earlier days of computer simulation methods the inversion and calculation required a significant amount computational power, but in modern high powered computers this is less of an issue. Still, the Hessian is not usually calculated at every opportunity as this would extend the calculation time dramatically. Therefore updating schemes are used to make approximations to update the Hessian every iteration. Within a minimisation it is common for the Hessian to be fully recalculated and inverted whenever one of a number of criteria is reached. These are (i) a maximum number of cycles is exceeded, (ii) the energy

has dropped past a defined limit in a single cycle, (iii) the energy cannot be lowered along the current search vector, and (iv) the angle between the gradient vector and search vector is greater than a specified threshold.

There are a number of methods for updating the Hessian matrix, the most efficient and the default within the GULP code is the Broyden-Fletcher-Goldfarb-Shanno (BFGS) scheme. GULP uses symmetry-adapted energy minimisation techniques. This means GULP uses symmetry information to calculate the minimum number of variables needed to reach an energy minima, and to increase the speed of calculation of the first derivatives and Hessian matrix.

2.4 Modelling of defects

The creation of a defect species in a crystal causes the surrounding lattice to relax (Figure 2.6). The effects are usually long-range Coulombic and therefore a large amount of ions are required to model this accurately. If all of the atoms were to be fully modelled then the simulation would be prohibitively long and complex.

To accurately simulate the defect without compromising computational resources the Mott and Littleton two region method is applied. The defect energy is defined as the difference between the lowest energy configurations of the defect system and the perfect crystal lattice. Region I is the region that directly surrounds the defect, and usually comprises 700-1000 ions. In this region all forces are explicitly calculated and relaxed according to the Newton-Raphson method. As region II is further away from the defect, and the pertubation effects are lessened, the calculations do not have to be as explicit and these regions are considered as pseudo-continuum. Region II reacts to the effective charge of the defect as a dielectric response. Taken from dielectric continuum theory, the polarisation (P) of a crystal per unit cell, at

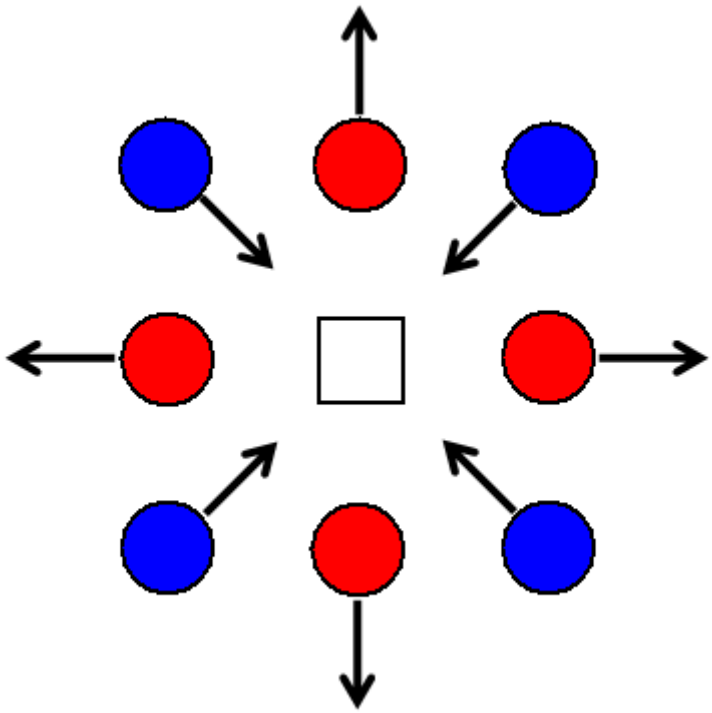

Figure 2.6: Schematic diagram of a relaxation of lattice containing a point defect

a point (d) relative to the defect of charge (q) at the origin can be seen as:

$$P = \frac{V}{4\pi}\left(1 - \frac{1}{\varepsilon_0}\right)\frac{qd}{r} \tag{2.18}$$

where V is the unit cell volume, q is the effective charge of the defect, and ε_0 is the static dielectric constant. The total defect energy (E_D) can be summarised with the equation:

$$E_D = E_I(x) + E_{IIA}(x, y) + E_{IIB}(y) \tag{2.19}$$

where E_I is the function of ion co-ordinates and dipole moments; E_{IIA} is the interaction between region I and II, allowing a smoother convergence during minimisation; E_{IIB} is dependant on displacements (y) in region IIA.

Within the GULP code the radii of region I and region IIA are specified. It is ideal to have the size of region IIA to be at least the same as the defined potential cutoff, which is typically 10-12Å. When applying these methods to a crystal structure a

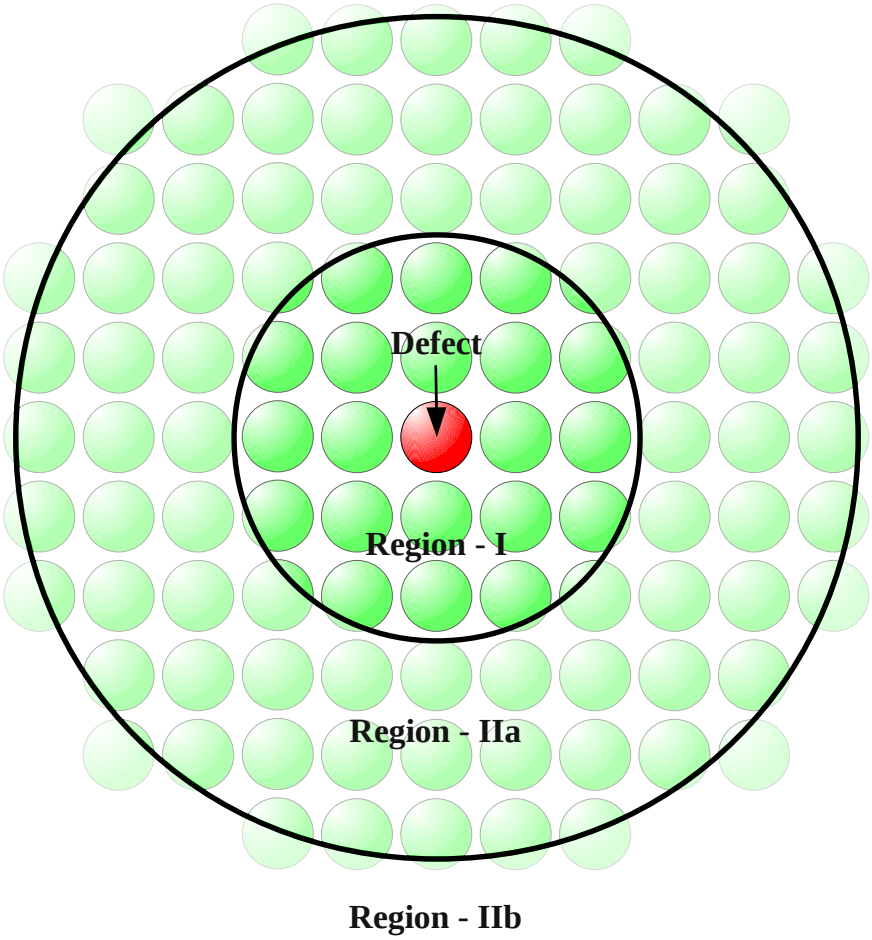

Figure 2.7: Schematic of the Mott-Littleton two region method.

series of test calculations are often undertaken to determine the optimal size for regions I and IIa.

When investigating a dynamic process using static lattice methods, it is common to create a calculation that contains multiple defects that provide a "snapshot" of the process. A series of these snapshots would allow and energy profile of the process to be created and therefore the energy of the process can be calculated. An example of a vacancy hop in the rock salt structure is shown in Figure 2.8.

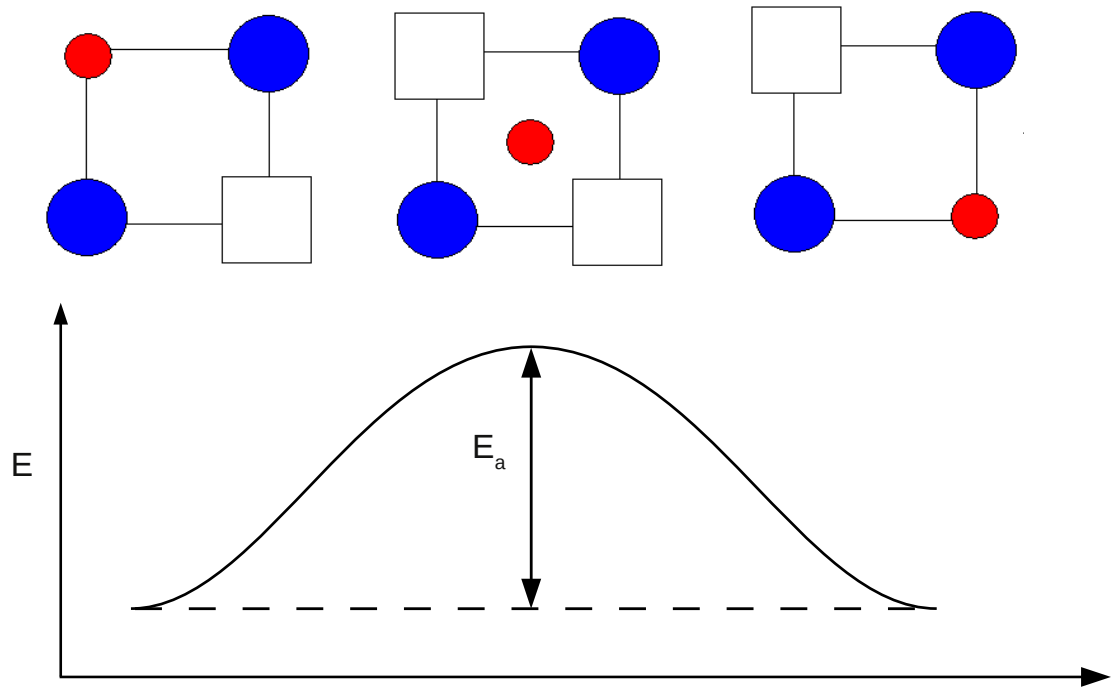

Figure 2.8: Schematic of vacancy hopping mechanism using the rock salt structure and the energy profile of the process where E_a is the migration activation energy.

2.5 Calculations

2.5.1 Equipment and Calculation Speed

A number of computer systems were used throughout this work. Primarily, desktop systems were utilised as GULP is optimised for single core processing.

Example specification of desktop system:

Intel Pentium D (Dual Core) 3.4GHz

4GB RAM

160GB HDD

nVidia GeForce 7300 LE graphics card

Further to the desktop machines, a number of servers that utilise a CONDOR high throughput computing (HTC) system were employed, that allowed a high volume of calculations to be submitted and automatically managed. This method assigns a single core per calculation, but could utilise the larger reserves of RAM on the servers.

Example specification of server:

2 x Quad-Core AMD Opteron 2360 SE 2.5 GHz
16GB RAM
160GB HDD
nVidia GeForce 8400 GS graphics card

The time taken to complete a structural optimisation calculation is dependant upon the size, complexity and degree of symmetry of the material. A typical high symmetry system (such as ZrO_2) will take between a few seconds and 5 minutes (when run on systems with the example specifications). A complex P1 cell (such as the Bi-Re system in this work) will take between 5 minutes to an hour. Faster processors typically perform structural optimisations quicker, however, in this work little difference was observed between systems.

A defect energy minimisation is dependant upon the complexity of the material and the size of the regions employed in the Mott-Littleton method. A series of calculations should be performed on each material to determine the best sizes for these regions that balance accuracy with calculation duration. Defect calculations typically take 5 to 20 minutes for simple materials and upwards of 1 hour for complex structures. It is not uncommon for highly complex structures to run overnight. Throughout this work it was observed that defect calculations would converge more quickly when on servers with access to greater reserves of RAM.

It must be noted that if a potential model is unreliable (or incorrect) calculation

time can be increased.

2.5.2 Calculation Error

The models developed in this work aim to be self consistant and by fitting to, and comparing with experimental data at multiple points within the development process, as accurate as possible. The calculations will not always reproduce the absolute accuracy of experimental data. However, the methods employed within the development process does allow trends in results to be asessed. The precision of the results are assessed by a series of test calculations (as mentioned in 2.5.1) in which parameters, such as the Mott-Littleton region sizes, are incrementally altered until the result is consistant to 4 decimal places.

Chapter 3

Structural and Defect Properties of Doped Bismuth Oxides

3.1 Introduction

Many of the best oxide-ion conducting solid electrolytes exhibit the fluorite structure and have potential applications in fuel cells, sensors and oxygen pumps. Well known examples include yttrium stabilized zirconia, YSZ, ($Zr_{1-x}Y_xO_{2-x/2}$) and gadolinium doped ceria, CGO, ($Ce_{1-x}Gd_xO_{2-x/2}$)[3–8, 68, 69]. The highest known oxide ion conductivity of any solid occurs in the defect fluorite δ-Bi_2O_3, with conductivities in the order of 1 S cm^{-1} at *ca.* 730°C [70]. However, the stability window of this phase is rather limited and much research has been carried out in stabilizing the high temperature phase at substantially lower temperatures, mainly through solid-solution formation with other oxides [71–75] (as discussed in section 3.2).

Bi_2O_3 exists in four forms (α, β, δ, γ). The $\alpha-Bi_2O_3$ monoclinic form occurs at room temperature and has poor oxide ion conductivity, but when heated past 1003K transforms into the highly oxide ion conductive fluorite-structured $\delta-Bi_2O_3$ that is stable to 1097K[76, 77]. When $\delta-Bi_2O_3$ is cooled it transforms into one of two forms of Bi_2O_3; tetragonal β-Bi_2O_3 is formed at 923K and returns to $\alpha-Bi_2O_3$ at 576K, or body centred cubic $\gamma-Bi_2O_3$ is formed at 912K and if cooled slowly the γ form can remain stable at room temperature, but if not cooled slowly the $\alpha-Bi_2O_3$ form is regenerated at 773K (summarised in Figures 3.1 and 3.2). This polymorphism of Bi_2O_3 has been extensively reviewed elsewhere [74]. Observations have shown that a δ to β transition is accompanied by a large volume change and deterioration of the mechanical properties of the material. This would be undesirable within a fuel cell as considerable mechanical stress would be placed on the physical structure of the cell, which makes the stabilisation of the δ form of Bi_2O_3 at lower temperatures a priority for both ionic conductivity and fuel cell durability reasons.

$\delta-Bi_2O_3$ has a fluorite-type structure, similar to current generation SOFC electrolytes ZrO_2 and doped CeO_2, but $\delta-Bi_2O_3$ differs by being intrinsically anion

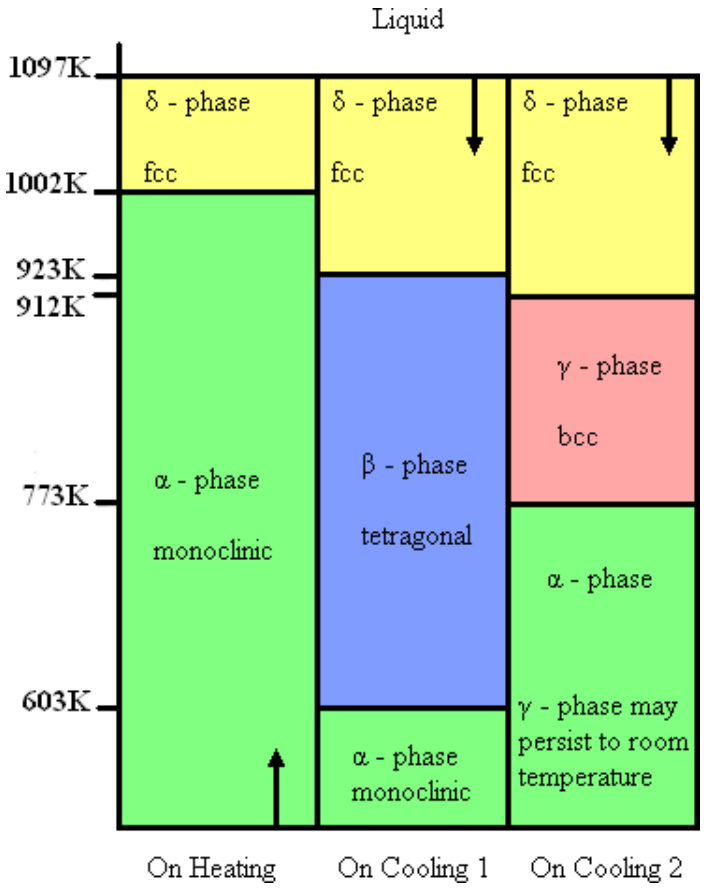

Figure 3.1: Temperature dependance of the four forms of Bi_2O_3[74]

deficient. The majority of all oxide ion conduction that occurs within a fluorite structure is vacancy based ion migration. As the $\delta-Bi_2O_3$ structure is anion deficient when compared to a regular fluorite system there are two intrinsic oxygen vacancies per unit cell that are thought to be statistically disordered (Figure 3.3).

The ordering of the intrinsic anion vacancies has been the source of debate for many years, and will also be examined in this work. There have been three main models proposed for $\delta-Bi_2O_3$:

(i) Sillen Model - 1937 [78]

A simple cubic flourite structure with the 25% oxygen vacancies ordered along the $\langle 111 \rangle$ as shown in Figure 3.4.

(ii) Gattow Model - 1962 [76]

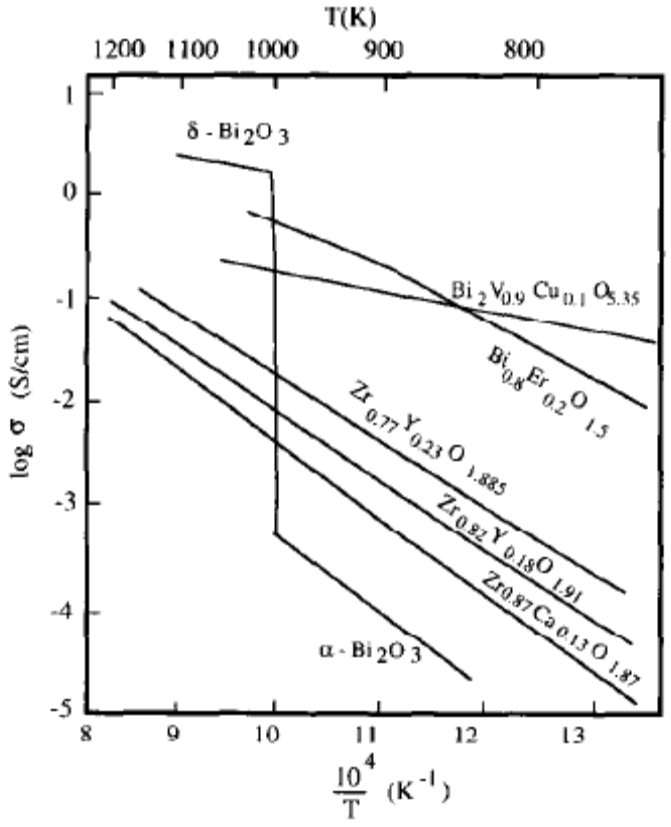

Figure 3.2: Arrhenius plot to show the temperature dependence of ionic conductivity highlighting $\alpha-Bi_2O_3$ and $\delta-Bi_2O_3$ from Shuk et al. [73]

The Sillen model was modified by Gattow and Schroder by describing the intrinsic vacancy ordering as spread over all possible 8c anion sites, as shown in Figure 3.5. This model assigns each 8c site with 75% oxygen occupancy causing the assumption that there is no ordering within the oxygen sub-lattice.

(iii) Willis Model - 1965 [79]

Originally proposed by Willis to give a better discription of the CaF_2 phase it has also been proposed for the $\delta-Bi_2O_3$. The anions not only inhabit the classic 8c positions but also occupy a 32f position, which is shifted along a $\langle 111 \rangle$ direction towards the centre of the unit cell as shown in Figure 3.6. This model has been used to successfully describe the structure of $\delta-Bi_2O_3$ by various groups that include, Catlow [80], Sammes [74] and more recently Yashima [81].

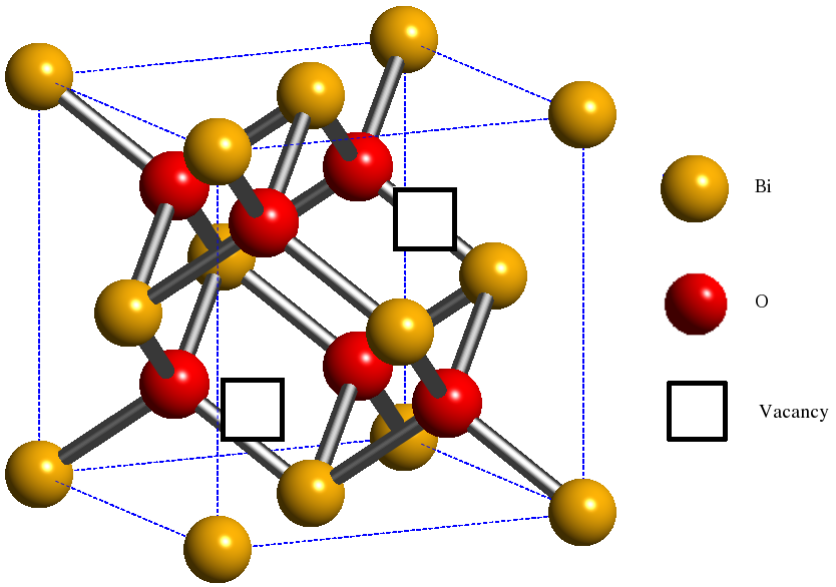

Figure 3.3: Structure of Bi_2O_3 (with oxygen vacancies in $\langle 110 \rangle$ configuration)

The one constant with all models is the complex, potentially disordered and mobile nature of the oxide-ion sub-lattice within $\delta{-}Bi_2O_3$. This is thought to be the reason for its fast oxide-ion conductivity properties. Other factors that are thought to enhance oxide ion transport within $\delta{-}Bi_2O_3$ are the Bi^{3+} lone pairs, which lead to a high polarisability of the cation network, and the ability for Bi^{3+} to accommodate disordered oxygen surroundings.

3.2 Doped $\delta{-}Bi_2O_3$

Aliovalent and isovalent doping are not only used to increase the ionic conductivity of a system, but in the case of Bi_2O_3 it is used to stabilise the high temperature δ-Bi_2O_3 phase, as shown by Takahashi et al[70, 82]. These phases are ion conducting solid solutions made up of Bi_2O_3 and the doping metal oxide, and are usually known as a binary systems, of which there are many examples [83]. These doped Bi_2O_3 systems are thought to be stabilised by the contraction of the δ-Bi_2O_3 structure due to the effect of the doping ion as stated by Verkerk et al[84]. It was also reported by Verkerk, that doping with an ion with similar ionic radius to that of

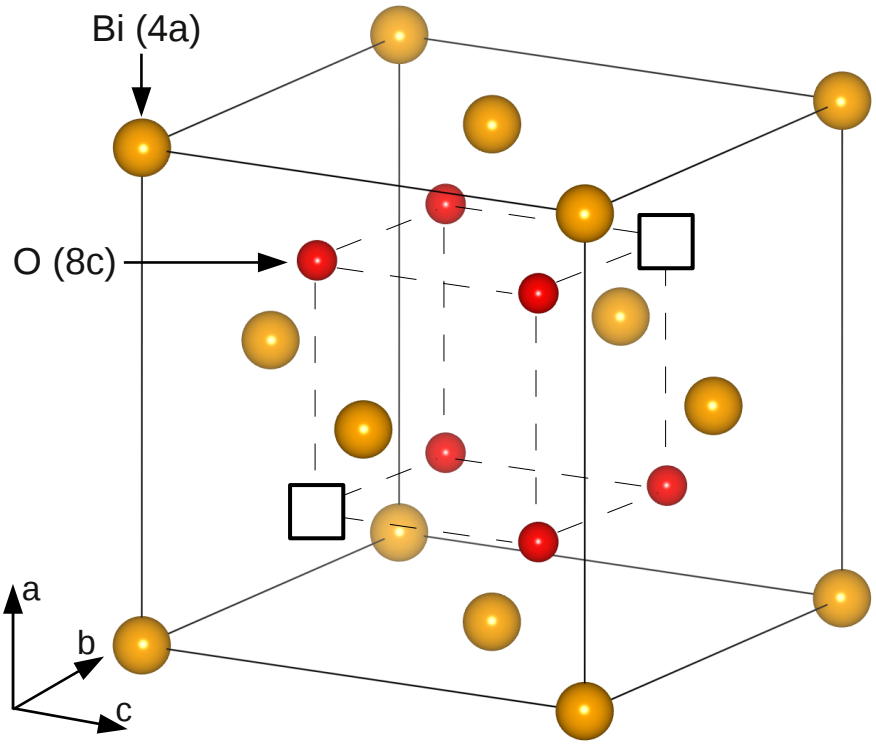

Figure 3.4: Sillen model of $\delta-Bi_2O_3$ with 25% oxygen vacancies

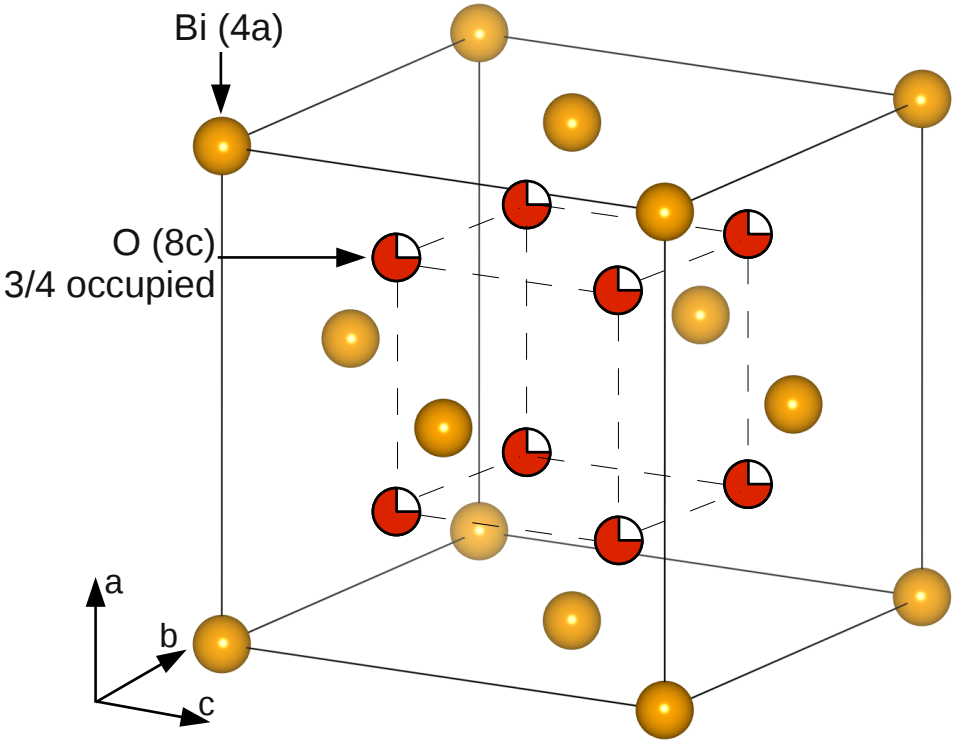

Figure 3.5: Gattow model of $\delta-Bi_2O_3$ with 3/4 occupancy of 8c site

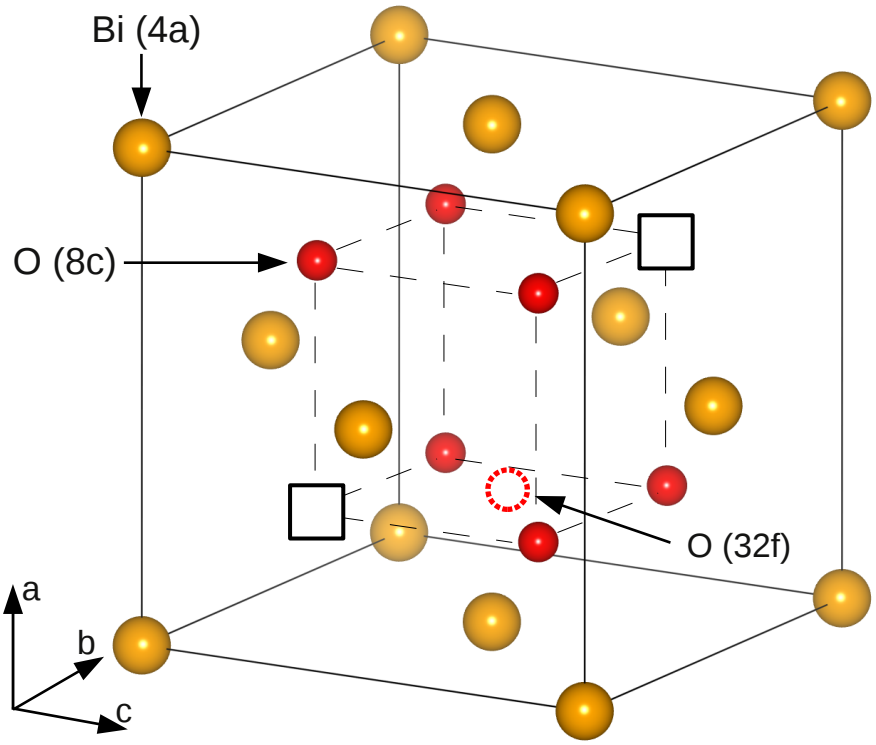

Figure 3.6: Willis model of $\delta-Bi_2O_3$ showing a 32f position

bismuth requires a higher percentage of dopant to stabilise the δ-Bi_2O_3 phase than when the doping ion is larger in size. However, the larger a dopant is, the greater amount the structure is distorted. If the dopant ionic radius is too large then the cubic structure of δ-Bi_2O_3 becomes unstable. More recently, co-substitution, the doping of the cation network with two different dopants, has been studied [85–87]. However, these phases have so far been found to be as unsuitable as practical solid electrolytes, as the majority are only metastable and usually convert to a rhombohedral form[88].

3.3 Structural and Defect Properties of Y - Doped Bismuth Oxide

3.3.1 Experimental Background

Y_2O_3 has been used extensively as a dopant for Bi_2O_3 with a range of solid phases created [70, 75, 82]. The Bi_2O_3-Y_2O_3 binary system has been investigated by several authors and their work is extensively reviewed by Sammes et al.[74] Our work will focus on the Bi_3YO_6 phase which is a stabilised form of $\delta-Bi_2O_3$. Datta and Meehan used XRD to characterise the Bi_3YO_6 structure and reported a pure δ-phase stable at temperatures below 400℃ [89]. The oxide-ion conduction for this phase has been reported to be fast with an Arrhenius activation energy (E_a) of 0.66 eV at high temperature [71]. Further research by Watanabe on compositions similar to Bi_3YO_6 in the $Bi_2O_3-Y_2O_3$ system show that after prolonged annealing at 650℃, a transformation from cubic to a stable hexagonal phase occurs. On further heating to 720℃ the cubic phase is reformed. This leads to the conclusion that the δ phase observed at room temperature was merely a quenched metastable phase and that the kinetics of the cubic to hexagonal phase transition are very "sluggish".

δ-Bi_3YO_6 is structurally very similar to δ-Bi_2O_3 [90]. Y^{3+} being isovalent with Bi^{3+} results in the same nominal vacancy concentration in Bi_3YO_6 as in the pure bismuth oxide ($\frac{1}{4}$ of the available oxide ion sites in the fluorite structure are vacant in both systems). However, there are likely to be significant differences associated with the preferred coordination environments of Bi^{3+} and Y^{3+}. Detailed characterization of the defect structure in these systems is key to understanding the ionic conduction mechanism. Nevertheless, since these phases are disordered on the crystallographic scale, conventional diffraction methods yield only an average picture. Recent work by Abrahams et al. [91, 92] has attempted to establish the structure and short range ordering of oxygen vacancies within Bi_3YO_6 using total scattering analysis,

involving both Bragg and diffuse scattering.

A number of studies have been carried out on modelling the undoped δ-Bi_2O_3 structure, in particular to assess the vacancy ordering. Jacobs and MacDonaill [93–95] investigated various models and found that $\langle 111 \rangle$ aligned vacancies were more stable than those aligned along $\langle 100 \rangle$, but that $\langle 110 \rangle$ vacancies are also present. Total energy calculations by Medvedeva et al. [96] also found $\langle 111 \rangle$ vacancy ordering to be the most stable. These findings are in contrast to those of Walsh et al. [97] who used density functional theory (DFT) calculations to predict that $\langle 100 \rangle$ ordering is favored. In a recent detailed investigation by Aidhy et al. [98], using molecular dynamics (MD) and ab initio methods, it was concluded that a combination of $\langle 110 \rangle$ and $\langle 111 \rangle$ vacancy alignment occurs. Even more recent publications utilizing a combination of DFT and neutron total scattering data by Mohn et al. [99] and Hull et al. [100] show that δ-Bi_2O_3 does not adopt a fluorite structure at the local scale, but instead favors an asymmetric Bi^{3+} co-ordination which is closely related to that found in the metatable δ-Bi_2O_3 phase.

This chapter presents a computational study of the oxide-ion conductor, Bi_3YO_6. Our study focusses upon the oxygen vacancy ordering, the intrinsic defect chemistry and the trends in dopant incorporation within the Bi_3YO_6 phase.

3.3.2 Crystal Structure and Potentials

Bi_3YO_6 adopts a cubic fluorite-type structure with a lattice parameter a = 5.4918Å in space group $Fm\bar{3}m$[91]. The cations are located at conventional fluorite cation positions (4a) position with a 3:1 Bi^{3+}/Y^{3+} ratio, whereas, the oxygen ions are located in two positions. Neutron powder diffraction (NPD) data (Table 3.1) shows a small displacement occurs from the standard 8c fluorite anion site, along $\langle 111 \rangle$ towards (0.3, 0.3, 0.3) to a 32f site. A 48i position which is also partially occupied at higher temperatures has been characterised, [92] as shown in Figure 3.7.

Table 3.1: Refined atomic parameters for Bi_3YO_6

(a) 25℃ from Abrahams et al. [91]

Atom	x	y	z	Cell Occupancy
Bi	0.00	0.00	0.00	0.75
Y	0.00	0.00	0.00	0.25
O1	0.25	0.25	0.25	0.525(5)
O2	0.329(1)	0.329(1)	0.329(1)	0.055
$Fm\bar{3}m$; a = 5.4918(1)Å				

(b) 800℃ from Abrahams et al. [92]

Atom	x	y	z	Cell Occupancy
Bi	0.00	0.00	0.00	0.75
Y	0.00	0.00	0.00	0.25
O1	0.25	0.25	0.25	0.388
O2	0.3089	0.3089	0.3089	0.073
O3	0.50	0.0.1656	0.1656	0.017
$Fm\bar{3}m$; a = 5.55982(7)Å				

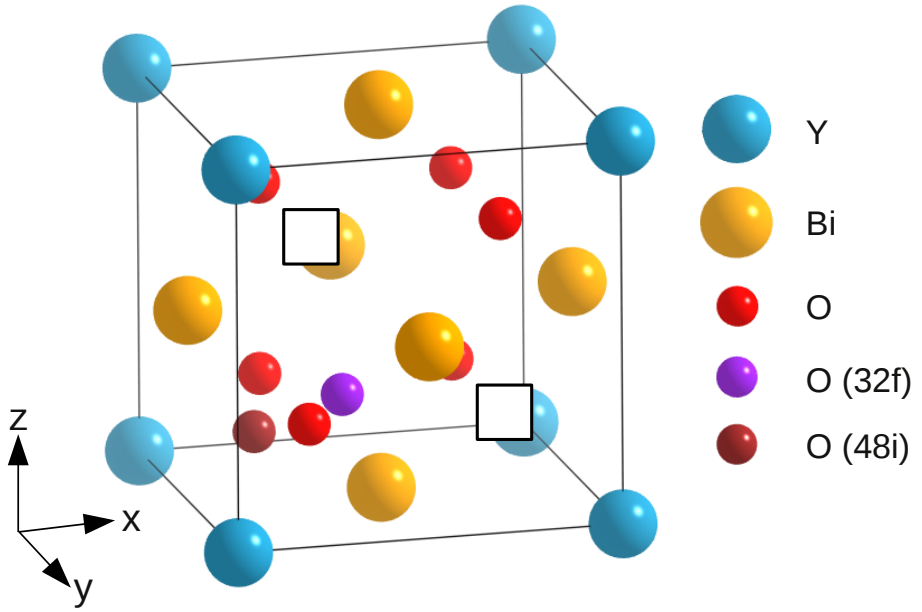

Figure 3.7: Crystal structure of Bi_3YO_6 with examples of the 32f and 48i positions.

Table 3.2: Interatomic potentials for Bi_3YO_6

(i) short-range

Interaction	A (eV)	ρ (Å)	C (eV Å^6)	Ref
$Bi^{3+} \cdots O^{2-}$	49529.35	0.2223	0.000	[101]
$Bi^{3+} \cdots Bi^{3+}$	24244.5	0.3284	0.000	[101]
$Y^{3+} \cdots O^{2-}$	1519.279	0.3291	0.000	[102]
$O^{2-} \cdots O^{2-}$	9547.96	0.2192	32.000	[103]

(ii) shell model

Species	$Y(e)$	k (eV Å^{-2})	ref
Bi^{3+}	-5.51	359.55	[101]
O^{2-}	-2.04	6.3	[103]

Short-range parameters for Bi-O and Bi-Bi interactions and shell model parameters for each ion were taken directly from a previous study on Bi_2WO_6 [101], while the parameters of Y-O were taken from a study of binary and ternary oxides [102]. The parameters for the O-O interaction were obtained from work by Grimes et al [103]. The full set of interatomic potentials and shell model parameters used in the present study are listed in Table 3.2. For the present calculations a supercell 27 times the size of the fluorite unit cell was constructed in space group P1 so that all atom sites within the cell could serve as locations for point defects. In creating this system the anions were positioned only at the ideal fluorite anion site (8c in space group $Fm\bar{3}m$), to keep the occupancy of anion sites as simple as possible. Repetition of the unit cell in three dimensions ensured that the yttrium atoms were evenly distributed throughout the crystal lattice with maximum separation.

There are three possible short range configurations of vacancy ordering: $\langle 100 \rangle$ ordering the vacancies along an axis, $\langle 110 \rangle$ ordering diagonally across a face of the unit cell, and $\langle 111 \rangle$ ordering along the body diagonal of the unit cell as shown in Figure 3.8. Further to this, the ordering scheme used by Aidhy et al. [98], that

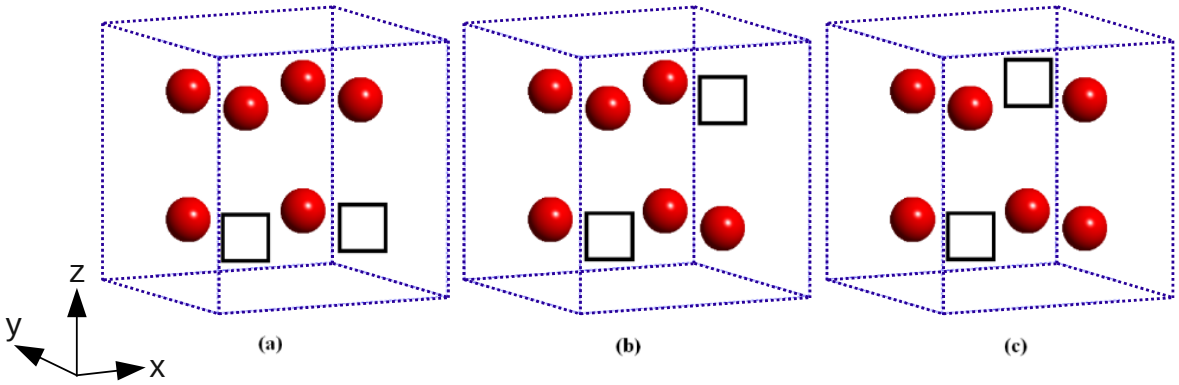

Figure 3.8: Possible ordering of cations in a single unit cell Sillen model of Bi_3YO_6 (a) ⟨100⟩ (b) ⟨110⟩ (c) ⟨111⟩.

combines ⟨110⟩⟨111⟩ orderings has been used. Finally, a number of cells with the oxygen vacancy distribution being random were also investigated.

Comparison of the lattice energies of the ordering models listed in Table 3.3 reveals that ⟨111⟩ ordering is the least stable, with the ⟨110⟩ configuration slightly lower in energy than ⟨100⟩ and the disordered state. This is consistent with the structural analysis, indicating evidence for ⟨110⟩ vacancy ordering in δ-Bi_3YO_6. It is worth noting that previous ab initio studies of similar intrinsic oxygen vacancy ordering in pure δ-Bi_2O_3 found that ⟨111⟩ ordering was least favorable and ⟨100⟩ was only 0.06eV more stable than that of ⟨110⟩ [97]. However, our results suggest that the lowest energy vacancy configuration identified for Bi_3YO_6 is a 2 x 2 x 2 supercell containing a combination of ⟨111⟩ and ⟨110⟩ vacancy configurations, previously found to be the lowest energy configuration for pure δ-Bi_2O_3 by ab-initio calculations [98].

The calculated unit cell parameters for Bi_3YO_6 for the different ordering models shown in Figure 3.8 are also listed in Table 3.3 and compared to the experimentally observed values. Interestingly, small differences in unit cell volume are observed for the different vacancy ordering configurations, with the ⟨110⟩ configuration yielding the largest unit cell volume of the ordered states, but still significantly lower than that for the disordered state.

Table 3.3: Experimental and calculated lattice parameters for Bi_3YO_6

Parameter	Expt.	single cell			supercell	
		Calc. ⟨100⟩	Calc. ⟨110⟩	Calc. ⟨111⟩	Calc. ⟨110⟩⟨111⟩	Calc. random
a/Å	5.495	5.375	5.331	5.430	5.476	5.479
b/Å	5.495	5.508	5.643	5.430	5.476	5.483
c/Å	5.495	5.375	5.331	5.430	5.476	5.505
β/Å	90.0	86.9	88.8	88.2	90.0	89.8
lattice energy /eV	-	-275.51	-275.71	-270.45	-279.33	-275.49

A significant feature of these supercell calculations is the relaxation of the oxygen atoms from starting points equivalent to the 8c lattice position in the $Fm\bar{3}m$ subcell, to positions equivalent to the 32f site in the cubic subcell as shown in Figure 3.9. The average deviation from the 8c lattice site was 0.47Å. The modelling work therefore reproduces a structural feature observed in the experimental studies, which was not incorporated into the input simulation structure and provides a valid starting point for the defect calculations.

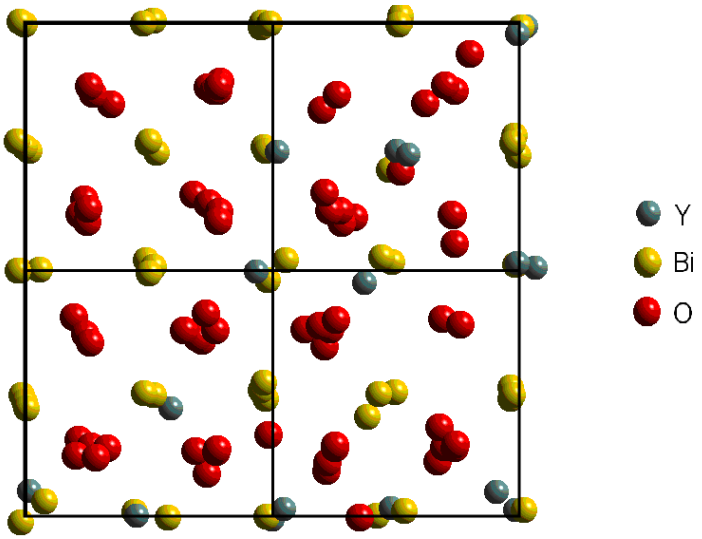

Figure 3.9: Relaxed structure of a Bi_3YO_6 supercell

3.3.3 Intrinsic Defect Formation

The energies of isolated point defects in the ⟨110⟩ single cell of Bi_3YO_6 were calculated. Vacancies on the various oxygen sites were examined, as well as a number of possible interstitial sites. The most favourable interstitial site for oxide ions was found to be on the intrinsic vacancy sites (*ca.* $\frac{1}{4}$, $\frac{1}{4}$, $\frac{1}{4}$), making the structure similar to that of Bi_3NbO_7, and it has thus been termed a pseudo-interstitial site by Jacobs and MacDonaill[93]. The 48i site was also considered and the mean value was found to be less favourable by at least 1eV. The total energies for Frenkel and Schottky-type energies for the various species were then derived by combining the individual defect energies and the appropriate lattice energies according to the following reaction equations: note that Kröger-Vink notation is used where, for example, $O_O^{\times}$, $V_O^{\bullet\bullet}$ and O_i'', indicates a lattice anion, an oxygen vacancy (+2 effective charge) and an oxygen interstitial (-2 effective charge) respectively.

O Frenkel disorder

$$O_O^{\times} \rightarrow V_O^{\bullet\bullet} + O_i'' \tag{3.1}$$

Bi Frenkel disorder

$$Bi_{Bi}^{\times} \rightarrow V_{Bi}''' + Bi_i^{\bullet\bullet\bullet} \tag{3.2}$$

Bi_3YO_6 Schottky disorder

$$3\,Bi_{Bi}^{\times} + Y_Y{}^{\times} + 6\,O_O^{\times} \rightarrow 3\,V_{Bi}''' + V_Y''' + 6\,V_O^{\bullet\bullet} + Bi_3YO_6 \tag{3.3}$$

Bi_2O_3 partial Schottky disorder

$$2\,Bi_{Bi}^{\times} + 3\,O_O^{\times} \rightarrow 2\,V_{Bi}''' + 3\,V_O^{\bullet\bullet} + Bi_2O_3 \tag{3.4}$$

Y_2O_3 partial Schottky disorder

$$2\,Y_Y{}^{\times} + 3\,O_O^{\times} \rightarrow 2\,V_Y''' + 3\,V_O^{\bullet\bullet} + Y_2O_3 \tag{3.5}$$

Table 3.4: Energies of Frenkel and Schottky disorder in Bi_3YO_6

Type	Eqn.	Energy /eV
O Frenkel	3.1	0.54
Bi Frenkel	3.2	25.93
Bi_3YO_6 Full Schottky	3.3	15.93
Bi_2O_3 Schottky-type	3.4	10.56
Y_2O_3 Schottky-type	3.5	11.60

The resulting defect formation energies are given in Table 3.4 and indicate two main features. First, the results suggest that cation Frenkel and all the Schottky-type defects are highly unlikely, which agrees well with experiment. Second, oxygen Frenkel disorder is clearly the most favourable intrinsic defect. This is consistent with our structural analysis and indicates a highly mobile oxygen sub-lattice in the Bi_3YO_6 system at higher temperatures.

3.3.4 Dopant Incorporation

Dopant cations can be substituted into Bi_3YO_6. Our simulation methods can generate quantitative estimates of the relative energies of different mechanisms of dopant incorporation or 'solution'. Although the prediction of the maximum amount of dopant that can be incorporated is less straightforward, our results can provide useful trends relating to the solubility of dopant species. This approach has been applied successfully to a range of oxides including Bi_2WO_6 [57, 101, 104, 105]. We have therefore examined a wide range of dopants in Bi_3YO_6, including monovalent (e.g., Li^+ and Na^+), divalent (e.g., Sr^{2+} and Mg^{2+}), and trivalent (e.g., La^{3+} and Yb^{3+}) ions. The potentials used to model these dopants are listed in Appendix E.

Doping with aliovalent (donor or acceptor) ions requires the creation of charge-compensating defects. For monovalent and divalent ions this involves the creation of oxygen vacancies. For tetravalent cations two charge compensation mechanisms

are possible, an oxygen interstitial or a cation vacancy. Our calculations indicated that the former was preferred. The defect equations for the incorporation reactions for M^{+}, M^{2+} and M^{3+} are given in the following equations:

M^{+} Dopant

$$\frac{1}{2}M_2O + Bi_{Bi}^{\times} + O_O^{\times} \rightarrow M_{Bi}'' + V_O^{\bullet\bullet} + \frac{1}{2}Bi_2O_3 \tag{3.6}$$

M^{2+} dopant

$$MO + Bi_{Bi}^{\times} + \frac{1}{2}O_O^{\times} \rightarrow M_{Bi}' + \frac{1}{2}V_O^{\bullet\bullet} + \frac{1}{2}Bi_2O_3 \tag{3.7}$$

M^{3+} dopant

$$M_2O_3 + Bi_{Bi}^{\times} \rightarrow M_{Bi}^{\times} + \frac{1}{2}Bi_2O_3 \tag{3.8}$$

The 'solution' energies are calculated from these equations by combining the corresponding defect and lattice energies. Their is a degree of uncertainty of the lattice energies used to calculate the solution energies and relative trends should be considered more significant. The potentials used for the dopant ions are those used on the binary oxides. The results of the doping study are presented in Table 3.5, and as a function of ionic radius in Figure 3.10. In our analysis we have used the 6 coordinate effective ionic radii as 8 coordinate values are not available for all lanthanides.

Examination of the results reveal several key points. The most favourable dopants are the larger trivalent dopant ions (Nd^{3+} and La^{3+}). This trend can be explained using ion-size arguments: Y^{3+} and Bi^{3+} have ionic radii of 0.9Å and 1.03Å respectively, and the dopants that are most favourable have similar ionic radii (Nd^{3+} = 0.98Å, La^{3+} = 1.03Å). Our calculations also predict that Gd^{3+} and Yb^{3+} may also be favourable trivalent dopants within this phase. The divalent dopants show a similar ion size relationship, with Ca^{2+} and Sr^{2+} more favourable than that of the smaller dopant ion Mg^{2+}. The monovalent Li^{+} and Na^{+} dopants are highly unfavourable, suggesting that such doping in Bi_3YO_6 would not be significant.

Table 3.5: Calculated solution energies of dopants in Bi_3YO_6

Dopant	Solution Energy /eV
Li^+	7.03
Na^+	4.21
Mg^{2+}	2.10
Ca^{2+}	0.41
Sr^{2+}	0.21
Pb^{2+}	-0.28
Ba^{2+}	0.56
Ga^{3+}	1.94
Sc^{3+}	0.51
Yb^{3+}	-0.29
Gd^{3+}	-0.58
Nd^{3+}	-1.09
La^{3+}	-1.00

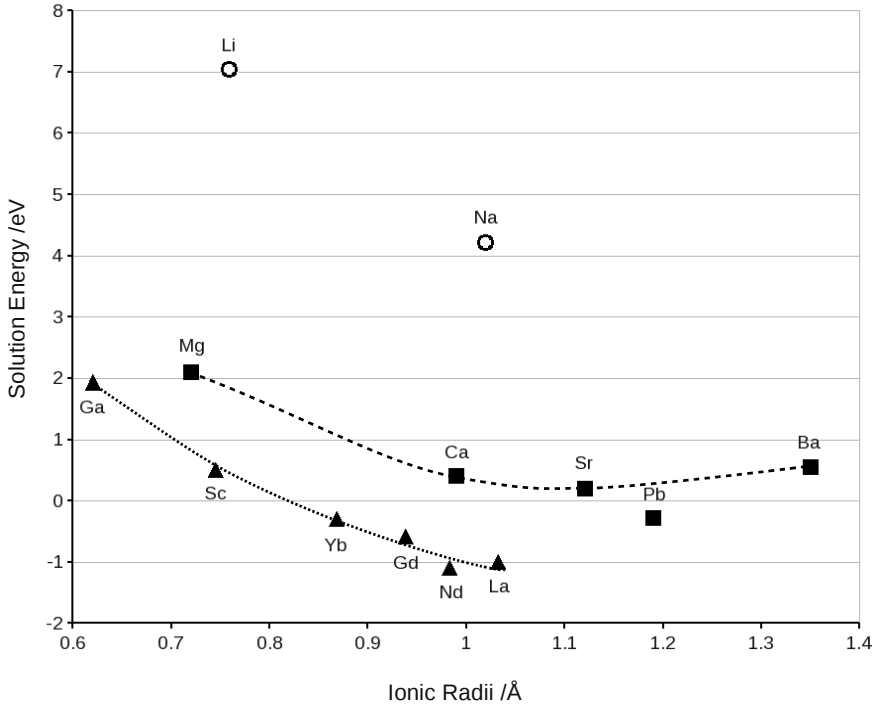

Figure 3.10: Calculated solution energies as a function of dopant ionic radius for Bi_3YO_6 (circle = 1+ cations, triangle = 2+ cations, square = 3+ cations, lines are guide to the eye only

An interesting result is that of Pb^{2+}. This is the most favourable of the divalent ions, meaning doping with this ion would create a higher concentration of oxygen vacancies. Preliminary experimental work has indicated that Pb^{2+}-doping of δ-Bi_2O_3-type phases is possible and shows some of the highest oxide ion conductivities observed for a doped δ-Bi_2O_3 phases. This behaviour can be explained not only by the creation of the charge compensating oxygen vacancy, but also some of the characteristics of the Pb^{2+} ion being very similar to that of the Bi^{3+} ion with respect to ion size and the existence of a lone pair. The lone pair of Bi^{3+} has been thought to impact favourably upon the oxide ion conduction in δ-Bi_2O_3 and retaining the lone pair when doping could lead to higher oxide conduction. Our result suggests that Pb-doped Bi_2O_3 phases warrants further experimental investigation.

3.4 Structural Modelling of $Bi_{28}Re_2O_{49}$

3.4.1 Introduction

The replacement of Bi with M^{6+} ions in Bi_2O_3 has shown to lead to the incorporation of MO_4^{2-} moieties [106–113] and these doped systems have shown low temperature oxide-ion conduction. Further studies of these phases continued with co-doping with M^{5+} and M^{7+} dopants. A new Re^{7+} doped Bi_2O_3 phase, $Bi_{28}Re_2O_{49}$, has been synthsised and characterised by Greaves et al [114]. Analysis of this phase showed a number of interesting features. First, $Bi_{28}Re_2O_{49}$ was measured to have higher oxide ion conductivity at low temperatures than Bi_3YO_6, with an observed activation energy of 0.62 eV and oxide-ion conductivity of 5.4 x 10^{-4} S cm^{-1} at 400°C [114]. Second, to compensate for charge disparity, the incorporation of Re^{7+} was suggested to exist in the form of tetrahedra ReO_4^-, and ReO_6^{5-} octahedra. However, Greaves et al. [114] reported that the exact oxygen arrangement around the Re^{7+} ions was difficult to obtain, and proposed that the high conductivity of $Bi_{28}Re_2O_{49}$ was due to mechanism that includes the two configurations of Re-O.

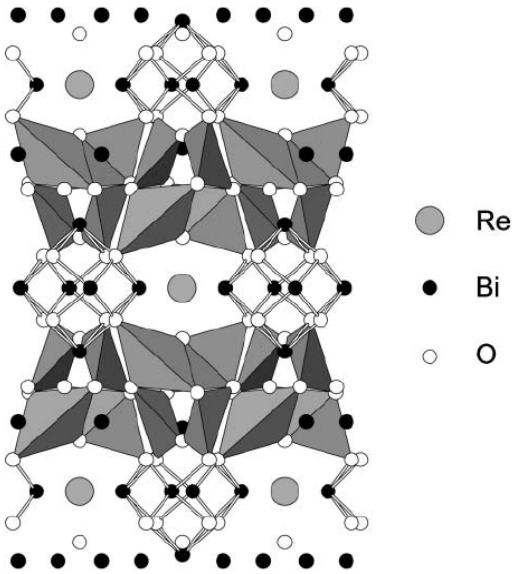

Figure 3.11: Experimental structure of $Bi_{28}Re_2O_{49}$ [114] viewed along [100] showing the BiO_4e trigonal bipyramids and the BiO bonds in the BiO_4e square pyramids. The O atoms bonded to Re are not shown.

The aim of this preliminary study is to develop an interatomic potential model for this highly complex phase.

3.4.2 Crystal Structure and Modelling of $Bi_{28}Re_2O_{49}$

The $Bi_{28}Re_2O_{49}$ structure has not yet been fully determined by experimental work using neutron powder diffraction (NPD), IR and K-edge X-ray adsorption spectra, although the combination of the three techniques does give an insight into its structure. NPD has shown that the material has a tetragonal superstructure of the cubic fluorite unit cell with space group I4/m, a = 8.7216(1) Å, c = 17.4177(2) Å (Table 3.6). Within this superstructure there exists an ordered framework of BiO_4: trigonal bipyramids and square pyramids with discrete Re-oxoanions at the origin and centre of the unit cell, as shown in Figure 3.11. Infra-red spectra and Re K-edge X-ray adsorption spectra [114] confirmed the presence of tetrahedral ReO_4^- and octahedral ReO_6^{5-} species in the ratio 3:1 on the oxoanion sites.

The published co-ordinates, listed in Table 3.6, are derived from NPD data only and

Table 3.6: Refined atomic parameters for $Bi_{28}Re_2O_{49}$ from NPD at 298K [114]

Atom	x	y	z	Cell Occupancy
Re	0	0	0.0100(6)	2
Bi1	0.2107(3)	0.4491(2)	0	8
Bi2	0.2988(2)	0.1056(2)	0.1711(8)	16
Bi3	0.5	0.5	0.1557(2)	4
O1	0.5	0	0.1259(2)	8
O2	0.0739(2)	0.2517(3)	0.2567(1)	16
O3	0.3253(3)	0.6302(3)	0.0780(1)	16
O4	0.020(2)	0.232(2)	0.015(2)	2
O5	0	0	0.1126(6)	2
O6	0.015(3)	0.179(3)	0.036(2)	2
O7	0.995(2)	0.206(3)	0.012(3)	2

I4/m; a = 8.7212(1) Å; c = 17.4177(2) Å

therefore give an average structure around the Re ions within the unit cell, which as stated previously, are thought to be made up of a combination of tetrahedra and octahedra. Also, it can be seen that the NPD data for $Bi_{28}Re_2O_{49}$ only specifies 48 oxygen sites.

Therefore our initial modelling work has an ideal stoichiometric structure with fully occupied sites. This structure was a 2 x 2 x 1 supercell with eight Re sites. The Re sites had either ReO_4^- tetrahedral or a ReO_6^{5-} octahedral coordination. The final ideal structure is shown in Figure 3.12. Variations of this strucutre with differing ReO_6^{5-} octahedron separation and ReO_4^- tetrahedral orientations were also created to allow the testing of the potential models.

The development of a potential model for this phase started by Bi^{3+}- and O^{2-}-related interactions taken from published work by Islam et al. [101] on Bi_2WO_6 and the $O^{2-}\cdots O^{2-}$ interaction from work by Minervini et al. [39], listed in Table 3.7. A $Re^{6+}\cdots O^{2-}$ potential was developed by Cormack et al. [115] when investigating the ReO_3 structure, which was used as the basis for the initial $Re^{7+}\cdots O^{2-}$ potential.

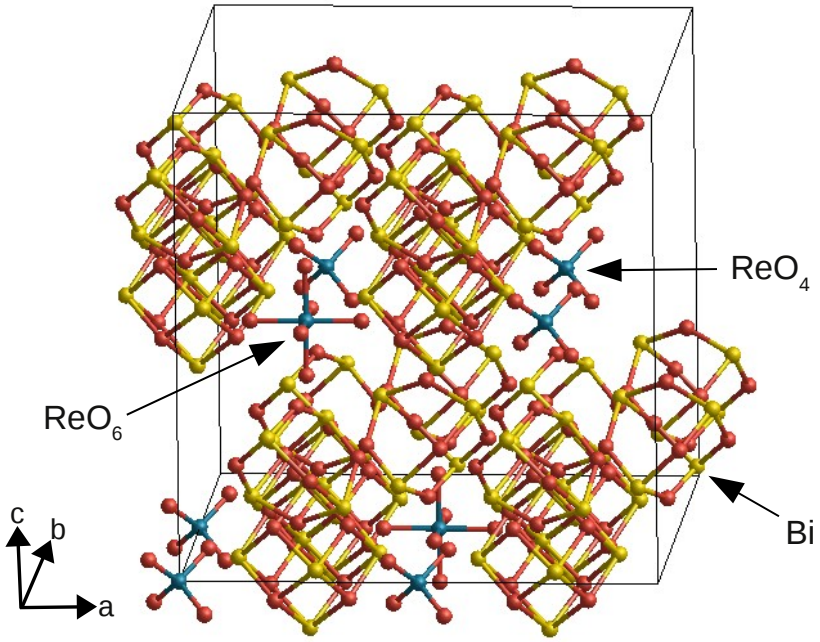

Figure 3.12: Simulated $Bi_{112}Re_8O_{196}$ supercell showing ReO_4 tetrahedra and ReO_6 octahedra.

Table 3.7: Interatomic potentials for $Bi_{28}Re_2O_{49}$

(i) short-range

Interaction	A (eV)	ρ (Å)	C (eV Å^6)	Ref
$Bi^{3+} \cdots Bi^{3+}$	24244.5	0.3284	0.0	[101]
$Bi^{3+} \cdots O^{2-}$	49529.35	0.2223	0.0	[101]
$O^{2-} \cdots O^{2-}$	9547.96	0.2192	32.0	[39]
$Re^{7+} \cdots O^{2-}$	741.39	0.4838	0.0	[115]
$Re^{7+} \cdots O^{2-}$	913.201	0.4383	0.0	This Study

(ii) shell model

Species	$Y(e)$	k (eV Å$^{-}{}_2$)
Bi^{3+}	-5.51	359.55
O^{2-}	-2.04	6.30
Re^{7+}	6.89	7.69

Table 3.8: Experimental and calculated cell parameters for Bi_3ReO_8 and La_3ReO_8

Structure	Parameter	Expt.	Calc.
Bi_3ReO_8			
	a/Å	11.59	11.56
	b/Å	11.59	11.56
	c/Å	11.59	11.56
	$\alpha/^\circ$	90.0	90.0
	$\beta/^\circ$	90.0	90.0
	$\gamma/^\circ$	90.0	90.0
La_3ReO_8			
	a/Å	7.76	7.81
	b/Å	7.78	7.81
	c/Å	5.93	6.84
	$\alpha/^\circ$	90.0	90.0
	$\beta/^\circ$	90.0	90.0
	$\gamma/^\circ$	111.1	114.0

Before the $Re^{7+}\cdots O^{2-}$ potential was used in the modelling of $Bi_{24}Re_2O_{49}$ the potential was empirically fitted to two fully characterised Re^{7+} structures Bi_3ReO_8 and La_3ReO_8; the experimental and calculated structures are presented in Table 3.8, showing good agreement. This process, detailed in appendices A and B, produced candidate potential models.

The refined potential for $Bi_{28}Re_2O_{49}$ proved stable with respect to varying the separation between the ReO_6^{5-} octahedra. However, calculation of the phonon dispersion curve for $Bi_{28}Re_2O_{49}$, revealed imaginary phonons and non-convergence with respect to oxygen vacancy calculations.

In summary, our preliminary study of the new $Bi_{28}Re_2O_{49}$ material has not produced a satisfactory interatomic potential model. This is largely due to the complexity of the structure in which the local Re coordinations are not fully characterised and to the high valence state of Re. Future work should include further experimental characterisation of the crystal structure and DFT-based structural optimisations.

3.5 Chapter Summary

Atomistic simulation techniques have been used to study the structural, defect, and dopant properties of Bi_3YO_6, which has potential SOFC and ceramic membrane applications. The following main points can be taken from this study.

(i) A new potential model for Bi_3YO_6 has been developed in which the lowest energy vacancy-ordering model is found to be the $\langle 110 \rangle$ configuration. A supercell with random distribution of oxygen vacancies gave structural reproduction of the system to within 1% of experimental values. However, our results suggest that the lowest energy vacancy configuration identified for Bi_3YO_6 is a 2 x 2 x 2 supercell containing a combination of $\langle 111 \rangle$ and $\langle 110 \rangle$ vacancy configurations, previously found to be the lowest energy configuration for pure δ-Bi_2O_3 by ab-initio calculations.

(ii) The intrinsic defect energies were calculated and it was found that the Schottky and cation Frenkel defects are energetically unfavourable. However the oxygen Frenkel energy is very low (0.54 eV) and indicates a highly mobile oxygen sub-lattice as observed experimentally.

(iii) The most energetically favoured dopants are predicted to be Nd^{3+}, La^{3+} and Pb^{2+}. Doping with Pb^{2+} is an interesting result as this would create a higher oxygen vacancy concentration than in pure δ-Bi_2O_3, but also preserve the polarisable nature of the cation sublattice, that is thought to influence oxide ion migration.

Chapter 4

Defect Chemistry and Proton-Dopant Association in $BaZrO_3$, $BaPrO_3$ and $BaThO_3$

4.1 Experimental Background

Solid-state proton conductors based on cerate and zirconate perovskite oxides have attracted considerable attention for a range of electrochemical applications, such as fuel cells, seperation membranes and steam electrolysers [5, 7, 16, 17, 25, 116–119]. As mentioned in section 1.4, such oxide materials are particularly attractive as electrolytes for solid oxide fuel cells (SOFCs) operating at intermediate temperatures (400-700°C), in contrast to high temperature operation (>900°C) of SOFCs based on the Y/ZrO_2 oxide-ion conductor.

Of the known perovskite-type proton conductors, there has been considerable experimental [120–142] and computational [104, 143–150] interest in acceptor-doped $BaZrO_3$ due to its high proton conductivity in a cubic structure coupled with good chemical and mechanical stability. The proton mobility in Y-doped $BaZrO_3$ is among one of the highest ever reported for a perovskite-type proton conductor, and has the potential to operate at lower temperatures than the conventional SOFC electrolyte. There has also been recent interest in some less-studied Ba-based perovskites as potential proton conductors including acceptor-doped $BaPrO_3$ and $BaThO_3$ [151–159], but the defect, thermodynamic and conduction properties of these materials are not fully characterised.

It is known that defect reactions and atomistic diffusion mechanisms underpin the fundamental understanding of proton conduction behaviour. However, there is often limited atomic-scale information on complex ceramic oxides, such as lattice defects, local proton sites and the extent of interactions between the dopant ion and the protonic defect leading to possible proton "trapping". Yamazaki et al. [135] have reported thermogravimetry studies of the water incorporation reaction in Y-doped $BaZrO_3$ and determine hydration enthalpies that are substantially smaller than those reported previously. Recent Neutron-Spin-Echo experiments [126] on hydrated $BaZr_{0.90}Y_{0.10}O_{2.95}$ report data that are indicative of trapping effects in which the proton spends an extended time in the vicinity of the Y dopant before

Table 4.1: Interatomic potentials and shell model parameters for $BaZrO_3$, $BaPrO_3$, and $BaThO_3$

(i) short-range

Interaction	A (eV)	ρ (Å)	C (eV Å^6)
$Ba^{2+} \cdots O^{2-}$	931.700	0.3949	0.000
$Zr^{4+} \cdots O^{2-}$	985.869	0.3760	0.000
$Pr^{4+} \cdots O^{2-}$	1925.382	0.3511	21.152
$Th^{4+} \cdots O^{2-}$	1139.700	0.3944	0.000
$O^{2-} \cdots O^{2-}$	22764.300	0.1490	27.890

(ii) shell model

Species	$Y(e)$	k (eV Å^{-2})
Ba^{2+}	1.460	14.800
Zr^{4+}	1.350	169.617
Pr^{4+}	7.7	291
Th^{4+}	7.280	193.000
O^{2-}	-2.077	27.300

further proton diffusion.

This chapter presents recent computational studies of topical proton-conducting perovskites based upon $BaZrO_3$, $BaPrO_3$ and $BaThO_3$ with an examination of trends and direct comparison with experimental data where available. Emphasis here is placed on probing the defect chemistry, proton sites, dopant-OH association and oxygen ion migration on the atomic scale.

4.2 Crystal Structure and Potentials

The interatomic potential and shell model parameters for $BaZrO_3$, $BaPrO_3$, and $BaThO_3$ are listed in Table 4.1. The parameters for Ba-O, Zr-O, Th-O and O-O have been transferred from previous simulation studies [160–162], and those for Pr-O have been derived empirically for this study.

Table 4.2: Parameters for O-H interaction

Morse potential	D (eV)	β (Å^{-1})	r_0 (Å)
O$\cdots$H	7.0525	2.1986	0.9485
Buckingham potential	A (eV)	ρ (Å)	C (eV Å^6)
O$\cdots$H	311.97	0.25	0

For the protonic defect, the O-H interaction was modelled using an attractive Morse potential

$$V(r) = D\{1 - exp[-\beta(r - r_0)]\}^2 \tag{4.1}$$

using parameters (Table 4.2) developed from ab initio quantum mechanical cluster calculations, with a point charge representation of the surrounding lattice [163]. The dipole of the hydroxyl species was distributed across both ions to give an overall charge of -1 with O assigned -1.4263 and H +0.4263. An additional Buckingham potential describing the interaction between the hydroxyl group and the lattice ions was taken from previous studies of water incorporation in silicates[164]. This simulation approach has been applied successfully to other proton-conducting perovskites [165–168], and more recently, to water incorporation in Si/Ge-apatites [169].

The starting point of the study was to reproduce the experimentally observed crystal structures. The unit cell dimensions and ion positions were equilibrated under constant pressure conditions. The calculated structures of cubic $BaZrO_3$ and orthorhombic $BaPrO_3$ and $BaThO_3$ are compared with experiment in Table 4.3. The unit cell parameters change only slightly on relaxation of the structures. The differences in the observed and calculated lattice parameters and bond lengths are all within 0.09Å, and in many cases less than 0.03Å, indicating that the potentials reproduce successfully these perovskite structures.

Table 4.3: Experimental and calculated lattice parameters and mean bond lengths for $BaZrO_3$, $BaPrO_3$ and $BaThO_3$

Parameter	Exp	Calc	δ
$BaZrO_3$ [a]			
a=b=c/Å	4.199	4.188	-0.011
Ba-O/Å	2.969	2.961	-0.008
Zr-O/Å	2.099	2.094	-0.005
$BaPrO_3$ [b]			
a/Å	6.181	6.213	-0.032
b/Å	6.214	6.221	-0.007
c/Å	8.722	8.789	-0.067
Ba-O1/Å	3.114	3.111	-0.003
Ba-O2/Å	3.016	3.110	0.093
Pr-O1/Å	2.227	2.205	0.022
Pr-O2/Å	2.223	2.203	0.020
$BaThO_3$ [c]			
a/Å	6.345	6.316	-0.029
b/Å	6.376	6.346	-0.029
c/Å	8.992	8.958	-0.034
Ba-O1/Å	3.200	3.176	-0.024
Ba-O2/Å	3.198	3.175	0.023
Th-O1/Å	2.294	2.265	0.029
Th-O2/Å	2.291	2.263	0.028

[a][170] [b][171] [c][172]

4.3 Intrinsic Defects and Redox Reactions

Energies of isolated point defects (vacancies and interstitials) were then calculated for the three structures. The isolated defect energies were combined to give the energies of formation of Frenkel and Schottky defects based on the following equations.

Ba Frenkel:

$$Ba_{Ba}^{\times} \rightarrow V_{Ba}'' + Ba_i^{\bullet\bullet} \tag{4.2}$$

M Frenkel:

$$\mathrm{M}_{\mathrm{M}}^{\times} \rightarrow \mathrm{V}_{\mathrm{M}}^{4\prime} + \mathrm{M}_{\mathrm{i}}^{4\bullet} \tag{4.3}$$

O Frenkel:

$$\mathrm{O}_{\mathrm{O}}^{\times} \rightarrow \mathrm{V}_{\mathrm{O}}^{\bullet\bullet} + \mathrm{O}_{\mathrm{i}}^{\prime\prime} \tag{4.4}$$

Schottky:

$$\mathrm{Ba}_{\mathrm{Ba}}^{\times} + \mathrm{M}_{\mathrm{M}}^{\times} + 3\,\mathrm{O}_{\mathrm{O}}^{\times} \rightarrow \mathrm{V}_{\mathrm{Ba}}^{\prime\prime} + \mathrm{V}_{\mathrm{M}}^{4\prime} + 3\,\mathrm{V}_{\mathrm{O}}^{\bullet\bullet} + \mathrm{BaMO}_3 \tag{4.5}$$

BaO Schottky-type:

$$\mathrm{Ba}_{\mathrm{Ba}}^{\times} + \mathrm{O}_{\mathrm{O}}^{\times} \rightarrow \mathrm{V}_{\mathrm{Ba}}^{\prime\prime} + \mathrm{V}_{\mathrm{O}}^{\bullet\bullet} + \mathrm{BaO} \tag{4.6}$$

MO Schottky-type:

$$\mathrm{M}_{\mathrm{M}}^{\times} + 2\,\mathrm{O}_{\mathrm{O}}^{\times} \rightarrow \mathrm{V}_{\mathrm{M}}^{4\prime} + 2\,\mathrm{V}_{\mathrm{O}}^{\bullet\bullet} + \mathrm{ZrO}_2 \tag{4.7}$$

The resulting energies are listed in Table 4.4 which reveal two main points. First, the creation of Frenkel defects is associated with substantial amounts of energy, confirming that the close-packed perovskite structure is highly unlikely to accommodate ion interstitials. Second, the most favourable energy is found for the BaO Schottky-type disorder for all systems, with the lowest value of 2.13 eV for $BaPrO_3$. This suggests the possible loss of BaO at very high temperatures. It has been found that $BaPrO_3$-based compounds are unstable towards even mild reduction [151].

Most applications of proton conductors require them to be used under a range of redox (reducing or oxidising) conditions. For the undoped system, the following reaction for reduction can be considered involving the creation of oxygen vacancies and electronic defects:

$$\mathrm{O}_{\mathrm{O}}^{\times} \rightarrow \mathrm{V}_{\mathrm{O}}^{\bullet\bullet} + \frac{1}{2}\mathrm{O}_{2\,(\mathrm{g})} + 2\mathrm{e}^{\prime} \tag{4.8}$$

For an extrinsic system, where oxygen vacancies already exist due to acceptor

Table 4.4: Energies of Frenkel and Schottky disorder in $BaZrO_3$, $BaPrO_3$ and $BaThO_3$

Type	Energy (eV/defect) $BaZrO_3$	$BaPrO_3$	$BaThO_3$
Ba Frenkel	6.97	5.96	4.75
M Frenkel	10.22	12.78	17.51
O Frenkel	5.58	4.89	4.25
$BaMO_3$ Full Schottky	3.20	4.49	4.09
BaO Schottky-type	2.80	2.13	2.67
MO Schottky-type	3.75	5.30	5.26

Table 4.5: Energies of redox reactions in $BaZrO_3$, $BaPrO_3$ and $BaThO_3$

Type	Energy (eV/electronic defect) $BaZrO_3$	$BaPrO_3$	$BaThO_3$
Oxidation	2.90	2.15	2.37
Reduction	6.23	1.14	9.36

doping, oxidation can occur via the following reaction:

$$V_O^{\bullet\bullet} + \frac{1}{2}O_{2\,(g)} \rightarrow O_O^{\times} + 2h^{\bullet} \tag{4.9}$$

in which the oxygen vacancies are filled to create electron holes ($h^{\bullet}$). Our approach to electronic defects in $BaZrO_3$, $BaPrO_3$ and $BaThO_3$ follows that used for the $BaCeO_3$ and $SrCeO_3$ perovskites [166, 168], in which the hole centres are modelled as O^- and the electron centres (e') as M^{3+}. Using these electronic terms, the energies of the redox reactions were calculated and are given in Table 4.5. Owing to the uncertainties in the free-ion terms employed, we must be cautious in giving detailed interpretations.

The results show that the lowest oxidation and reduction energies are found for the $BaPrO_3$ system, suggesting a greater concentration of electronic defects in this ma-

terial. For the doped material, p-type conductivity will be exhibited with increasing oxygen partial pressures. Indeed, Furøy et al. [151] show that Gd-doped $BaPrO_3$ is dominated by electronic holes at lower temperatures in oxidising atmospheres, making it a p-type conductor. Similarly, Magraso et al. [158] find that Gd-doped $BaPrO_3$ is largely a p-type conductor.

The lowest defect reaction energy is for intrinsic reduction of $BaPrO_3$ with the formation of oxygen vacancies and electronic species (Pr^{3+}). Furøy et al. [151] find that the $BaPrO_3$ system is unstable towards reduction, while photoemission spectroscopy measurements of Mimuro et al. [157] indicate the presence of Pr^{3+} in the intrinsic region.

The high reduction energies in $BaZrO_3$ and $BaThO_3$ indicates greater resistance to reduction than oxidation. We note that entropic effects need to be included in our calculations to derive a quantitative relationship between oxygen partial pressure and defect concentration, which is a topic for further study. In general, these results are consistent with experimental findings of the materials, which show mixed ionic/electronic conductivity and that p-type electronic conductivity increases with increasing oxygen activity especially for doped $BaPrO_3$.

4.4 Dopant Incorporation

It is well established that cation doping in perovskite-type ion conductors is a key step to proton incorporation in wet/hydrogen atmospheres. Trivalent ions doped on to the Ba and M sites can be represented by the following reactions (where Ln = Lanthanide):

$$\frac{1}{2}Ln_2O_3 + M_M^{\times} + \frac{1}{2}O_O^{\times} \rightarrow Ln_M' + \frac{1}{2}V_O^{\bullet\bullet} + MO_2 \tag{4.10}$$

Table 4.6: Calculated solution energies (in eV) for the $BaMO_3$ perovskites

		$BaZrO_3$		$BaPrO_3$		$BaThO_3$	
Dopant	Ionic Radius /Å	Ba-site	Zr-site	Ba-site	Pr-site	Ba-site	Th-site
Sc^{3+}	0.75	5.96	2.16	5.09	3.21	7.51	2.83
In^{3+}	0.80	5.23	2.20	4.54	3.21	5.84	2.89
Yb^{3+}	0.87	3.80	1.57	4.09	2.51	4.87	2.28
Y^{3+}	0.90	3.30	1.51	3.94	2.40	4.33	2.23
Gd^{3+}	0.94	2.76	1.49	3.45	2.30	3.97	2.21
Nd^{3+}	0.98	2.20	1.56	3.00	2.27	3.35	2.30
La^{3+}	1.03	2.74	2.69	3.57	3.29	3.84	3.43

$$\frac{1}{2}Ln_2O_3 + \frac{3}{2}Ba^{\times}_{Ba} \rightarrow Ln^{\bullet}_{Ba} + \frac{1}{2}V''_{Ba} + \frac{3}{2}BaO \tag{4.11}$$

The dopant solution energies are presented in Table **??** and in Figures 4.1, 4.2 and 4.3 as a function of dopant ion size[173]. The potentials used for dopant incorporation calculations can be found in Appendix E.

Examination of the results show a number of key points. In general, doping onto the M site (Zr, Pr, Th) is more favourable than that of the Ba site. For all three phases, the larger dopant cations (Gd, Nd) have more favourable solution energies than that of the smaller cations (Sc, Yb). These general observations can be explained by idea of 'mismatch' of ion size, in which substitution is more favourable when the size of the 'host' site is similar to that of the ionic radius of the dopant ion (where Ba = 1.6Å, Zr = 0.72Å, Th = 0.94Å and Pr = 0.99Å). In all three systems the most favourable dopant ions are Yb, Y, Gd, and Nd. This is in accordance with experimental work as Yb_2O_3[157], Y_2O_3[174], Gd_2O_3[151] and Nd_2O_3[175] are common acceptor dopants within these $BaMO_3$ systems when stimulating proton conduction due to the formation of the necessary oxygen vacancies.

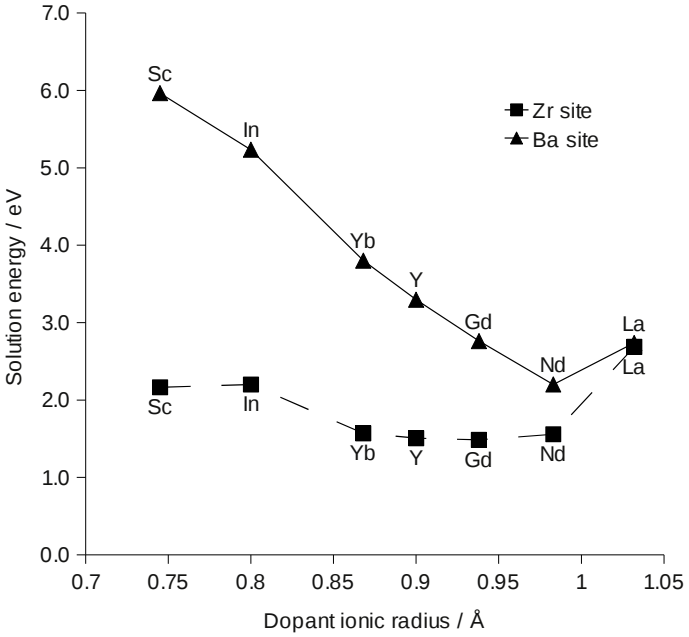

Figure 4.1: Calculated solution energies as a function of dopant ionic radius in $BaZrO_3$

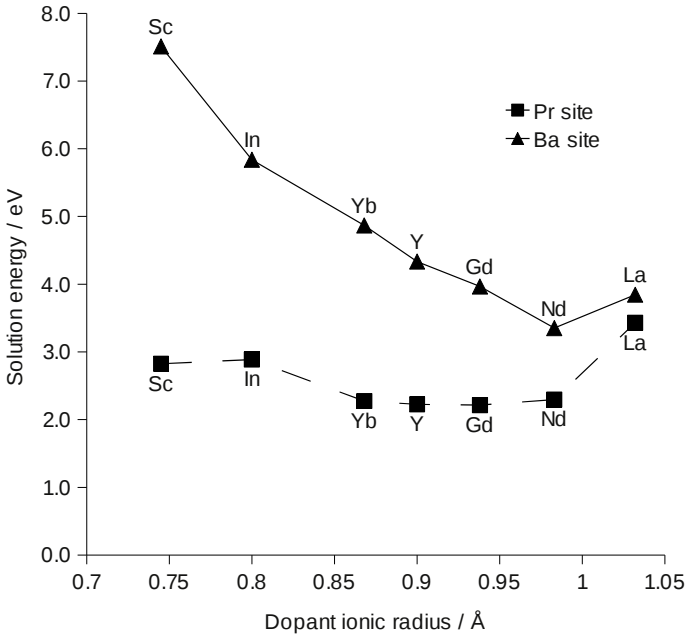

Figure 4.2: Calculated solution energies as a function of dopant ionic radius in $BaPrO_3$

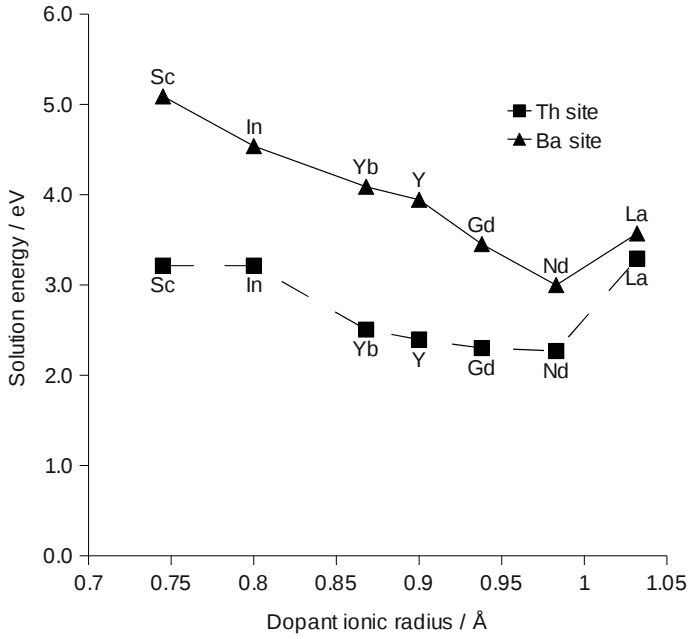

Figure 4.3: Calculated solution energies as a function of dopant ionic radius in $BaThO_3$

4.5 Water Incorporation and Protonic Defect

The incorporation of water into the perovskite structure is achieved by treatment in water vapour, in which the oxygen vacancies, generated by acceptor doping, are replaced by protonic defects (in the form of hydroxyl ions) as shown by the following equation and Figure 4.4.

$$H_2O + O_O^{\times} + V_O^{\bullet\bullet} \longrightarrow 2\,OH_O^{\bullet} \tag{4.12}$$

Previous computational studies [143, 144, 148, 176] have indicated that proton conduction in perovskites involves (i) proton hopping between neighbouring oxygens (Grotthus mechanism) aided by local lattice softening and (ii) rotational motion of the hydroxyl group. Hence, the characterisation of the local structure and O-H configurations is important, but is not straightforward from diffraction experiments.

As with previous studies [165, 168], our simulation techniques can be used to probe

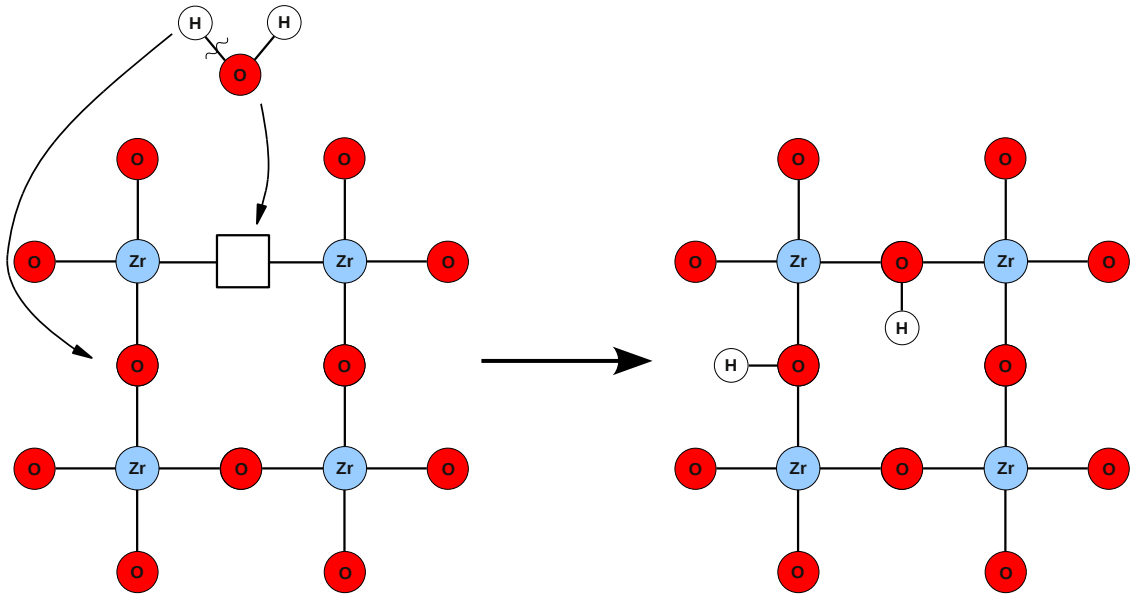

Figure 4.4: Schematic of water incorporation process based on equation 4.12

the proton site and examine the most energetically favourable O-H configuration. The simulations suggest that the equilibrium O-H bond lies perpendicular to the line between the two adjacent Zr^{4+}, Pr^{4+} or Th^{4+} ions (as shown in Figure 4.5 for $BaZrO_3$). This configuration seems to maximise both the H-Ba^{2+} and the H-M^{4+} distances.

Unlike average structural techniques, our atomistic simulations reveal local ion relaxations around the protonic defect (illustrated in Figure 4.5b) with a local distortion from cubic symmetry for $BaZrO_3$. An equilibrium O-H distance of 0.98Å is found, which lies close to accepted O-H bond lengths in perovskites [25, 117]. Our calculated position for the H atom in $BaZrO_3$ is (0.5, 0.275, 0.0). These results are consistant with the deuterium position refined from neutron powder diffraction data collected on deuterated and dry samples of $BaZr_{0.5}In_{0.5}O_{2.75}$ at 5K and room temperature [123].

Based on reaction (4.12), the energy of water incorporation, or hydration energy, (E_{H_2O}) can be calculated by using the following equation:

$$E_{H_2O} = 2E_{OH} - E_{V_O^{\bullet\bullet}} + E_{PT} \tag{4.13}$$

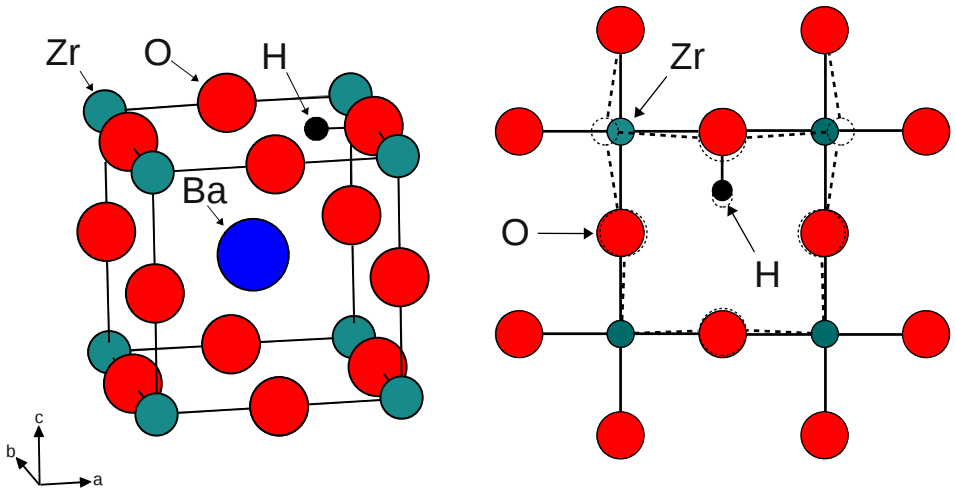

(a) **(b)**

Figure 4.5: Schematic of equilibrium O-H configuration in $BaZrO_3$ (a) Unit cell of cubic structure (b) relaxed (dotted line) and unrelaxed local structure in the a-b plane

where E_{OH} is the energy associated with substitution of O^{2-} with an OH^- group, $E_{V_O^{\bullet\bullet}}$ is the oxygen vacancy energy, and E_{PT} is the energy of the gas phase reaction $O^{2-} + H_2O = 2\,OH^-$. The latter term is estimated from the difference between proton affinities of O^{2-} and OH^-, and discussed in detail by Catlow and co-workers [177, 178].

The calculated hydration energies are listed in Table 4.7 and indicate two key features. First, E_{H_2O} is negative for all three materials, which suggests that the materials will be dominated by protons at low temperatures and oxygen vacancies at high temperatures. The magnitude of E_{H_2O} is notably less exothermic for $BaZrO_3$ than that for $BaPrO_3$ and $BaThO_3$. Yamazaki et al.[135] determine hydration enthalpies at low temperature for Y doped $BaZrO_3$ of -22 to -26 kJmol^{-1} (-0.22 to -0.27 eV) with varying dopant levels of 20 – 40%. As with our calculated value, these are significantly smaller in magnitude than the previously reported values for Y-doped $BaZrO_3$ of -79.4 to -93.3 kJmol^{-1} (-0.82 to -0.97 eV) [120]. Yamazaki et al.[135] indicate that the smaller negative values in comparison with previous data are attributed to the restriction of the analysis to the low temperatures at which

electronic hole concentrations can be neglected.

Table 4.7: Defect and hydration energies for $BaZrO_3$, $BaPrO_3$ and $BaThO_3$

	$BaZrO_3$	$BaPrO_3$	$BaThO_3$
$E_{V_O^{\cdot\cdot}}$ /eV	18.56	19.01	17.76
E_{OH} /eV	15.11	14.67	14.10
Calc. E_{H_2O} /eV	-0.12	-1.45	-1.32
Exp. E_{H_2O} /eV	-0.22 to -0.27[a], -0.82 to -0.97[b]	-	-1.33[c]

[a][135], [b][120], [c][151]

For $BaPrO_3$, there is no experimental hydration enthalpy for direct comparison partly due to the dominance of electronic behaviour. Mimuro et al. [157] suggests that proton solubility increases with increasing dopant concentration in Yb-doped $BaPrO_3$, while Magraso et al.[158] find Gd-doped $BaPrO_3$ to be highly reactive under water, CO_2 and hydrogen containing atmospheres. Furthermore, Furøy et al.[151] calulated E_{H_2O} for 10% Nd doped $BaThO_3$ as -128 kJmol^{-1} (-1.33 eV), this shows excellent correlation with our results.

4.6 Proton-dopant Interactions

There has been some debate as to whether there is any significant association between the dopant ion and the protonic defect (hydroxyl ion at oxygen site), which may affect proton mobility. In an attempt to probe the question of proton-dopant association, we have extended our previous studies on $SrCeO_3$ [168] and $CaZrO_3$ [176] with a series of calculations on OH-dopant pairs in $BaZrO_3$, $BaPrO_3$ and $BaThO_3$ comprised of a hydroxyl ion and a neighbouring dopant substitutional (Figure 4.6). For this task, the simulation methods used here are well suited as they model accurately Coulomb and polarization energies, which are the predominant terms in any local association process. Work on the $LaGaO_3$ perovskite [179] suggests that in addition to the electrostatic attraction, the elastic energy term due to distortion of the crystal lattice upon introduction of different-sized cations

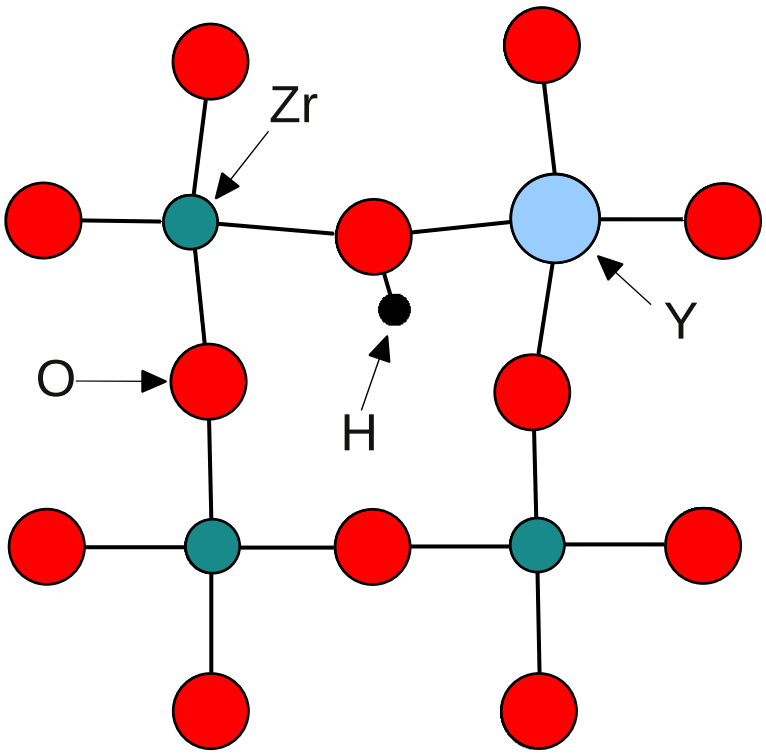

Figure 4.6: Calculated local structure for the $OH_O^{\bullet}-Y_{Zr}^{'}$ pair cluster in $BaZrO_3$ showing local lattice relaxation, in the a-b plane.

contributes to cluster formation.

With regard to the relaxed geometry, deviations from the equilibrium O-H configuration (shown in Figure 4.5) are found, corresponding to a shift of the H position towards a neighbouring oxygen and dopant ion (shown in Figure 4.6 for Y^{3+} in $BaZrO_3$ as an example). As in Figure 4.5b, the simulations reveal ion relaxations and local deviations from cubic symmetry in $BaZrO_3$.

The cluster binding energy (E_{bind}) for this configuration was calculated, which is defined as the difference between the energy of the cluster (E_{cluster}) and the sum of the energies of the corresponding isolated defects. This is given by the general relation:

$$E_{\text{bind}} = E_{\text{cluster}} - \left(\sum_{\text{component}} E_{\text{isolated defect}} \right) \tag{4.14}$$

where a negative value indicates that the cluster is stable with respect to the component isolated defects. For example, in the case of $BaZrO_3$ the binding energy is given by the relation:

$$E_{\text{bind}} = E(\text{OH}_{\text{O}}^{\bullet}\text{M}_{\text{Zr}}^{'}) - \{E(\text{M}_{\text{Zr}}^{'}) + E(\text{OH}_{\text{O}}^{\bullet})\} \tag{4.15}$$

Attention was focused on commonly used dopants in these materials, namely Sc, In, Y, Yb and Gd. The resulting energies (reported in Table 4.8 and Figure 4.7) predict that all the hydroxyl-dopant pairs are favourable configurations; the lowest binding energy is for Y and Gd and the strongest association is for Sc. These results suggest that proton mobility would be very sensitive to the type of acceptor dopant ion. It may be significant that a low binding energy is found for Y^{3+}, which is the most commonly used dopant in the $BaZrO_3$ proton conductor. It should be noted there is limited research relating to Gd-doped $BaZrO_3$ and our results suggest that Gd doping warrants further investigation.

Kreuer et al. [120] have investigated a range of alkaline-earth zirconates and titanates for potential electrochemical applications: they find that the system $BaZr_{1-x}Y_xO_{3-\delta}$ ($x = 0.1$) exhibits the highest proton mobility and the lowest activation enthalpy. In contrast, the lowest proton mobility and highest activation energy is found for Sc-doped $BaZrO_3$, for which we predict the strongest dopant-OH association. Our binding energy results for $BaPrO_3$ and $BaThO_3$ indicate extremely strong proton trapping by all of the acceptor dopants. This suggests significant impeding effects on long-range proton mobility, which would lead to low proton conductivity in doped $BaPrO_3$ and $BaThO_3$.

The interatomic distances between the M dopant and proton of the hydroxyl unit in the dopant-OH cluster have been analysed and are listed in Table 4.8. The analysis reveals that the distance between M and the proton (M-H) changes with respect to the host Zr, Pr and Th ions. The longest M-H distances are for the Gd and Y dopants, and this mirrors the variation in binding energy (Figure 4.7).

Table 4.8: Binding energy and dopant-proton (M-H) distances in the pair cluster (Figure 4.6) in $BaZrO_3$ and $BaPrO_3$

System	M^{3+}	ionic radius (Å)	Energy /eV	M-H (Å)	ΔM-H(Å)
$BaZrO_3$					
	Zr	0.72	-	2.65	0.00
	Sc	0.75	-0.74	2.25	-0.40
	In	0.80	-0.59	2.29	-0.36
	Yb	0.87	-0.38	2.36	-0.29
	Y	0.90	-0.28	2.41	-0.24
	Gd	0.94	-0.19	2.81	0.16
$BaPrO_3$					
	Pr	0.85	-	2.82	0.00
	Sc	0.75	-1.30	2.24	-0.58
	In	0.80	-1.19	2.27	-0.55
	Yb	0.87	-1.02	2.31	-0.51
	Y	0.90	-0.95	2.34	-0.48
	Gd	0.94	-0.88	2.37	-0.45
$BaThO_3$					
	Th	0.94	-	3.00	0.00
	Sc	0.75	-1.15	2.26	-0.74
	In	0.80	-1.05	2.29	-0.71
	Yb	0.87	-0.87	2.34	-0.66
	Y	0.90	-0.80	2.37	-0.63
	Gd	0.94	-0.72	2.40	-0.60

Interestingly, the largest dopant (Gd) in $BaZrO_3$ is the only case in which the OH bond does not swing towards the dopant ion, which can be related to the greater ion size mismatch between the Zr^{4+} and Gd^{3+} cations.

Although there are no quantitative experimental values for either $BaZrO_3$, $BaThO_3$ or $BaPrO_3$ for direct comparison, our calculated binding energies are in accord with proton "trapping" energies of about -0.2 and -0.4 eV for related Sc-doped $SrZrO_3$ and Yb-doped $SrCeO_3$ respectively, derived from muon spin relaxation (μSR) and quasi-elastic neutron scattering (QENS) experiments [180, 181]. In accord with our previous dopant-OH simulations on $SrZrO_3$, $CaZrO_3$[165, 176] and $SrCeO_3$[168], Bjorketun et al.[147] also find proton-dopant cluster formation in $BaZrO_3$ from DFT-based calculations. Moreover, recent Neutron-Spin-Echo (NSE) experiments

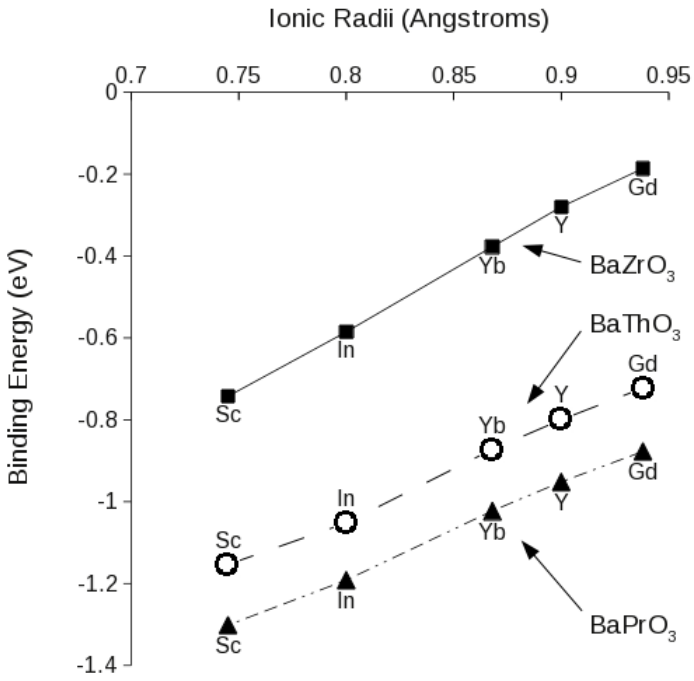

Figure 4.7: Dopant-OH binding energies as a function of dopant ion size

[126] on proton dynamics in hydrated $BaZr_{0.90}Y_{0.10}O_{2.95}$ indicate proton trapping in which the proton spends an extended times in the vicinity of the Y dopant ions before further diffusion.

4.7 Oxide-ion Migration

The oxygen vacancies required for incorporation of protons may also migrate, particularly at high temperature (> 600°C) when the exothermic incorporation of water is no longer favoured (eq.4.12). Whereas oxygen transport may be disadvantageous for certain applications, steam permeation (involving simultaneous diffusion of protons and oxygen vacancies) has been shown to inhibit coking of the anode in a proton conducting fuel cell operating on methane [182]. In this context, atomistic simulation of oxygen migration may greatly assist in our understanding of the energies and mechanistic features of oxygen transport in these $BaMO_3$ systems. Our simulation methods have previously been used to elucidate oxygen-ion

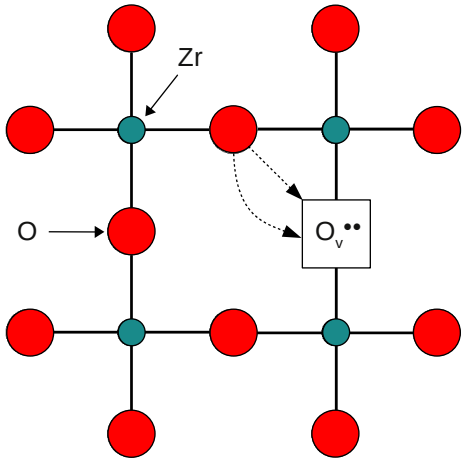

Figure 4.8: Schematic representation of the linear and curved path of oxygen migration in the a-b plane of the $BaMO_3$ perovskite

migration pathways in many perovskite oxides [168, 183, 184].

The energy profile of a migrating oxide ion was calculated by placing the ion at intermediate sites between adjacent oxygen vacancies along edges of a MO_6 octahedron. It was found that for $BaPrO_3$ and $BaThO_3$ the migration pathway was not a linear pathway, but curved away from the M site cation, with a deviation from linear of about 0.3Å and 0.27Å respectively. A schematic of oxide-ion migration in the perovskite structure is shown in Figure 4.8. This is a common trait among perovskites which was first predicted for $LaGaO_3$ using similar computational methods [183] and then observed experimentally using neutron diffraction and the maximum entropy method (MEM) as shown in Figure 4.9 [47]. Unusually, $BaZrO_3$ was found to have a linear oxygen vacancy migration pathway, which would be interesting to examine using a similar neutron diffraction analysis employed by Yashima et al.[47, 185].

The migration energy (E_{mig}) for these pathways (listed in Table 4.9 and shown for $BaZrO_3$ in Figure 4.10) show that $BaPrO_3$ has the highest value. It is important to note that these calculated migration energies (E_{mig}) relates to the intrinsic migration (or jump) of an oxygen vacancy, and does not include energies of defect

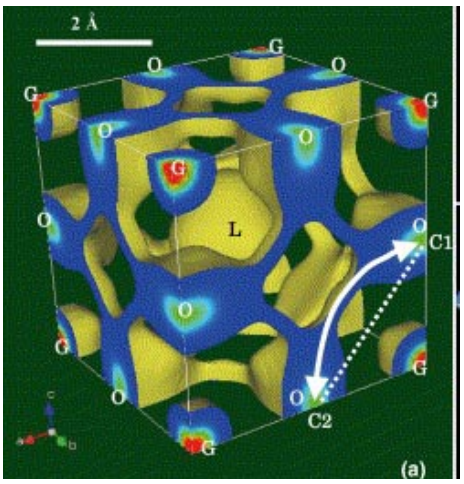

Figure 4.9: Equicontour surface of scattering amplitude (0.05 fm/Å^3) in cubic $(La_{0.8}Sr_{0.2})(Ga_{0.8}Mg_{0.15}Co_{0.05})O_{2.8}$ at 1665 K, with the scattering amplitude distribution on the (1 0 0) planes. The L, G and O denote the A-site cation ($La_{0.8}Sr_{0.2}$), the B-site cation ($Ga_{0.8}Mg_{0.15}Co_{0.05}$) and oxide ion, respectively, in the perovskite-type ABO_3 structure from [47]

Table 4.9: Oxygen vacancy migration energies for $BaZrO_3$ and $BaPrO_3$

Compound	Calc E_{mig} (eV)	Exp E_{mig} (eV)
$BaZrO_3$	0.65	0.71[a]
$BaPrO_3$	0.93	-
$BaThO_3$	0.58	-

[a][125]

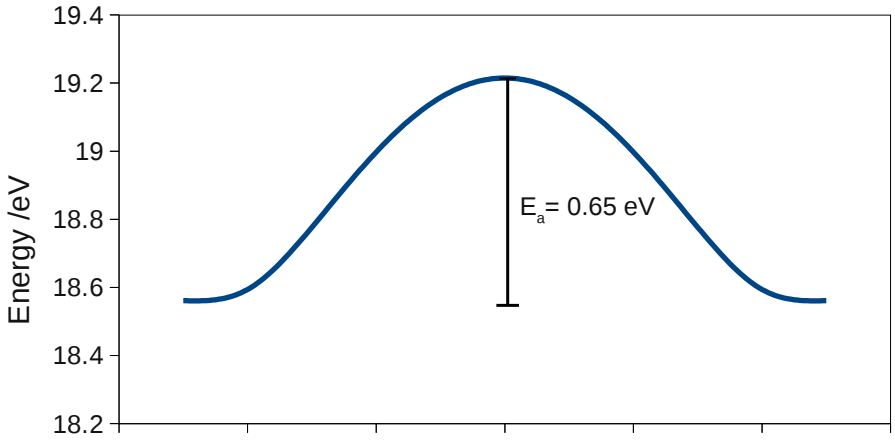

Figure 4.10: Energy profile of oxide-ion migration in $BaZrO_3$.

formation or association. As with fluorite-oxides, the bulk activation energy for oxygen ion conduction in perovskites will usually consist of the migration term (E_m) at high temperatures, but an additional binding term (E_{bind}) at low temperatures, leading to two slopes in the conductivity data. Hence, we recognise that direct comparison between our calculated migration energies and the experimental activation energies (E_a) is not straightforward. Also, the E_a values from experimental studies can show significant variation, which may reflect differences in synthesis conditions, phase purity or analysis of the conductivity data. Nevertheless, the calculated migration energy (0.65eV) for $BaZrO_3$ is consistent with the experimental activation energies ($\sim$0.7Å) for doped $BaZrO_3$ for high temperatures [125].

4.8 Chapter Summary

This study has provided atomic-scale insights on defect reactions and proton-dopant association in $BaZrO_3$, $BaPrO_3$ and $BaThO_3$ materials, which are relevant to their proton transport properties for intermediate temperature SOFC applications. The main points are summarised as follows:

(i) The high defect energies suggest that significant intrinsic disorder (either Frenkel, Schottky or reduction) in $BaZrO_3$ and $BaThO_3$ is unlikely, which is consistent with the relative chemical stability of these systems. In contrast, favourable redox energies are found for intrinsic reduction of $BaPrO_3$ (creating Pr^{3+} species), and oxidation of acceptor-doped $BaPrO_3$ (creating electronic holes). The latter result suggests p-type conductivity in doped $BaPrO_3$ in oxidising atmospheres, as observed experimentally.

(ii) The most favourable dopants were Yb, Y, Nd and Gd at the M site. This is in accord with experimental studies that commonly dope the $BaMO_3$ perovskites with Yb_2O_3, Y_2O_3, Nd_2O_3 and Gd_2O_3.

(iii) The water incorporation (hydration) energy is found to be less exothermic for $BaZrO_3$ than for $BaPrO_3$ and $BaThO_3$, but in all cases this suggests that the proton concentration would decrease with increasing temperature, in accord with the available thermodynamic data. The relaxed geometries suggest that the equilibrium O-H bond lies perpendicular to the line between two adjacent M ions. With a neighbouring acceptor-dopant ion, there is a small O-H displacement with local distortion from cubic symmetry for $BaZrO_3$.

(iv) Binding energies for dopant-OH pairs in $BaZrO_3$ indicate the weakest association for Gd and Y dopants, and the strongest association for Sc. These results confirm that local proton trapping and mobility would be very sensitive to the type of acceptor dopant ion. The Gd-doped $BaZrO_3$ system may require further experimental investigation. Our results are compatible with recent Neutron-Spin-Echo measurements of hydrated Y-doped $BaZrO_3$, which report data that are indicative of proton trapping. The high binding energies for all the dopant-OH pair clusters in $BaPrO_3$ and $BaThO_3$ suggest strong proton trapping effects, which would be detrimental to proton conductivity.

(v) Oxide ion migration is predicted to follow a curved path for $BaPrO_3$ and $BaThO_3$ (as observed for the $LaGaO_3$-based oxide-ion conductor), but a linear path for the $BaZrO_3$ system. This warrants further study by, for example, neutron diffraction and maximum entropy methods.

Chapter 5

Simulation Studies of the New Multiferroic Material $BiFeO_3$

5.1 Introduction

Multiferroics are materials that exhibit two or more properties from ferromagnetism, ferroelecticity and ferroelasticity [186–189]. Ferromagnetic materials allow the formation of domains of aligned electron spin (magnetic dipoles). These spin domains align when an external magnetic field is applied to the system. The ferromagnetic behaviour exists within a phase until the Curie temperature (T_C). Anti-ferromagnetic materials have neighbouring magnetic dipoles aligned in opposite directions and occurs below the Néel temperature (T_N). A ferroelectric phase, a term analogous to ferromagnetism, undergoes spontaneous alignment of the electric dipole moments caused by the interactions between them. This polarisation can be reversed by the application of an electric field, creating a hysteresis effect as seen in Figure 5.1. This hysteresis "memory" effect, that also exists in ferromagnetism, is the basis of the Ferromagnetic Random Access Memory (FeRAM) and Magnetic Random Access Memory (MRAM) applications.

Interest in multiferroics is high due to the often coupled nature of the two (or more) properties, also known as the magnetoelectric (ME) effect [186–189]. The result of this is a phase that enables the control of electric polarisation by a magnetic field. Coupled magnetic and ferroelectric order parameters can be exploited for developing magnetoelectronic devices including spin valves, that are used as modern hard disk head readers and magnetic sensors.

5.2 $BiFeO_3$: Materials and Defect Issues

Multiferroic materials are rare in nature because the conditions for being simultaneously ferroelectric and ferromagnetic are difficult to achieve [190]. There are a number of candidate materials for practical multiferroics, but the majority of these materials do not possess multiferroic properties at room temperature [191–193].

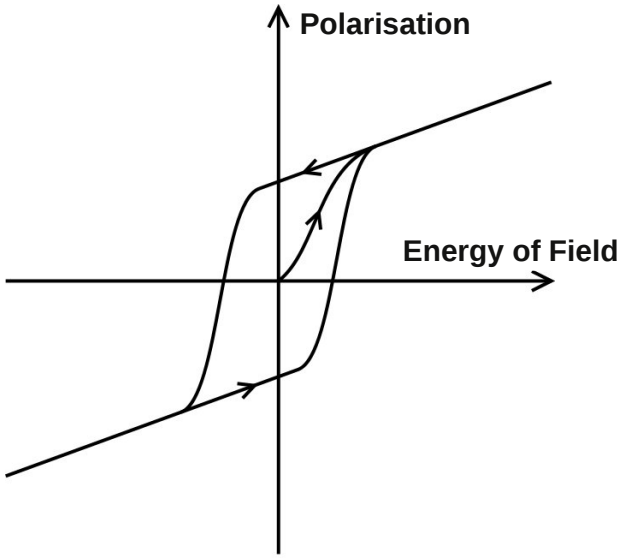

Figure 5.1: Simple hysteresis loop showing ferroelectric polarisation

The distorted perovskite oxide, $BiFeO_3$ (figure 5.2), has attracted considerable interest in the last few years[186–203]. It has multiferroic (antiferromagnetic and ferroelectric) properties below its Néel temperature of ∼650K [204, 205], making it an ideal material for use in device development. Its large electrical polarisation [206], the highest among all known ferroelectrics, makes $BiFeO_3$ a strong candidate for next-generation FeRAMs and promising for future MRAM elements [200].

Major drawbacks of $BiFeO_3$ as a multiferroic are the high leakage currents that limit its commercialisation into practical applications. Qi et al. [190] suggest the leakage currents are related to oxygen vacancies creating deep-trap energy levels in the band gap. The relationship with oxygen vacancies has been examined by doping with 2+ cations (with possible charge-compensation with oxygen vacancies) increasing current leakage, and doping with 4+ cations (with possible compensation with the filling of existing oxygen vacancies) decreasing current leakage[190, 201, 203]. The majority of current research on $BiFeO_3$ has been focused upon the multiferroic characteristics and attempts to limit the leakage currents. However, there has been limited research into the use of acceptor-doped $BiFeO_3$ as an oxide-ion conductor [202], utilising the oxygen vacancies that are related to current leakage. The work of

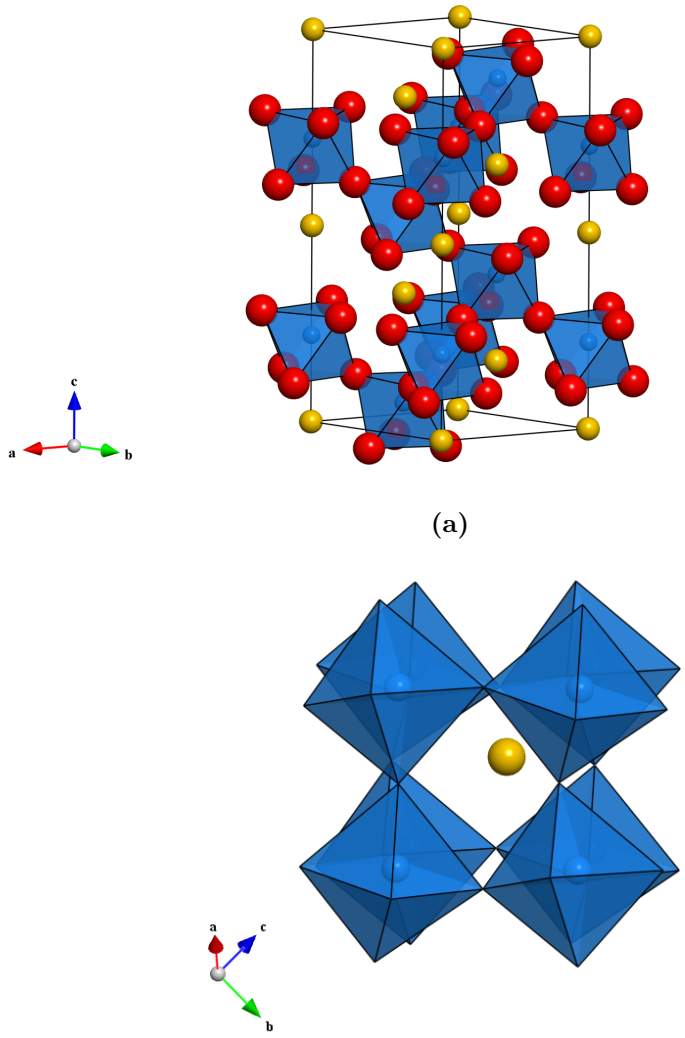

Figure 5.2: Distorted perovskite crystal structure of $BiFeO_3$ (a) Unit cell of $BiFeO_3$ (b) A-centred cell with FeO_6 corner sharing octahedra.

Brinkman et al. [202] showed oxide-ion conduction at 800°C raising the possibility of use a material in SOFCs.

However, there is considerable debate relating to the origin of the oxygen vacancies in $BiFeO_3$. There is some evidence of a small amount of oxygen non-stoichiometry, $BiFeO_{3-\delta}$ ($\delta < 0.01$), and a related 2% mol fraction of Fe^{2+} on the Fe^{3+} site, discussed by Li et al. [207] and Wang et al. [208]. Another possible source of oxygen vacancies is by acceptor-doping by 2+ cations, although the oxidation of Fe^{3+} to Fe^{4+} is another compensation mechanism for doping. Yang et al.[199] studying

Ca-doped $BiFeO_3$, stated that when the system is doped, vacancy formation is preferred to Fe oxidation and trapping of the vacancy also occurs. However, Chung et al. [209] reported that no evidence of Fe^{2+} was found in a Nb^{5+} doped sample of $BiFeO_3$. It is known that there are are a number of impurity phases that are formed during the synthesis process, indicating it is difficult to create a pure $BiFeO_3$ phase, which may help explain the difference between experimental results.

It is clear that the underlying defect chemistry of $BiFeO_3$ is very important as experiment shows that they underpin some of the key properties of the phase. However, it is often the case that accurate atomic-scale information is limited, such as lattice defects (oxygen vacancies), dopant solubility and oxygen migration energetics. In this chapter, we address a number of important topics concerning the multiferroic phase $BiFeO_3$, by applying for the first time atomistic simulation methods to this material. Emphasis here is placed on investigating the energetic and mechanistic features of intrinsic defects, redox characteristics, dopant site selectivity, oxide-ion migration and oxygen vacancy trapping in $BiFeO_3$ which are difficult to probe expermentally.

5.3 Crystal Structure and Potential Model

$BiFeO_3$ has a distorted perovskite type structure, as shown in Figure 5.2, in the trigonal space group R3c [210, 211]. The structure has the distinctive perovskite ion positions, linked corner-sharing FeO_6 octahedra with the A-site cation (Bi) in a 12-coordinate site. However, it is significantly distorted with tilting of the octahedra.

Our approach to modelling $BiFeO_3$ was to apply interatomic potentials used previously in studies of $Bi_4Ti_3O_{12}$ and Bi_2WO_6 listed in Table 5.1. The Fe-O potential was refined from the previously published potential by Minervini et al. [39]. To examine whether our model provided a good reproduction of the structure we ex-

Table 5.1: Interatomic potentials for $BiFeO_3$

(i) short-range

Interaction	A (eV)	ρ (Å)	C (eV Å^6)	Ref
$Bi^{3+} \cdots O^{2-}$	49529.35	0.2223	0.000	[101]
$Bi^{3+} \cdots Bi^{3+}$	24244.5	0.3284	0.000	[101]
$Fe^{3+} \cdots O^{2-}$	1414.6	0.3211	0.000	this study
$O^{2-} \cdots O^{2-}$	9547.96	0.2192	32.000	[103]

(ii) shell model

Species	$Y(e)$	k (eV Å↑-2)
Bi^{3+}	-5.51	359.55
O^{2-}	-2.04	6.3

amined the relaxed cell parameters and bond lengths, and compared them to the experimental structures determined by Moreau et al. [210] and by Kubel et al. [211]. Table 5.2 shows a comparison of calculated and experimental structures. In both cases our model reproduced the experimental cell parameters to within 0.5% accuracy and the bond lengths to within 0.05Å, which is not a trivial task. This successful reproduction of the complex distorted structure proves a valid potential model and allows reliable defect studies of $BiFeO_3$.

5.4 Intrinsic Defects

The energies of isolated intrinsic defects (interstitials and vacancies) in orthorhombic $BiFeO_3$ were first evaluated. Frenkel disorder and Schottky disorder energies were calculated by combining the individual defect energies and the lattice energies where appropriate. These defect reactions are given below (eqs 5.1-5.6) and the corresponding energies listed in Table 5.3.

Table 5.2: Calculated and experimental lattice parameters and bond lengths for $BiFeO_3$

Parameter	Calc.	Exp. [210]	δ^a	Exp. [211]	δ^a
a/Å	5.564	5.588	-0.024	5.579	-0.015
b/Å	5.564	5.588	-0.024	5.579	-0.015
c/Å	13.904	13.867	0.037	13.869	0.035
Bi-O/Å x3	2.281	2.313	-0.032	2.271	0.010
Bi-O/Å x3	2.466	2.523	-0.057	2.510	-0.044
Bi-O/Å x3	3.246	3.210	0.036	3.231	0.015
Bi-O/Å x3	3.440	3.405	0.035	3.449	-0.009
Fe-O/Å x3	1.992	1.942	0.050	1.958	0.034
Fe-O/Å x3	2.091	2.114	-0.023	2.110	-0.019

[a] Difference between calc. and expt.

O Frenkel disorder

$$\mathrm{O_O^{\times}} \rightarrow \mathrm{V_O^{\bullet\bullet}} + \mathrm{O_i''} \tag{5.1}$$

Bi Frenkel disorder

$$\mathrm{Bi_{Bi}^{\times}} \rightarrow \mathrm{V_{Bi}'''} + \mathrm{Bi_i^{\bullet\bullet\bullet}} \tag{5.2}$$

Fe Frenkel disorder

$$\mathrm{Fe_{Fe}^{\times}} \rightarrow \mathrm{V_{Fe}'''} + \mathrm{Fe_i^{\bullet\bullet\bullet}} \tag{5.3}$$

$BiFeO_3$ Schottky disorder

$$\mathrm{Bi_{Bi}^{\times}} + \mathrm{Fe_{Fe}}^{\times} + 3\,\mathrm{O_O^{\times}} \rightarrow \mathrm{V_{Bi}'''} + \mathrm{V_{Fe}'''} + 3\,\mathrm{V_O^{\bullet\bullet\bullet}} + \mathrm{BiFeO_3} \tag{5.4}$$

Bi_2O_3 partial Schottky disorder

$$2\,\mathrm{Bi_{Bi}^{\times}} + 3\,\mathrm{O_O^{\times}} \rightarrow 2\,\mathrm{V_{Bi}'''} + 3\,\mathrm{V_O^{\bullet\bullet}} + \mathrm{Bi_2O_3} \tag{5.5}$$

Fe_2O_3 partial Schottky disorder

$$2\,\mathrm{Fe_Y}^{\times} + 3\,\mathrm{O_O^{\times}} \rightarrow 2\,\mathrm{V_{Fe}'''} + 3\,\mathrm{V_O^{\bullet\bullet}} + \mathrm{Fe_2O_3} \tag{5.6}$$

where, in Kröger-Vink notation [212], $V_O^{\bullet\bullet}$, $V_{Bi}^{\prime\prime\prime}$, and $V_{Fe}^{\prime\prime\prime}$ represent oxygen, bismuth, and iron vacancies, respectively, $O_i^{\prime\prime}$, $Bi_i^{\bullet\bullet}$, and $Fe_i^{\bullet\bullet}$ represent oxygen, bismuth, and iron interstitials, respectively, and the superscripts $^{\bullet}$ (positive), $^{\prime}$ (negative), and $^{\times}$ (neutral) indicate the charge of the defect relative to the normal site.

Table 5.3: Energies of Frenkel and Schottky disorder in $BiFeO_3$

Type	Eqn.	Defect Energy (eV/defect)
O Frenkel	5.1	4.26
Bi Frenkel	5.2	12.55
Fe Frenkel	5.3	NC[a]
Schottky	5.4	4.98
Bi_2O_3 Schottky-type	5.5	4.51
Fe_2O_3 Schottky-type	5.6	6.25

[a]non-convergence of calculation (Fe interstitial defect)

Examination of Table 5.3 reveals that the creation of Frenkel and Schottky defects is associated with substantial amounts of energy. In particular, the simulations confirm that the perovskite structure is higly unlikely to accomodate Bi interstitials (as would be expected in a close-packed perovskite structure). The most favourable intrinsic disorder is for the formation of O interstitials. However, the magnitude of the energies suggests that the concentration of intrinsic atomic defects is relatively small. These results are consistent with previous studies of the perovskite system [213, 214] where Schottky and Frenkel defects are not common.

The potential applications of this material within SOFCs would require it to be used under highly reducing and oxidising conditions. As mentioned earlier, there is discussion on the existence and role of varying Fe oxidation states within $BiFeO_3$. Wang et al. [208] and Li et al. [207] both maintain the existence of Fe^{2+} in undoped $BiFeO_3$ due to oxygen non-stoichiometry. However, Chung et al. [209] did not find any evidence of Fe^{2+} within pure, Mn and Nb-doped samples. In addition, Kharel et al. [201] concluded that doping had little effect on Fe valence states. It has also been suggested by Li et al. [207] that cation vacancies are possibly compensated

by the oxidation of Fe^{3+} to Fe^{4+}.

Therefore, it is important to determine the redox stability of this phase. This is probed using the series of calculations that were used for $BaMO_3$ in chapter 4, and have been successfully applied to other transition metal perovskite oxides [46, 168]. In these calculations the electronic defects ($h^{\bullet}$ and e') are modelled as localised species (small polarons). The holes ($h^{\bullet}$) were assumed to reside on either the iron ion ($Fe^{3+} \rightarrow Fe^{4+}$) or oxygen ion ($O^{2-} \rightarrow O^{-}$) and electrons reside on the iron ion ($Fe^{3+} \rightarrow Fe^{2+}$). The following redox reactions were considered:

(i) Oxidation to give a metal deficient material:

$$\frac{1}{2}O_2(g) + \frac{2}{3}Fe_{Fe}^{\times} \rightarrow \frac{2}{3}V_{Fe}''' + 2h^{\bullet} + \frac{1}{3}Fe_2O_3 \tag{5.7}$$

$$\frac{1}{2}O_2(g) + \frac{2}{3}Bi_{Bi}^{\times} \rightarrow \frac{2}{3}V_{Bi}''' + 2h^{\bullet} + \frac{1}{3}Bi_2O_3 \tag{5.8}$$

The calculations find that the O^{-} hole species is more favourable than that of Fe^{4+} by 5 eV. This suggests that the holes prefer to be centred on oxygen sites, although we recognise that there will be some degree of Fe(3d)-O(2p) mixing [215–218].

(ii) Reduction to give an oxygen deficient material:

$$O_O^{\times} \rightarrow V_O^{\bullet\bullet} + \frac{1}{2}O_2(g) + 2e' \tag{5.9}$$

(iii) Disproportionation of Fe^{3+}:

$$2Fe_{Fe}^{\times} \rightarrow Fe_{Fe}^{\bullet} + Fe_{Fe}' \tag{5.10}$$

(iv) In addition, M^{2+} doping onto either of the cation lattice sites within this system would create oxygen vacancies. Under high oxygen partial pressures these

vacancies can be filled with the creation of a hole species via the following reaction:

$$\frac{1}{2}O_2 + V_O^{\bullet\bullet} \rightarrow O_O^{\times} + 2h^{\bullet} \tag{5.11}$$

The energies of the various redox processes (eqns 5.7-5.11) are summarized in Table 5.4, and were calculated using the appropriate free ion terms together with the point defect energies. The results suggest that $BiFeO_3$ is more readily reduced than oxidised, with the creation of oxygen vacancies and Fe^{2+} species via reaction (5.9). The highly unfavourable energy (> 4 eV) estimated for disproportionation of Fe^{3+} (to Fe^{2+} and Fe^{4+}) suggests that tetravalent iron ions are unlikely to form in this material through this process. The key significance of these results is the likely intrinsic formation of oxygen vacancies via reduction without the need for acceptor doping which is in agreement with experimental observations [207, 208]. The oxygen vacancies are believed to be the source of leakage currents and are also required for oxide-ion conduction.

Table 5.4: Calculated energies of redox reaction in $BiFeO_3$

Redox process	Equation	Energy (eV/electronic defect)[a]
Oxidation	5.7	7.71
Oxidation	5.8	6.26
Reduction	5.9	1.42
Disproportionation	5.10	4.54
Oxidation (doped oxide)	5.11	2.50

[a]Calculated using $\Delta E = 9.87$ eV for $\frac{1}{2}O_2 \rightarrow O^{2-}$; O hole ($h^{\bullet}$) = 8.17 eV ;Fe hole ($h^{\bullet}$) term = 13.32 eV; Fe electron (e') term = -4.24 eV

5.5 Dopant Incorporation

As discussed in chapter 4, doping in perovskites is a common practice to enhance specific properties and has been highly successful in optimising oxide-ion conduc-

tivity in a variety of perovksites. In terms of modes of "solution" into the $BiFeO_3$ material, dopant ions can substitute at either Bi^{3+} or Fe^{3+} sites with the creation of charge-compensating defects. This raises key questions in relation to the favoured substitution site, the type of compensating defect and the inuence, if any, of A and B site cation size. There is a considerable amount of interest in the doping of the $BiFeO_3$ phase, centred mainly on the effects of doping upon current leakage which is thought to be related to the oxygen vacancy concentration [190, 199, 203, 209].

Our simulation methods can probe these issues by generating quantitative estimates of the relative energies of different modes of solution. As noted, such an approach has been applied successfully to a variety of oxides. We have therefore examined a wide range of dopants in $BiFeO_3$ including divalent (e.g. Co^{2+}, Ni^{2+}, Sr^{2+}), trivalent (e.g. Mn^{3+}, Yb^{3+}, La^{3+}), tetravalent (e.g. Ti^{4+}) and pentavalent (e.g. Nb^{5+}, Ta^{5+}) ions, which is a wider range than current experimental reports. The results are discussed in the following sub-sections.

5.5.1 M^{2+} Substitution

Experimental research has shown that acceptor-doping leads to creation of oxygen vacancies and a measured increase in leakage currents [190]. This doping mechanism can be represented by the following defect reactions for the Bi and Fe sites respectively:

$$MO + Bi_{Bi}^{\times} + \frac{1}{2}O_O^{\times} \rightarrow M'_{Bi} + \frac{1}{2}V_O^{\cdot\cdot} + \frac{1}{2}Bi_2O_3 \tag{5.12}$$

$$MO + Fe_{Fe}^{\times} + \frac{1}{2}O_O^{\times} \rightarrow M'_{Fe} + \frac{1}{2}V_O^{\cdot\cdot} + \frac{1}{2}Fe_2O_3 \tag{5.13}$$

The energies of incorporation (or "solution") are listed in Table 5.5 and plotted as a function of dopant ionic radius in Figure 5.3. We note that the dopant radii for six-coordination from Shannon[173] are used since 12-coordination values are not available for all the ions.

Table 5.5: Calculated solution energies for M^{2+} dopants in $BiFeO_3$

Dopant	Ionic Radii /Å	Bi-site	Fe-site
Co^{2+}	0.65	5.22	3.48
Mn^{2+}	0.67	4.58	3.63
Ni^{2+}	0.69	5.46	3.49
Mg^{2+}	0.72	5.37	3.50
Ca^{2+}	1.00	3.75	4.62
Sr^{2+}	1.18	3.56	6.20

Examination of Table 5.5 and Figure 5.3 reveals two main points. First, low favourable solution energies were found for the smaller ions, Co, Mn, and Ni, at the Fe-site and the larger ions, Ca and Sr, at the Bi-site. These results suggest a degree of ion size correlation, where lower solution energies are observed when the host site ionic radius is similar to that of the dopant ion radius. In the case of $BiFeO_3$, Fe^{3+} has an ionic radius of 0.55Å with Co, Mn, and Mg having an ionic radii of 0.65Å, 0.67Å, 0.69Å, and 0.72Å respectively. In contrast, Bi^{3+} has a larger ionic radius of 1.03Å and the ions favourable to substitute onto this site, Ca and Sr, have ionic radii of 1.00Å and 1.18Å respectively. Our results compare favourably with experimental observations, in which Ca and Sr are known to favour substitution onto the Bi site [202] and Co, Mn, and Ni have been shown by Naganuma et al. [219] to favour the Fe-site. These results add support to the validity of our simulation approach. The leakage currents of Ni^{2+} and Ti^{4+} doped $BiFeO_3$ are found to increase and decrease respectively [190].

5.5.2 M^{3+} Substitution

The addition of isovalent M^{3+} does not require charge-compensation and is not expected to influence the concentration of defects; M^{3+} can be represented by equations 5.14 and 5.15 for Bi and Fe substitution repectively.

$$\frac{1}{2}M_2O_3 + Bi_{Bi}^{\times} \rightarrow M_{Bi}^{\times} + \frac{1}{2}Bi_2O_3 \tag{5.14}$$

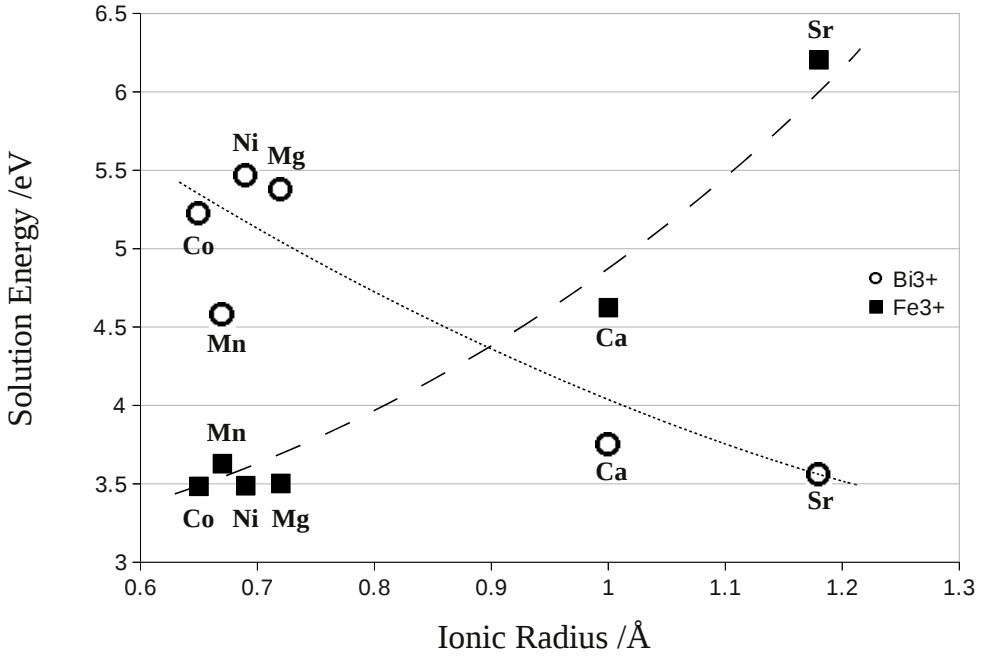

Figure 5.3: Solution energy vs. dopant ionic radius for M^{2+} dopants in $BiFeO_3$. Lines are guide to the eye only.

$$\frac{1}{2}M_2O_3 + Fe_{Fe}^{\times} \rightarrow M_{Fe}^{\times} + \frac{1}{2}Fe_2O_3 \tag{5.15}$$

The calculated solution energies for a number of trivalent dopants are shown in Table 5.6 and Figure 5.4. The results show again a clear trend that ion-size is a key factor in a similar way to that of the M^{2+} dopants. We predict that the smaller ions, Mn, Ga, and Yb are more soluble on the Fe-site, while the larger dopants of Nd and La subsitute preferentially at the Bi-site. Our calculations are in accord with doping studies [220–222] that attempted to suppress bismuth loss at deposition by doping, and found Nd and La subsituting onto the Bi-site. Also, Mn^{3+} has been found experimentally to favour the Fe-site [223] as predicted in our results. Our results also show a "crossover" point at Gd, making it difficult to make predictions about this dopant, which suggests possible substitution at either the Bi or Fe sites; this effect warrants further investigation.

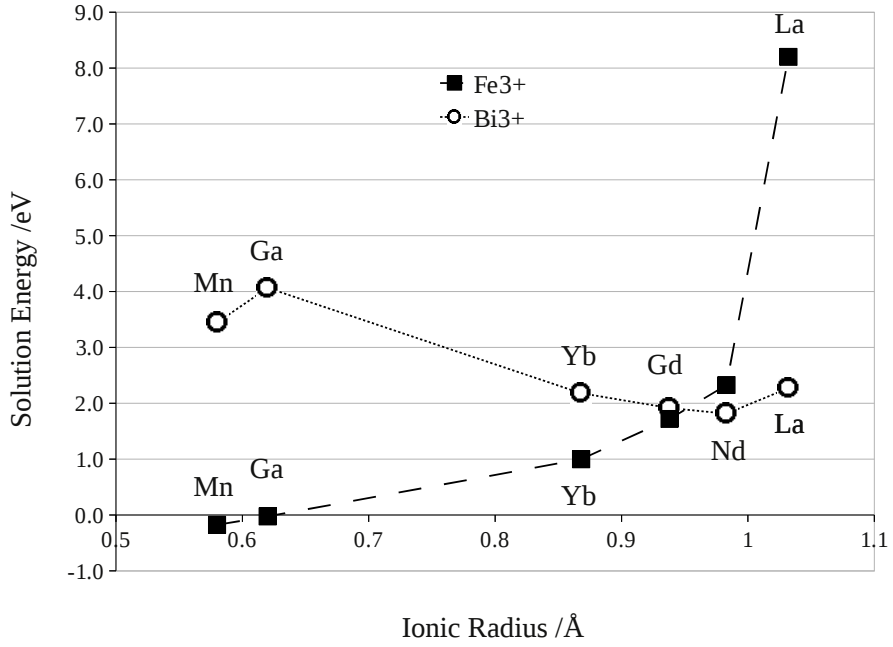

Figure 5.4: Solution energy vs. dopant ionic radius for M^{3+} dopants in $BiFeO_3$. Lines are guide to the eye only.

Table 5.6: Calculated solution energies for M^{3+} dopants in $BiFeO_3$

Dopant	Ionic Radii /Å	Bi-site	Fe-site
Mn^{3+}	0.58	3.45	-0.18
Ga^{3+}	0.62	4.07	-0.02
Yb^{3+}	0.87	2.18	1.00
Gd^{3+}	0.94	1.92	1.72
Nd^{3+}	0.98	1.81	2.33
La^{3+}	1.03	2.27	8.20

5.5.3 M^{4+} and M^{5+} Substitution

The introduction of M^{4+} and M^{5+} dopants on either the Bi or Fe site produces three possible charge-compensation mechanisms; these are shown as follows using the Fe site:

(i) Cation vacancy formation

M^{4+}:

$$MO_2 + \frac{4}{3}Fe_{Fe}^{\times} \rightarrow M_{Fe}^{\bullet} + \frac{1}{3}V_{Fe}^{'''} + \frac{2}{3}Fe_2O_3 \tag{5.16}$$

M^{5+}:

$$\frac{1}{2}M_2O_5 + \frac{5}{3}Fe_{Fe}^{\times} \rightarrow M_{Fe}^{\bullet\bullet} + \frac{2}{3}V_{Fe}^{\prime\prime\prime} + \frac{5}{6}Fe_2O_3 \tag{5.17}$$

(ii) Formation of electronic species (as $Fe_{Fe}^{\prime}$)

M^{4+}:

$$MO_2 + Fe_{Fe}^{\times} \rightarrow M_{Fe}^{\bullet} + e^{\prime} + \frac{1}{4}O_2 + \frac{1}{2}Fe_2O_3 \tag{5.18}$$

M^{5+}:

$$\frac{1}{2}M_2O_5 + Fe_{Fe}^{\times} \rightarrow M_{Fe}^{\bullet\bullet} + 2e^{\prime} + \frac{1}{2}O_2 + \frac{1}{2}Fe_2O_3 \tag{5.19}$$

(iii) Filling of existing oxygen vacancies from non-stoichiometry

M^{4+}:

$$MO_2 + \frac{1}{2}V_O^{\bullet\bullet} + Fe_{Fe}^{\times} \rightarrow M_{Fe}^{\bullet} + \frac{1}{2}O_O^{\times} + \frac{1}{2}Fe_2O_3 \tag{5.20}$$

M^{5+}:

$$\frac{1}{2}M_2O_5 + V_O^{\bullet\bullet} + Fe_{Fe}^{\times} \rightarrow M_{Fe}^{\bullet} + O_O^{\times} + \frac{1}{2}Fe_2O_3 \tag{5.21}$$

The calculated energies for Ti^{4+}, Nb^{5+} and Ta^{5+} dopants are listed in Table 5.7. Our calculations predict that for this compound, charge-compensation by the creation of cation vacancies is unfavourable with the majority of the solution energies above 3.5 eV.

Examination of Table 5.7 reveals three further points. Firstly, all of the M^{4+} and M^{5+} dopants show a preference for the Fe-site, regardless of compensation mechanism. The low solution energies at this site suggest that the dopant ions are readily taken up by the $BiFeO_3$ structure. This agrees with experimental studies of Ti [190], Nb [209], and Ta-doped [203] phases that identified dopant substitution onto the Fe-site.

Secondly, we find that the most favourable compensation mechanism is the elimi-

Table 5.7: Calculated solution energies of 4+ and 5+ dopants in $BiFeO_3$

	Solution Energy (eV)		
Dopant	Cation Vacancy	Electronic	O Vacancy Elimination
Bi-site			
Ti^{4+}	NC[a]	NC[a]	NC[a]
Nb^{5+}	7.02	2.35	-0.49
Ta^{5+}	7.03	2.36	-0.48
Fe-site			
Ti^{4+}	2.74	-1.05	-2.47
Nb^{5+}	6.74	-0.83	-3.67
Ta^{5+}	6.34	-1.23	-4.07

[a]NC ≡ Non-convergence of calculation

nation of existing oxygen vacancies. This predicts that the incorporation of these dopants would decrease the concentration of oxygen vacancies in non-stoichiometric $BiFeO_3$ and hence cause a reduction in current leakage. This effect has been observed by Qi et al. [190] who reported a decrease of current leakage by three orders of magnitude when doping with Ti^{4+} using current density - electric field (J-E) strength measurements. Jun et al. [203] reported Ta^{5+} substitution for Fe^{3+} reduced the leakage current by six orders of magnitude. Chung et al. [209], also observed a reduction of oxygen vacancies when doping with Nb^{5+}. It is clear that further study of doping with M^{4+} and M^{5+} ions and the effect of limiting current leakages is needed for the developement of $BiFeO_3$ as a practical multiferroic. There is a further range of higher valent dopants that could be considered such as Zr^{4+}, Sn^{4+} and W^{6+}, which warrants future study.

5.6 Oxide-Ion Migration

The $BiFeO_3$ phase has been examined as a fast oxide ion conductor for potential use in oxygen permeation membranes by Brinkman et al. [202]. It was reported that an Sr-doped sample of $BiFeO_3$ exhibited a significant oxygen flux at 800°C with

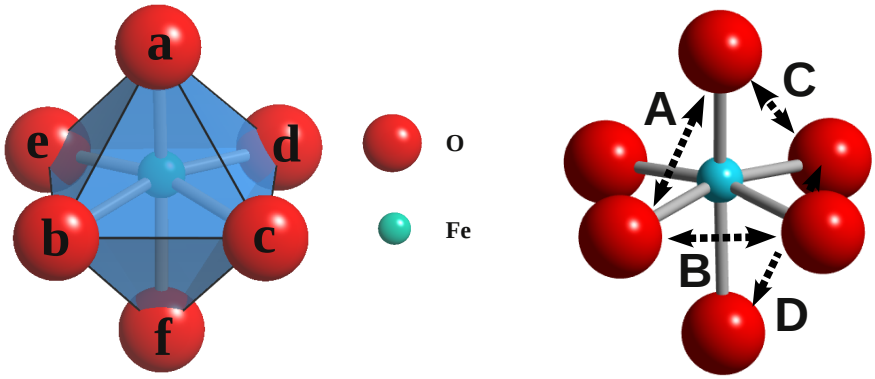

(a) (b)

Figure 5.5: (a) FeO_6 octahedra with oxygen labels for identification of oxygen migration paths, (b) Examples of each path around an FeO_6 octahedron, A = a-b, c-d, e-f. B = b-c, b-f, c-f. C = a-d, a-e, e-d. D = b-e, a-c, d-f.

an activation energy of 47 to 61 $kJmol^{-1}$, depending on the membrane thickness. Furthermore, Yang et al. [199] have shown that in Ca-doped $BiFeO_3$ the oxygen vacancies respond to an electric field with migration towards the negatively charged electrode. In the same study oxygen diffusion was estimated to be $\sim 10^{-17} cm^2 s^{-1}$, which would make this system a poor oxide ion conductor. However, the precise paths for oxide-ion migration have not been fully identified.

The tilting of the Fe-O octahedra in the distorted perovskite structure of $BiFeO_3$ means that all vacancy migration paths were investigated. It was found that there are four possible migration paths between adjacent oxygen ions in the structure, which are shown in Figure 5.5. As with the $BaMO_3$ perovskites (chapter 4), the energy profiles for oxide ion migration were mapped out by calculating the defect energy of the migrating ion at intermediate sites between adjacent oxygen vacancies. The difference in energy between the highest energy position ("saddle-point") and the lowest were then calculated giving estimates of E_{mig} for oxide ion transport along the different migration pathways. Our simulations show the importance of local lattice relaxation effects and that the saddlepoint cannot be treated purely as a structural gap of hard-sphere ions.

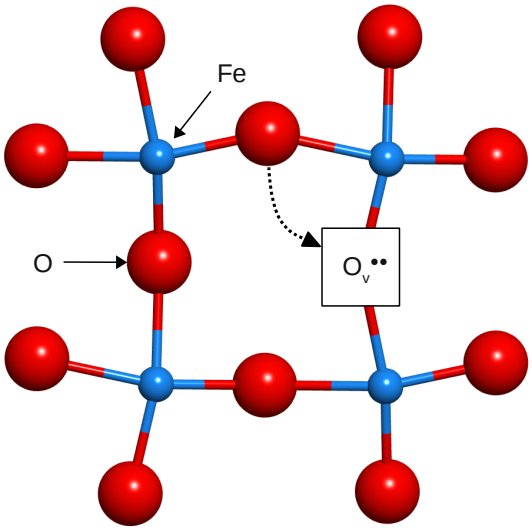

Figure 5.6: Schematic representation of the curved path of oxygen migration path in $BiFeO_3$

Table 5.8: Energetics of oxygen migration paths in $BiFeO_3$ shown in Figure 5.5

Path	Linear E_{mig} /eV	Curved E_{mig} /eV
A	1.27	0.47
B	1.33	0.93
C	2.10	1.29
D	1.66	1.51

It was found that the lowest energy pathways are curved away from a linear migration path, as shown in Figure 5.6. This behaviour has been found in other perovskite-related structures such as the $LaGaO_3$-based oxide ion conductor LSGM [104, 224], and was confirmed by neutron scattering and diffraction studies[47, 225] of pure and doped $LaGaO_3$. The results of both the linear pathways and the lowest energy paths are listed in Table 5.8.

Table 5.8 indicates that migration via paths A and B are the most energetically favourable. The E_{mig} of path A (0.47 eV) suggests oxide-ion conduction is possible in $BiFeO_3$. Also, our result for this path is in good agreement with the experimental

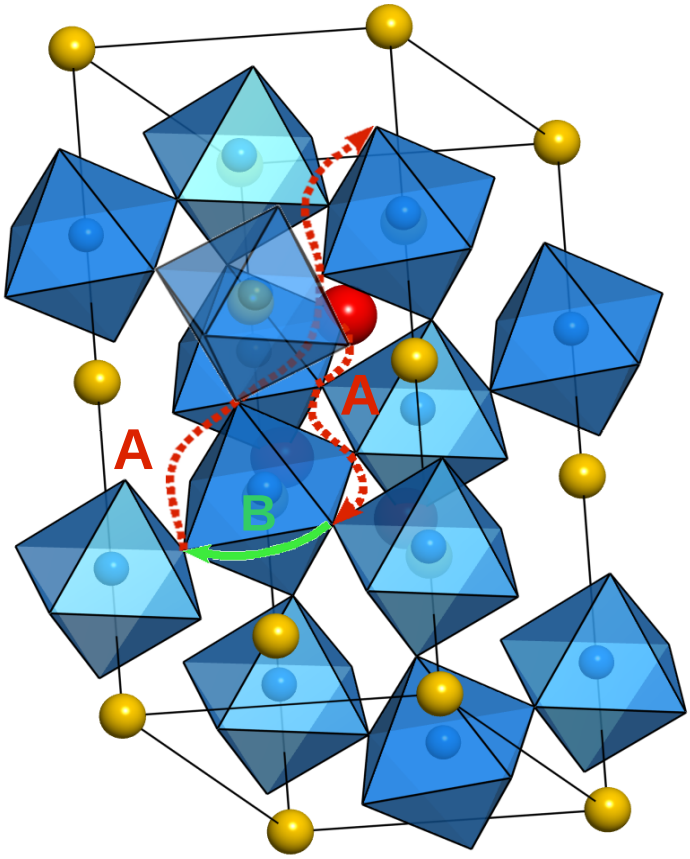

Figure 5.7: Schematic of oxygen vacancy migration paths A and B in $BiFeO_3$, in the Fe-O layer

activation energy of 47 to 61 kJmol^{-1} (0.49 to 0.63 eV) [202]. When considering the long-range migration of oxide-ions within this phase, Figure 5.7 shows the lowest energy path forms 1D-like channels. However the next most favourable path, B ($E_{mig} = 0.93$ eV), would allow migration between two channels of path A as detailed in Figure 5.7(c). This would suggest fully isotropic migration would require the higher activation energy of path B, which we predict to be 0.93 eV. The long-range migration of oxygen vacancies has been shown in Ca-doped $BiFeO_3$ with an electric field used to "sweep" oxygen vacancies to one side of the material [199].

5.7 Defect Trapping

As discussed previously, the oxygen vacancies that are formed due to non-stoichiometry and acceptor-doping are key to the physical properties exhibited by $BiFeO_3$. However, the properties that are required for fast oxide-ion conduction are related to the unwanted high leakage currents. The understanding of the trapping of oxygen vacancies by subvalent dopants is critical to the optimisation for the relevant usage as either a multiferroic or an oxide-ion conductor. It is known that interactions between dopant ions and their charge compensating defects (oxide-ion vacancies) can lead to the formation of distinct clusters. A schematic of dopant-vacancy interaction is shown in Figure 5.8.

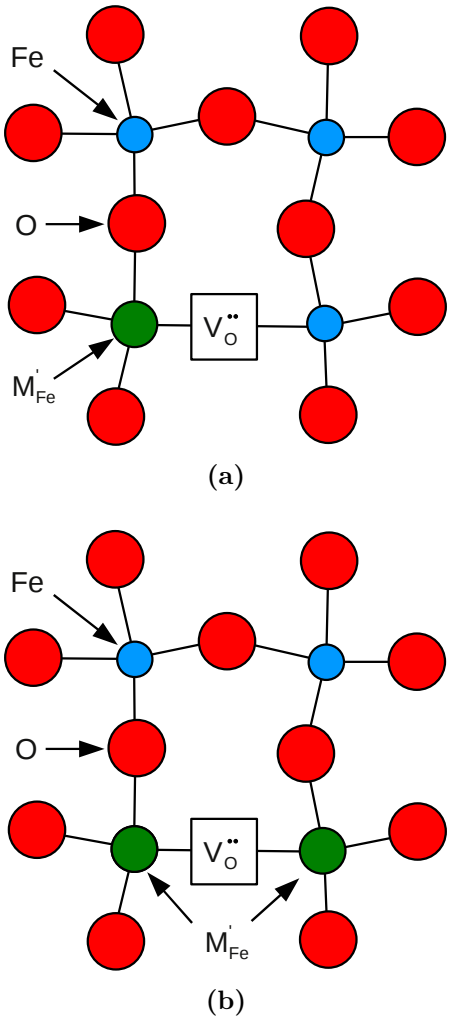

Figure 5.8: Schematic of dopant-vacancy binding in $BiFeO_3$, Fe-O layer shown (a) $M_{Fe}{}'V_O^{\bullet\bullet}$ (b) $M_{Fe}{}'V_O^{\bullet\bullet}M_{Fe}{}'$

A series of calculations on defect clusters in $BiFeO_3$ was carried out to investigate interactions between oxygen vacancies and dopant cations, which are not fully understood in this material.

Defect clusters were calculated for the pair ($M_{Bi}'V_O^{\bullet\bullet}$) and neutral trimer ($M_{Bi}'V_O^{\bullet\bullet}M_{Bi}'$) clusters, where M is a divalent dopant (eg. Ca, Sr). As in section 4.6, binding energies were then calculated as the difference between the energy of the cluster and the sum of the isolated component defects using equation 4.14. For example the binding energy for the pair cluster of ($Sr_{Bi}'V_O^{\bullet\bullet}$) is derived as follows:

$$E_{\text{bind}} = E(Sr_{Bi}'V_O{}^{\bullet\bullet}) - [E(Sr_{Bi}') + E(V_O{}^{\bullet\bullet})] \tag{5.22}$$

A negative value would indicate that the cluster is stable with respect to the isolated defects. Here we focused on the dopants and host sites that were indicated as most favourable from our results in section 5.5 i.e., Ca, Sr on Bi, and Co, Mn, Ni, Mg on Fe. The calculated binding energies are presented in Table 5.9.

The results in Table 5.9 reveal a strong degree of association for the M^{2+} dopant pair- and trimer-clusters, with energies ranging from -0.62 to -1.09 eV. The results also suggest that the Fe site has a stronger tendency to "trap" an oxygen vacancy. The smallest binding energies are calculated for Ca^{2+} and Sr^{2+} substituted on the Bi site meaning doping with these ions would have the least impact upon oxide-ion mobility. However, the magnitude of the association would suggest that an increase in the conduction activation energy would occur with increasing dopant concentration. It must be noted that the majority of research into $BiFeO_3$ has focussed upon its multiferroic properties and little attention has been paid to its potential as an oxide-ion conductor. Therefore, before an assessment can be made as to its suitability as an oxide-ion conductor, further research into oxide-ion conductivity across a wide range of dopant concentrations in $BiFeO_3$ is required, with specific focus on Ca- and Sr-doping.

Table 5.9: Calculated binding energies for M^{2+} dopant-pair clusters and M^{2+} neutral trimer clusters in $BiFeO_3$ (a) the Bi site and (b) Fe site

(a) M^{2+} on Bi Site

	binding energy /eV per defect	
dopant	$(M_{Bi}{}'V_O^{\bullet\bullet})$	$(M_{Bi}{}'V_O^{\bullet\bullet}M_{Bi}{}')$
Ca	-0.65	-0.59
Sr	-0.62	-0.58

(b) M^{2+} on Fe Site

	binding energy /eV per defect	
dopant	$(M_{Fe}{}'V_O^{\bullet\bullet})$	$(M_{Fe}{}'V_O^{\bullet\bullet}M_{Fe}{}')$
Co	-0.99	-1.07
Mn	-0.97	-1.08
Ni	-1.01	-1.09
Mg	-0.97	-1.05

5.8 Chapter Summary

Atomistic simulation techniques have been used, for the first time, to study the properties of $BiFeO_3$, which have potential oxide-ion conducting and multiferroic device applications. The following main points can be taken from this study.

(i) A potential model for $BiFeO_3$ has been successfully developed and reproduction of the crystal structure is accurate. The energetics of intrinsic atomic defects suggest that Frenkel and Schottky type defects are unlikely. The reduction process involving the formation of oxygen vacancies and Fe^{2+} is the most favourable. This may explain the oxygen sub-stoichiometry of this compound that has been observed experimentally. Disproportionation of Fe^{3+} (to Fe^{2+} and Fe^{4+}) is highly unfavourable. These results indicate that deviations from oxygen stoichiometry is likely to play a crucial role on the multiferroic properties of $BiFeO_3$ and the levels will depend on the synthesis conditions.

(ii) Our calculations show that 2+ and 3+ cation doping is largely influenced by ion size effects with smaller dopants (e.g. Mg^{2+}, Ga^{3+}) favouring the Fe-site and larger dopants (e.g. Sr^{2+}, Nd^{3+}) the Bi-site, in agreement with experimental observations. The Gd^{3+} dopant is found to sit at a "crossover" point in our solution energies for Bi versus Fe substitution. This suggests possible "ambi-site" behaviour in which the dopant can occupy either site.

(iii) The higher valent cations (e.g. Ti^{4+}, Nb^{5+}) are predicted to substitute preferentially for the Fe-site and charge-compensated by the filling of oxygen vacancies. This has been suggested as an explanation for observed reduction in current leakage.

(iv) The activation energy for oxygen vacancy migration has been calculated to be 0.47 eV, in good agreement with experimental data, suggesting possible oxide-ion conduction in $BiFeO_3$. The pathway for oxygen vacancy migration is predicted to be a curved trajectory between oxygen sites, with anisotropic long range conduction within the distorted perovskite structure.

(v) The calculations on dopant-oxygen vacancy clusters indicate that Ca and Sr doped on the Bi site give the smallest association energies and doping on the Fe site is likely to "trap" oxygen vacancies. However, the magnitude of all association energies suggest that increasing dopant concentration may have a detrimental effect upon oxide-ion migration within $BiFeO_3$.

Chapter 6

Conclusions and Further Work

6.1 General Remarks

In this thesis we have presented how the application of computer modelling techniques to a range of fluorite and perovskite related materials can give valuable insights into defect and transport properties. By examining these atomic scale phenomena we have attempted to further understand experimental observations and macroscopic properties that could not be analysed easily by conventional methods. Furthermore, we have strived to make our simulation work predictive to facilitate the development of advanced materials for potential applications in a range of electrochemical devices. It is appropriate to conclude this thesis by reviewing our findings and by suggesting extensions to each study.

6.2 Structural and Defect Properties of Doped Bismuth Oxide

In chapter 3 we studied the structural, defect, and dopant properties of the δ-Bi_2O_3 related phase Bi_3YO_6. The ordering of the intrinsic oxygen vacancies were investigated with both short and long-range ordering considered. For a single unit cell three ordering schemes are possible. Our results showed that the least favourable ordering was $\langle 111 \rangle$ and the most favourable the $\langle 110 \rangle$, which is in agreement with total neutron scattering data [92]. The lowest energy vacancy configuration identified thus far for Bi_3YO_6 is a 2 x 2 x 2 supercell containing a combination of $\langle 111 \rangle$ and $\langle 110 \rangle$ vacancy configurations, previously found to be the lowest energy configuration for pure δ-Bi_2O_3 by DFT techniques [98].

An investigation into the intrinsic defect energies of Bi_3YO_6 was undertaken. The most favourable interstitial site for oxide ions was found to be on the intrinsic vacancy sites (ca. $\frac{1}{4}$, $\frac{1}{4}$, $\frac{1}{4}$); making the structure similar to that of Bi_3NbO_7. The isolated point defects were combined and it was found that the formation of Schottky and cation Frenkel defects is energetically unfavourable in the Bi_3YO_6 phase.

The oxygen Frenkel energy was found to be favourable (0.54 eV) and indicated a highly mobile oxygen sub-lattice.

The energetics of solution of alkaline-earth, transition metal, and lanthanide ions in Bi_3YO_6 have been studied. The incorporation of subvalent ions will enhance the oxide-ion conduction due to an increase in the concentration of the charge-compensating oxygen vacancies. The most energetically favoured dopants were predicted to be Nd^{3+}, La^{3+} and Pb^{2+}. Doping with Pb^{2+} is the most interesting result as this would create a higher oxygen vacancy concentration than in pure δ-Bi_2O_3, but also preserve the polarisable nature of the cation sublattice, that is thought to influence oxide ion migration.

With respect to further work, the application of molecular dynamics (MD) is the next step in the study of Bi_3YO_6. This would allow the investigation of temperature related phenomena such as the experimentally observed non-linear thermal expansion of the cell parameters and the relationship of the population of the 48i site with temperature. Another application of MD to the Bi_3YO_6 phase would be the examination of the oxide-ion migration pathways.

A new Re^{7+} doped Bi_2O_3 phase, $Bi_{28}Re_2O_{49}$, has been synthesised and characterised by Greaves et al [114]. Our preliminary study has not produced a satisfactory potential model. This is largely due to the complexity of the structure in which the local Re coordinations are not fully characterised and to the high valence state of Re.

Future work should include further characterisation of the crystal structure and DFT-based structural optimisations.

6.3 Defect Chemistry and Proton-Dopant Association in $BaZrO_3$, $BaPrO_3$ and $BaThO_3$

In chapter 4 the atomic-scale properties of the proton conducting $BaZrO_3$, $BaPrO_3$ and $BaThO_3$ materials have been probed. The effects of defects, water incorporation and proton-dopant association were the focus of this study.

The intrinsic disorder and redox characteristics of the three perovskites have been investigated and it was found that for $BaZrO_3$ and $BaThO_3$ intrinsic disorder (either Frenkel, Schottky or reduction) is unlikely. This is in agreement with the observed chemical stability of these phases. In contrast, favourable redox energies are found for intrinsic reduction of $BaPrO_3$ (creating Pr^{3+} species), and oxidation of acceptor-doped $BaPrO_3$ (creating electronic holes). The latter result suggests p-type conductivity in doped $BaPrO_3$ in oxidising atmospheres, as observed experimentally [151, 158].

The incorporation of a range of dopants were investigated and our results suggested that the most favourable dopants were Yb, Y, Nd and Gd. This is in accord with experimental studies that commonly dope the $BaMO_3$ perovskites with Yb_2O_3, Y_2O_3, Nd_2O_3 and Gd_2O_3. Furthermore, our results suggested that substituting trivalent cations onto the M site is more favourable than onto the Ba site.

We also probed the energetics of water incorporation as the mechanism for introducing protons into the crystal structure, which is required for proton conduction. The water incorporation (or hydration energy) is found to be less exothermic for $BaZrO_3$ than for $BaPrO_3$ and $BaThO_3$, but in all cases indicating that the proton concentration would decrease with increasing temperature, in accord with the available thermodynamic data[120, 135, 157]. Further to the energetics, the local environment of a proton was studied. The relaxed geometries suggested that the equilibrium O-H bond was perpendicular to the line between two adjacent Zr or Pr ions.

To further understand the proton conducting capabilities of these phases the binding energies for dopant-OH pairs were calculated and the results showed that in $BaZrO_3$ the weakest association energies were for Gd and Y dopants, and the strongest association energies for Sc. These results confirm that local proton trapping and mobility would be very sensitive to the acceptor dopant ion. Our results are compatible with recent Neutron-Spin-Echo measurements [126] of hydrated Y-doped $BaZrO_3$, which report data that are indicative of proton trapping. The high binding energies for all the dopant-OH pair clusters in $BaPrO_3$ and $BaThO_3$ suggest strong proton trapping effects, which would be detrimental to proton conductivity.

Finally, the oxide-ion migration pathways were examined to determine if mixed-ion conduction was possible. The pathway for oxide ion migration was predicted to be a curved path for $BaPrO_3$ and $BaThO_3$ and a linear path for the $BaZrO_3$ system. The energetics of the lowest energy path in the $BaThO_3$ and $BaZrO_3$ were shown to be sufficiently low to allow possible oxide ion migration at high temperatures.

To extend this study, DFT methods could be applied to further investigate the trends described in this work, which could include proton migration pathways and binding effects.

6.4 Simulation Studies of the New Multiferroic Material $BiFeO_3$

In chapter 5 we applied atomistic simulation techniques for the first time to study the topical $BiFeO_3$ phase and to contribute to the understanding of key properties that are related to its potential use as an oxide-ion conductor and multiferroic applications. We began the investigation by developing a new potential model for $BiFeO_3$. We reproduced the crystal structure and the model was then applied to the energetics of intrinsic atomic defects. The results of these calculations suggested that intrinsic disorder of the Frenkel and Schottky type was unlikely and the reduction process involving the formation of oxygen vacancies and Fe^{2+} is the

most favourable. As some have suggested, these results confirm that deviations from oxygen stoichiometry with oxygen vacancies are likely to play a crucial role in the multiferroic properties of $BiFeO_3$.

We then investigated the effects of doping within $BiFeO_3$. For 2+ and 3+ cation doping our results showed that the solution energy is largely influenced by ion size effects with smaller dopants (e.g. Mg^{2+}, Ga^{3+}) favouring the Fe-site and larger dopants (e.g. Sr^{2+}, Nd^{3+}) the Bi-site. In addition, the Gd^{3+} dopant is found to sit at a "crossover" point in our solution energies for Bi versus Fe substitution. This suggests possible "ambi-site" behaviour in which the dopant can occupy either site. For the higher valent cations (e.g. Ti^{4+}, Nb^{5+}) are predicted to substitute preferentially for the Fe-site charge-compensated by the filling of oxygen vacancies, which has been suggested as an explanation for observed reduction in current leakage.

After experimental work suggested the possibility of oxide-ion conduction, we decided to investigate $BiFeO_3$ as an ion conductor. We calculated the activation energy for oxygen vacancy migration to be about 0.47 eV, which would suggest that $BiFeO_3$ would be a good oxide-ion conductor. The pathway for oxygen vacancy migration is predicted to be a curved trajectory between oxygen sites, with anisotropic long range migration within the distorted perovskite structure. However, long-range isotropic migration could be possible by using a higher energy pathway with an energy of 0.93 eV, which means this process is more likely at higher temperatures.

We investigated the binding energies for dopant-oxygen vacancy clusters in acceptor doped $BiFeO_3$. Our results showed that Ca and Sr doping on the Bi site gave the least binding energies and that substituting onto the Fe site would trap an oxygen vacancy.

In terms of future work, investigating larger and more complex dopant vacancy clusters would give better insight into the effects doping may have upon the physical properties of this phase. Further study of the oxide-ion migration mechanisms

are key, using the molecular dynamics (MD) methods to investigate temperature dependence and diffusion coefficients.

Appendix A

Modelling of Bi_3ReO_8

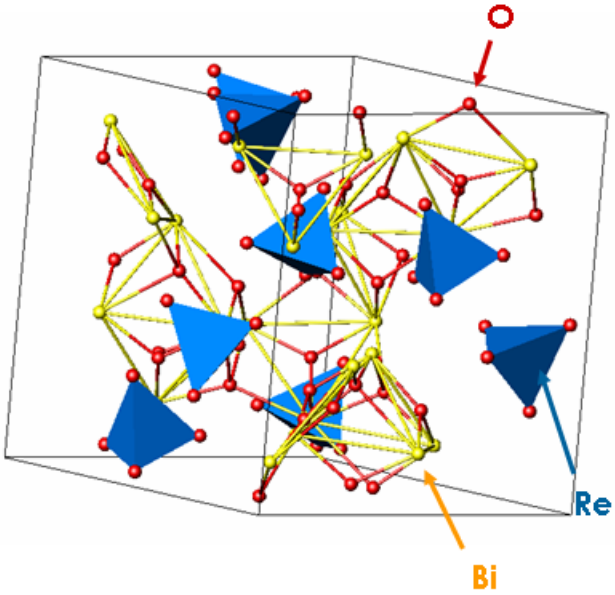

Figure A.1: Crystal structure of Bi_3ReO_8

Bi_3ReO_8 is thought to be the most stable compound of the Bi_2O_3-Re_2O_7 system, and was chosen to aid in the developement of the Re-O potential as it includes ReO_4 moieties. The crystal structure of Bi_3ReO_8 is fluorite-related and cubic, with a = 11.590(1) Å and in space group $P2_13$ [226]. This structure is illustrated in Figure A.1 and atom positions are listed in Table A.1.

Empirical fitting techniques (see chapter 2.2) were used to derive a new set of parameters for the $Re^{7+}\cdots O^{2-}$ potential (table A.2).

This $Re^{7+}\cdots O^{2-}$ was tested with a number of $O^{2-}\cdots O^{2-}$ potentials. The combination of potentials that best reproduced the Bi_3ReO_8 cell parameters are shown in Table A.3(i). Table A.3(ii) lists the calculated cell parameters in comparison to the experimental data for the two potentials in A.3(i). Examination of Table A.3(ii) suggest that both of these potential models accurately reproduce the Bi_3ReO_8 phase. Appendix E contains a summary of all candidate potential sets.

Table A.1: Refined atomic parameters for Bi_3ReO_8

atom	x	y	z
Re1	0.1192	0.1192	0.1192
Re2	0.6192	0.6192	0.6192
Bi1	0.1448	0.3513	0.3890
Bi2	0.1193	0.1530	0.6308
O1	0.0323	0.0323	0.0323
O2	0.5319	0.5319	0.5319
O3	0.1391	0.2543	0.0570
O4	0.6163	0.7589	0.5674
O5	0.2911	0.2911	0.2911
O6	0.7797	0.7797	0.7797
O7	0.2329	0.2140	0.4935
O8	0.2605	0.5399	0.0019

Table A.2: Interatomic potentials for Re^{7+} interactions derived from Bi_3ReO_8

Interaction	A (eV)	ρ (Å)	C (eV Å^6)
$Re^{7+} \cdots O^{2-}$	1023.16	0.4383	0.0
$Re^{7+} \cdots Re^{7+}$	0.000968	0.3284	0.0

Table A.3: Alternative $O^{2-} \cdots O^{2-}$ potentials

(i) Short-range and shell model parameters

$O^{2-} \cdots O^{2-}$	A (eV)	ρ (Å)	C (eV Å^6)	Y (e)	k (eV Å^{-2})	Ref
#1	22764.3	0.149	27.88	-2.860	74.92	[227]
#2	15123.6	0.223	23.43	-2.470	23.09	[228]

(ii) Deviation of calculated Bi_3ReO_8 cell parameters from experiment

$O^{2-} \cdots O^{2-}$	Δvol (%)	Δa (%)	Δb (%)	Δc (%)	$\Delta\beta$ (%)
#1	0.87	0.29	0.29	0.29	0.0
#2	-0.89	-0.30	-0.30	-0.30	0.0

Appendix B

Modelling of La_3ReO_8

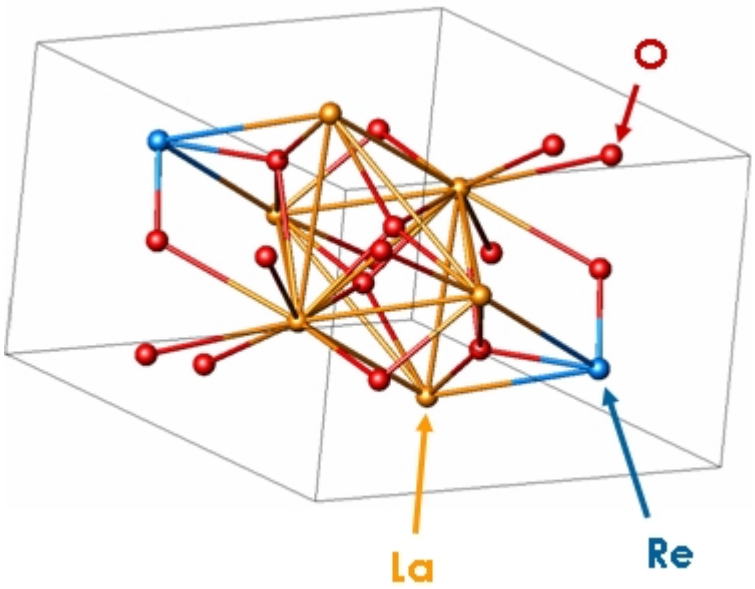

Figure B.1: Crystal structure of La_3ReO_8

Table B.1: Refined atomic parameters for La_3ReO_8

atom	x	y	z
Re1	0.1814	0.8187	0.7500
La1	0.3390	0.1071	0.2500
La2	0.6018	0.3978	0.7500
La3	0.1073	0.3384	0.7500
O1	0.3381	0.3384	0.0044
O2	0.1912	0.8060	0.0672
O3	0.6009	0.9891	0.2500
O4	0.6480	0.3440	0.2500
O5	0.0117	0.3867	0.2500
O6	0.0312	0.1172	0.2500

The crystal structure of high-temperature monoclinic La_3ReO_8 belongs to space group P21/m, with a = 7.757(1)Å, b = 7.777(1)Å, c = 5.928(1) Å, and $\gamma = 111.1°$. This phase was chosen to develop the Re-O potential because the Re^{7+} sits within slightly distorted ReO_6^{5-} octahedra as represented in Figure B.1. Table B.1 contains the refined atomic positions for La_3ReO_8.

The start of the empirical fitting process for La_3ReO_8 was identical to the previous Bi_3ReO_8 study. The same starting point for the $Re^{7+}\cdots O^{2-}$ potential and the original $O^{2-}\cdots O^{2-}$ potential was used (table 3.7). A $Re^{7+}\cdots O^{2-}$ potential was generated from this fitting ($Re^{7+}\cdots O^{2-}$ (1) (table B.2(i)). However, this potential

Table B.2

(i) Interatomic potentials for Re^{7+} interactions derived from La_3ReO_8

Interaction	A (eV)	ρ (Å)	C (eV Å^6)
$Re^{7+} \cdots O^{2-}$ (1)	1187.87	0.4632	0.0
$Re^{7+} \cdots O^{2-}$ (2)	3275.29	0.35	0.0

(ii) Deviation of calculated La_3ReO_8 cell parameters from experiment

Interaction	Δvol (%)	Δa (%)	Δb (%)	Δc (%)	$\Delta\beta$ (%)
$Re^{7+} \cdots O^{2-}$ (1)	33.37	-1.34	10.64	27.53	0.0
$Re^{7+} \cdots O^{2-}$ (2)	14.24	0.69	0.43	15.40	0.0

Table B.3

(i) Interatomic potentials for Re^{7+} interactions derived from simultaneous fitting

Interaction	A (eV)	ρ (Å)	C (eV Å^6)
$Re^{7+} \cdots O^{2-}$	12268.18	0.2418	0.0

(ii) Deviation of calculated Bi_3ReO_8 and La_3ReO_8 cell parameters from experiment

structure	Δvol (%)	Δa (%)	Δb (%)	Δc (%)	$\Delta\beta$ (%)
Bi_3ReO_8	-22.62	-8.19	-8.19	-8.19	0.0
La_3ReO_8	1.66	-2.63	-2.89	6.33	0.0

still showed overall poor structural reproduction, as evidenced by Table B.2(ii).

Another development approach was undertaken, by using extreme start points for our fitting study as to discount the possibility of a local energy minima in the parameter profile being reached. This potential set became another candidate for use on the $Bi_{28}Re_2O_{49}$ structure (potential set (3), Table E.2)

A final candidate potential model was created by taking potential set (1) (appendix II, Table IIc) from the Bi_3ReO_8 empirical fitting, and then simultaneously fitting the potential to both Bi_3ReO_8 and La_3ReO_8.

Appendix C

Published Paper - Defect chemistry and proton-dopant association in $BaZrO_3$ and $BaPrO_3$

J. Mater. Chem. **20** 6258 (2010)

View Online

Defect chemistry and proton-dopant association in $BaZrO_3$ and $BaPrO_3$†

Stephen J. Stokes and M. Saiful Islam*

Received 5th February 2010, Accepted 24th May 2010
DOI: 10.1039/c0jm00328j

Defect reactions, water incorporation and proton-dopant association in the $BaZrO_3$ and $BaPrO_3$ perovskite materials are investigated using well-established atomistic simulation techniques. The interatomic potential models reproduce the experimental cubic $BaZrO_3$ and orthorhombic BaPrO3 structures. The high defect energies suggest that significant intrinsic disorder (either Frenkel, Schottky or reduction) in $BaZrO_3$ is unlikely, which is consistent with the relative chemical stability of this system. In contrast, favourable redox processes are found for intrinsic reduction of $BaPrO_3$, and oxidation of acceptor-doped $BaPrO_3$, the latter leading to p-type conduction properties as observed experimentally. Binding energies for dopant-OH pairs in $BaZrO_3$ indicate the weakest association for Gd and Y dopants, and the strongest association for Sc. The high binding energies for all the dopant-OH pair clusters in $BaPrO_3$ suggest strong proton trapping effects, which would be detrimental to proton conductivity. The water incorporation or hydration energy is found to be less exothermic for $BaZrO_3$ than for $BaPrO_3$, the higher exothermic value for the latter suggesting that water incorporation extends to higher temperatures in accord with the available thermodynamic data. The energies and pathways for oxide ion migration in both materials are also investigated.

Published on 22 June 2010 on http://pubs.rsc.org | doi:10.1039/C0JM00328J
Downloaded by University of Bath on 17 September 2010

1 Introduction

Solid-state proton conductors based on cerate and zirconate perovskite oxides have attracted considerable attention for a range of electrochemical applications, such as fuel cells, seperation membranes and steam electrolysers.[1–7] Such oxide materials are particularly attractive as electrolytes for solid oxide fuel cells (SOFCs) operating at intermediate temperatures (400–700 °C), in contrast to high temperature operation (> 900 °C) of SOFCs based on the Y/ZrO_2 oxide-ion conductor.

Of the known perovskite-type proton conductors, there has been considerable experimental[8–30] and computational[31–39] interest in acceptor-doped $BaZrO_3$ due to its high proton conductivity in a cubic structure coupled with good chemical and mechanical stability. The proton mobility in Y-doped $BaZrO_3$ is among one of the highest ever reported for a perovskite-type proton conductor, and has the potential to operate at lower temperatures than the conventional SOFC electrolyte. There has also been recent interest in some less-studied Ba-based perovskites as potential proton conductors including acceptor-doped $BaPrO_3$,[40–48] but the thermodynamic and conduction properties of these materials are not fully characterised.

It is known that defect reactions and atomistic diffusion mechanisms underpins the fundamental understanding of proton conduction behaviour. However, there is often limited atomic-scale information on complex ceramic oxides, such as lattice defects, local proton sites and the extent of interactions between the dopant ion and the protonic defect leading to possible proton trapping. Yamazaki *et al.*[23] have reported thermogravimetry studies of the water incorporation reaction in Y-doped $BaZrO_3$ and determined hydration enthalpies that are substantially smaller than those reported previously.[8] In support of previous computer modelling predictions[39,39] recent Neutron-Spin-Echo experiments[14] on hydrated $BaZr_{0.90}Y_{0.10}O_{2.95}$ report data that are indicative of trapping effects in which the proton spends an extended time in the vicinity of the Y dopant before further proton diffusion.

This study attempts to provide further insight into these issues by using atomistic simulation techniques, which have been applied successfully in studies of ionic conduction in a range of complex oxides including $CaZrO_3$,[49,50] $ACeO_3$,[51–53] and $LaBaGaO_4$.[54,55] This paper presents recent computational studies of topical proton-conducting perovskites based upon $BaZrO_3$ and $BaPrO_3$, with an examination of trends and direct comparison with experimental data where available. Emphasis here is placed on probing the defect chemistry, proton sites, dopant-OH association and oxygen ion migration on the atomic-scale.

2 Simulation methods

Detailed reviews of these well established techniques are given elsewhere,[56] so only a brief account will be presented here. The calculations are within the framework of the Born model of ionic solids, with ion-ion interactions treated by long-range Coulombic terms and short-range forces that account for electron cloud overlap (Pauli repulsion) and dispersion (Van der Waals) interactions. The short-range interactions are modelled with a Buckingham interatomic potential:

Department of Chemistry, University of Bath, Bath, BA2 7AY, UK. E-mail: M.S.Islam@bath.ac.uk

† This paper is part of a *Journal of Materials Chemistry* themed issue on proton transport for fuel cells. Guest editors: Sossina Haile and Peter Pintauro.

 This journal is © The Royal Society of Chemistry 2010

View Online

Published on 22 June 2010 on http://pubs.rsc.org | doi:10.1039/C0JM00328J
Downloaded by University of Bath on 17 September 2010

Table 1 Interatomic potentials and shell model parameters for $BaZrO_3$ and $BaPrO_3$

(i) short-range			
Interaction	A (eV)	ρ (Å)	C (eV Å^6)
$Ba^{2+}\cdots O^{2-}$	931.700	0.3949	0.000
$Zr^{4+}\cdots O^{2-}$	985.869	0.3760	0.000
$Pr^{4+}\cdots O^{2-}$	1925.382	0.3511	21.152
$O^{2-}\cdots O^{2-}$	22764.300	0.1490	27.890
(ii) shell model			
Species	$Y(e)$		k (eV Å^{-2})
Ba^{2+}	1.460		14.800
Zr^{4+}	1.350		169.617
Pr^{4+}	7.7		291
O^{2-}	−2.077		27.300

Table 2 Parameters for O–H interaction

Morse potential	D (eV)	β (Å^{-1})	r_0 (Å)
O···H	7.0525	2.1986	0.9485
Buckingham potential	A (eV)	ρ (Å)	C (eV Å^6)
O···H	311.97	0.25	0

$$V_{ij}(r) = A\exp^{-r/\rho_{ij}} - \frac{C_{ij}}{r^6} \quad (1)$$

where A_{ij}, r_{ij} and C_{ij} are empirically derived parameters for each ion-ion interaction. Polarisability of the ions is incorporated by using the Dick–Overhauser shell model.[57] The lattice energy calculations employ the now standard Ewald summation procedures for the Coulombic interactions.

An important feature of the calculations is the treatment of lattice relaxation about the point defect or dopant. The Mott-Littleton approach[58] used here involves the partitioning of the crystal lattice into two regions so that over 500 ions within the spherical inner region surrounding the defect are relaxed explicitly. The remainder of the crystal, where the defect forces are relatively weak, are treated by more approximate quasi-continuum methods. In this way, local relaxation about the defect or impurity was effectively modelled and the crystal was not considered simply as a rigid lattice. These methods are embodied in the GULP simulation code.[59]

The interatomic potential and shell model parameters for $BaZrO_3$ and $BaPrO_3$ are listed in Table 1. The parameters for Ba–O, Zr–O and O–O have been transferred from previous simulation studies,[60,61] and those for Pr–O have been derived empirically for this study. For the protonic defect, the O–H interaction was modelled using an attractive Morse potential

$$V(r) = D\{1 - \exp[-\beta(r - r_0)]\}^2 \quad (2)$$

using parameters (Table 2) developed from ab initio quantum mechanical cluster calculations, with a point charge representation of the surrounding lattice.[62] The dipole of the hydroxyl species was distributed across both ions to give an overall charge of −1 with O assigned −1.4263 and H +0.4263. An additional Buckingham potential describing the interaction between the hydroxyl group and the lattice ions was taken from previous studies of water incorporation in silicates.[63] This simulation approach has been applied successfully to other proton-conducting perovskites,[49,50,52,64] and more recently, to water incorporation in Si/Ge-apatites.[65]

3 Results and discussion

3.1 Structural modelling and defect formation

The starting point of the study, before carrying out defect calculations, was to reproduce the experimentally observed crystal structures. The unit cell dimensions and ion positions were equilibrated under constant pressure conditions. The calculated structures of cubic $BaZrO_3$ and orthorhombic $BaPrO_3$ are compared with experiment in Table 3. The unit cell parameters change only slightly on relaxation of the structures. The differences in the observed and calculated lattice parameters and bond lengths are all within 0.09Å, and in many cases less than 0.03Å, indicating that the potentials reproduce these perovskite structures.

Energies of isolated point defects (vacancies and interstitials) were then calculated for $BaZrO_3$ and $BaPrO_3$. The isolated defect energies were combined to give the energies of formation of Frenkel and Schottky defects based on the following eqn (3)–(8); note that Kroger-Vink notation is used where, for example, $O_O^{\times}$, $V_O^{\bullet\bullet}$ and O''_i, indicates a lattice anion, an oxygen vacancy (+2 effective charge) and an oxygen interstitial (-2 effective charge) respectively.

Ba Frenkel:

$$Ba_{Ba}^{\times} \rightarrow V''_{Ba} + Ba_i^{\bullet\bullet} \quad (3)$$

M Frenkel:

$$M_M^{\times} \rightarrow V^{4\prime}_{M} + M_i^{4\bullet} \quad (4)$$

O Frenkel:

$$O_O^{\times} \rightarrow V_O^{\bullet\bullet} + O''_i \quad (5)$$

Schottky:

$$Ba_{Ba}^{\times} + M_M^{\times} + 3O_O^{\times} \rightarrow V''_{Ba} + V^{4\prime}_{M} + 3V_O^{\bullet\bullet} + BaMO_3 \quad (6)$$

BaO Schottky-type:

$$Ba_{Ba}^{\times} + O_O^{\times} \rightarrow V''_{Ba} + V_O^{\bullet\bullet} + BaO \quad (7)$$

Table 3 Experimental and calculated lattice parameters and mean bond lengths for $BaZrO_3$ and $BaPrO_3$

Parameter	Exp	Calc	δ
$BaZrO_3$[a]			
a = b = c/Å	4.199	4.188	−0.011
Ba-O/Å	2.969	2.961	−0.008
Zr-O/Å	2.099	2.094	−0.005
$BaPrO_3$[b]			
a/Å	6.181	6.213	−0.032
b/Å	6.214	6.221	−0.007
c/Å	8.722	8.789	−0.067
Ba-O1/Å	3.114	3.111	−0.003
Ba-O2/Å	3.016	3.110	0.093
Pr-O1/Å	2.227	2.205	0.022
Pr-O2/Å	2.223	2.203	0.020

[a] Ref. 66. [b] Ref. 67.

View Online

MO_2 Schottky-type:

$$M_M^{\times} + 2O_O^{\times} \rightarrow V^{4\prime}{}_M + 2V_O^{\bullet\bullet} + MO_2 \quad (8)$$

The resulting energies are listed in Table 4 which reveal two main points. First, the creation of Frenkel defects is associated with substantial amounts of energy, confirming that the close-packed perovskite structure is highly unlikely to accommodate ion interstitials. Second, the most favourable energy is found for the BaO Schottky-type disorder for both systems, with the lowest value of 2.13 eV for $BaPrO_3$. This suggests the possible loss of BaO at very high temperatures. It has been found that $BaPrO_3$-based compounds seem to exhibit greater chemical instability.

Most applications of proton conductors require them to be used under a range of redox (reducing or oxidising) conditions. For the undoped system, the following reaction for reduction can be considered involving the creation of oxygen vacancies and electronic defects:

$$O_O^{\times} \rightarrow V_O^{\bullet\bullet} + \frac{1}{2}O_{2(g)} + 2e' \quad (9)$$

For an extrinsic system, where oxygen vacancies already exist due to acceptor doping, oxidation can occur *via* the following reaction:

$$V_O^{\bullet\bullet} + \frac{1}{2}O_{2(g)} \rightarrow O_O^{\times} + 2h^{\bullet} \quad (10)$$

in which the oxygen vacancies are filled to create electron holes ($h^{\bullet}$). Our approach to electronic defects in $BaZrO_3$ and $BaPrO_3$ follows that used for the $BaCeO_3$ and $SrCeO_3$ perovskites,[52,64] in which the hole/electronic species are treated as small polarons localised at ion sites: hence, hole centres are modelled as a O^- substituted at O^{2-} and the electron centres (e') as a M^{3+} substituted at M^{4+}. The corresponding interatomic potentials are transferred directly for the short-range Buckingham parameters, but the shell model is modified by changing the shell charge by one. Using these electronic terms, the energies of the redox reactions were calculated and are given in Table 5. Owing to the uncertainties in the free-ion terms employed, we must be cautious in giving detailed interpretations, although these methods have been shown to provide reliable trends in overall redox energies.

Table 4 Energies of Frenkel and Schottky disorder in $BaZrO_3$ and $BaPrO_3$ (eV/defect)

Type	$BaZrO_3$	$BaPrO_3$
Ba Frenkel	6.97	5.96
M Frenkel	10.22	12.78
O Frenkel	5.58	4.89
Schottky	3.20	4.49
BaO Schottky-type	2.80	2.13
MO_2 Schottky-type	3.75	5.30

Table 5 Energies of redox reactions in $BaZrO_3$ and $BaPrO_3$ (eV/electronic defect)

Type	$BaZrO_3$	$BaPrO_3$
Oxidation	2.90	2.15
Reduction	6.23	1.14

The results show that the lowest oxidation and reduction energies are found for the $BaPrO_3$ system, suggesting a greater concentration of electronic defects in this material. For the doped material, p-type conductivity will be exhibited with increasing oxygen partial pressures. Indeed, Furøy *et al.*[40] show that Gd-doped $BaPrO_3$ is dominated by electronic holes at lower temperatures in oxidising atmospheres, making it a p-type conductor. Similarly, Magraso *et al.*[47] find that Gd-doped $BaPrO_3$ is largely a p-type conductor.

The lowest defect reaction energy is for intrinsic reduction of $BaPrO_3$ with the formation of oxygen vacancies and electronic species (Pr^{3+}). Furøy *et al.*[40] find that the $BaPrO_3$ system is unstable towards reduction, while photoemission spectroscopy measurements of Mimuro *et al.*[46] indicate the presence of Pr^{3+} in the intrinsic region.

The high reduction energy in $BaZrO_3$ indicates greater resistance to reduction than oxidation, as observed experimentally.[24] We note that entropic effects need to be included in our calculations to derive a quantitative relationship between oxygen partial pressure and defect concentration, which is a topic for further study. In general, these results are consistent with experimental findings of the two materials, which show mixed ionic/electronic conductivity and that p-type electronic conductivity increases with increasing oxygen activity especially for doped $BaPrO_3$.

3.2 Water incorporation and protonic defect

Acceptor doping with trivalent cations (typically Y, Yb or In) onto the Zr^{4+} or Pr^{4+} site generates oxygen vacancies as charge-compensating defects. The incorporation of water into the perovskite structure is achieved by treatment in water vapour, in which the oxygen vacancies are replaced by protonic defects (in the form of hydroxyl ions) as shown by the following equation,

$$H_2O + O_O^{\times} + V_O^{\bullet\bullet} \rightarrow 2OH_O^{\bullet} \quad (11)$$

Previous QM computational studies[8,31,32,36,68,69] have indicated that proton conduction in perovskites involves (i) proton hopping between neighbouring oxygens (Grotthuss mechanism) aided by local lattice softening and (ii) low activation barrier rotational motion of the hydroxyl group and rate-limiting proton transfer toward a neighbouring oxide ion. These studies also suggest possible quantum effects (tunnelling) for the proton jump. Hence, the characterisation of the local structure and O–H configurations is important.

As with previous studies,[49,52] our simulation techniques can be used to probe the proton site and examine the most energetically favourable O–H configuration. The simulations indicate that the equilibrium O–H bond lies perpendicular to the line between the two adjacent Zr^{4+} or Pr^{4+} ions (as shown in Fig. 1 for $BaZrO_3$). This configuration seems to maximise both the H-Ba^{2+} and the H-M^{4+} distances.

Unlike average structural techniques, our atomistic simulations reveal local ion relaxations around the protonic defect (illustrated in Fig. 1b) with a local distortion from cubic symmetry for $BaZrO_3$. An equilibrium O–H distance of 0.98Å is found, which lies close to accepted O–H bond lengths in perovskites.[3,4] Our calculated position for the H atom in $BaZrO_3$ is

Downloaded by University of Bath on 17 September 2010
Published on 22 June 2010 on http://pubs.rsc.org | doi:10.1039/C0JM00328J

This journal is © The Royal Society of Chemistry 2010

Downloaded by University of Bath on 17 September 2010
Published on 22 June 2010 on http://pubs.rsc.org | doi:10.1039/C0JM00328J

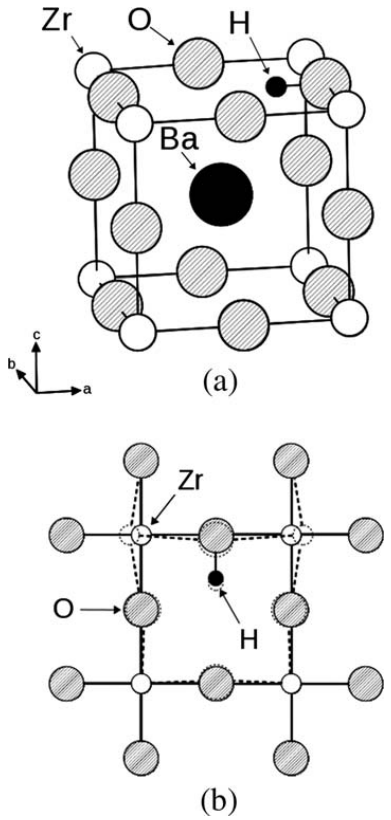

Fig. 1 Schematic of equilibrium O–H configuration in $BaZrO_3$ (a) Unit cell of cubic structure (b) relaxed (dotted line) and unrelaxed local structure in the a-b plane.

(0.5, 0.275, 0.0). These results accord well with the deuteron position refined from neutron powder diffraction data collected on deuterated and dry samples of $BaZr_{0.5}In_{0.5}O_{2.75}$ at 5 K and room temperature.[11]

Based on reaction (11), the energy of water incorporation, or hydration energy, (E_{H_2O}) can be calculated by using the following equation:

$$E_{H_2O} = 2E_{OH} - E_{VO}^{\bullet\bullet} + E_{PT} \quad (12)$$

where E_{OH} is the energy associated with substitution of O^{2-} with an OH– group, $E_{VO}^{\bullet\bullet}$ is the oxygen vacancy energy, and E_{PT} is the energy of the gas phase reaction $O^{2-} + H_2O = 2OH^-$. The latter term is estimated from the difference between proton affinities of O^{2-} and OH^-, and discussed in detail by Catlow and co-workers.[70,71]

Table 6 Defect and hydration energies in $BaZrO_3$ and $BaPrO_3$

	$BaZrO_3$	$BaPrO_3$
$E_{VO}^{\bullet\bullet}$/eV	18.56	19.01
E_{OH}/eV	15.11	14.67
Calc. E_{H_2O}/eV	−0.12	−1.45
Exp. E_{H_2O}/eV	−0.22 to −0.27[a], −0.82 to −0.97[b]	—

[a] Ref. 23. [b] Ref. 8.

The calculated hydration energies are listed in Table 6 and reveal two key features. First, E_{H_2O} is negative for both $BaZrO_3$ and $BaPrO_3$, which indicates that the materials will be dominated by protons at low temperatures and oxygen vacancies at high temperatures. Second, the magnitude of E_{H_2O} is notably less exothermic for $BaZrO_3$ than that for $BaPrO_3$. Yamazaki *et al.*[23] determine hydration enthalpies at low temperature for Y doped $BaZrO_3$ of −22 to −26 kJmol^{-1} (−0.22 to −0.27 eV) with varying dopant levels of 20 – 40%. As with our calculated value, these are significantly smaller in magnitude than the previously reported values for Y-doped $BaZrO_3$ of −79.4 to −93.3 kJmol^{-1} (−0.82 to −0.97 eV).[8] Yamazaki *et al.*[23] indicate that the smaller negative values in comparison with previous data are attributed to the restriction of the analysis to the low temperatures at which electronic hole concentrations can be neglected.

For $BaPrO_3$, there is no experimental hydration enthalpy for direct comparison partly due to the dominance of electronic behaviour. Mimuro *et al.*[46] indicate that the proton solubility increases with increasing dopant concentration in Yb-doped $BaPrO_3$, while Magraso *et al.*[47] find Gd-doped $BaPrO_3$ to be highly reactive under water, CO_2 and hydrogen containing atmospheres.

3.3 Proton-dopant interactions

There has been some debate as to whether there is any significant association between the dopant ion and the protonic defect (hydroxyl ion at oxygen site), which may affect proton mobility. In an attempt to probe the question of proton-dopant association, we have extended our previous studies on $SrCeO_3$[52] and $CaZrO_3$[69] with a series of calculations on OH-dopant pairs in $BaZrO_3$ and $BaPrO_3$ comprised of a hydroxyl ion and a neighbouring dopant substitutional (Fig. 2). With regard to the relaxed geometry, deviations from the equilibrium O–H configuration (shown in Fig. 1) are found, corresponding to a shift of

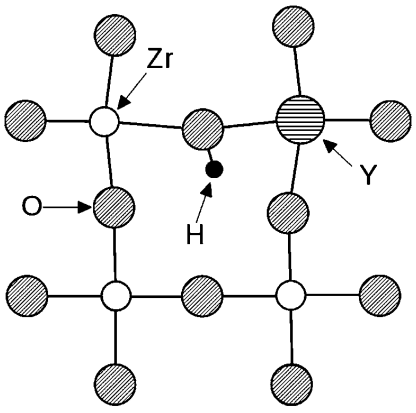

Fig. 2 Calculated local structure for the $OH_O^{\bullet}$-Y_{Zr}' pair cluster in $BaZrO_3$ showing local lattice relaxation.

View Online

Published on 22 June 2010 on http://pubs.rsc.org | doi:10.1039/C0JM00328J
Downloaded by University of Bath on 17 September 2010

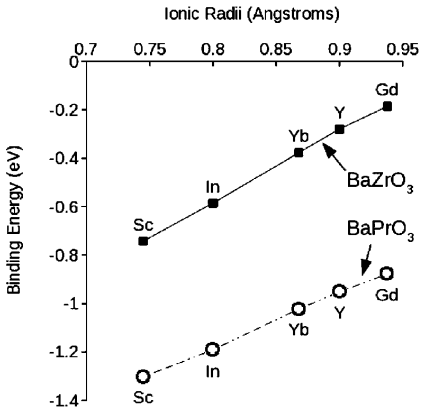

Fig. 3 Dopant-OH binding energies as a function of dopant ion size.

the H position towards a neighbouring oxygen and dopant ion (shown in Fig. 2 for Y^{3+} in $BaZrO_3$ as an example). As in Fig. 1b, the simulations reveal ion relaxations and local deviations from cubic symmetry in $BaZrO_3$.

The cluster binding energy (E_{bind}) for this configuration was calculated, which is defined as the difference between the energy of the cluster ($E_{cluster}$) and the sum of the energies of the corresponding isolated defects; this is given by the general relation:

$$E_{bind} = E_{cluster} - \left(\sum_{component} E_{isolated\ defect} \right) \quad (13)$$

where a negative value indicates that the cluster is stable with respect to the component isolated defects. For example, in the case of $BaZrO_3$ the binding energy is given by the relation:

$$E_{bind} = E(OH_O^{\bullet}\ M_{Zr}') - \{E(M_{Zr}') + E(OH_O^{\bullet})\} \quad (14)$$

Attention was focused on commonly used dopants in these materials, namely Sc, In, Y, Yb and Gd. The resulting energies (reported in Fig. 3) predict that all the hydroxyl-dopant pairs are favourable configurations. The lowest binding energy are for Y and Gd, and the strongest association is for Sc. These results indicate that proton mobility would be very sensitive to the type of acceptor dopant ion, and may be related to basicity as well ion size factors. It may be significant that a low binding energy is found for Y^{3+}, which is the most commonly used dopant in the $BaZrO_3$ proton conductor. It should be noted there is limited research relating to Gd-doped $BaZrO_3$ and hence our results show that Gd doping warrants further investigation.

Kreuer *et al.*[8] have investigated a range of alkaline-earth zirconates and titanates for potential electrochemical applications; they find that the system $BaZr_{1-x}Y_xO_{3-\delta}$ ($x = 0.1$) exhibits the highest proton mobility and the lowest activation enthalpy. In contrast, the lowest proton mobility and highest activation energy is found for Sc-doped $BaZrO_3$, for which we predict the strongest dopant-OH association. Our binding energy results for $BaPrO_3$ indicate extremely strong proton trapping by all of the acceptor dopants. This indicates significant impeding effects on long-range proton mobility, which would lead to low proton conductivity in doped $BaPrO_3$.

The interatomic distances between the M dopant and proton of the hydroxyl unit in the dopant-OH cluster have been analysed and are listed in Table 7. The analysis reveals that the distance between M and the proton (M–H) change with respect to the host Zr and Pr ions. The longest M–H distance are for the Gd and Y dopants, and mirrors the variation in binding energy (Fig. 3). Interestingly, the largest dopant (Gd) in $BaZrO_3$ is the only case in which the O–H bond does not swing towards the dopant ion, which can be related to the greater ion size mismatch between the Zr^{4+} and Gd^{3+} cations.

Although there are no quantitative experimental values for either $BaZrO_3$ or $BaPrO_3$ for direct comparison, our calculated binding energies agree well with proton "trapping" energies of about −0.2 and −0.4 eV for related Sc-doped $SrZrO_3$ and Yb-doped $SrCeO_3$ respectively, derived from muon spin relaxation (μSR) and quasi-elastic neutron scattering (QENS) experiments.[72,73] In accord with our previous simulations on dopant-OH interactions in $SrZrO_3$, $CaZrO_3$[49,69] and $SrCeO_3$,[52] Bjorketun *et al.*[35] also find proton-dopant cluster formation in $BaZrO_3$ from DFT-based calculations with association energies of about 0.2–0.4 eV. Moreover, recent Neutron-Spin-Echo (NSE) experiments[14] on proton dynamics in hydrated $BaZr_{0.90}Y_{0.10}O_{2.95}$ indicate proton trapping in which the proton spends an extended times in the vicinity of the Y dopant ions before further diffusion.

Table 7 Dopant-proton (M–H) distances in the pair cluster (Fig. 2) in $BaZrO_3$ and $BaPrO_3$

System	M^{3+}	ionic radius (Å)	M–H (Å)	ΔM–H(Å)
$BaZrO_3$				
	Zr	0.72	2.65	0.00
	Sc	0.75	2.25	−0.40
	In	0.80	2.29	−0.36
	Yb	0.87	2.36	−0.29
	Y	0.90	2.41	−0.24
	Gd	0.94	2.81	0.16
$BaPrO_3$				
	Pr	0.85	2.82	0.00
	Sc	0.75	2.24	−0.58
	In	0.80	2.27	−0.55
	Yb	0.87	2.31	−0.51
	Y	0.90	2.34	−0.48
	Gd	0.94	2.37	−0.45

3.4 Oxide-ion migration

The oxygen vacancies required for incorporation of protons may also migrate, particularly at high temperature (> 600 °C) when the exothermic incorporation of water is no longer favoured (eqn (11)). Whereas oxygen transport may be disadvantageous for certain applications, steam permeation (involving simultaneous diffusion of protons and oxygen vacancies) has been shown to inhibit coking of the anode in a proton conducting fuel cell operating on methane.[74] In this context, atomistic simulation of oxygen migration may greatly assist in our understanding of the energies and mechanistic features of oxygen transport in these $BaMO_3$ systems. Our simulation methods have previously been used to elucidate oxygen-ion migration pathways in many perovskite oxides.[52,53,55]

 This journal is © The Royal Society of Chemistry 2010

View Online

Downloaded by University of Bath on 17 September 2010
Published on 22 June 2010 on http://pubs.rsc.org | doi:10.1039/C0JM00328J

Table 8 Oxygen vacancy migration energies for $BaZrO_3$ and $BaPrO_3$

Compound	Calc E_{mig} (eV)	Exp E_{mig} (eV)
$BaZrO_3$	0.65	0.71[a]
$BaPrO_3$	0.93	—

[a] Ref. 13.

The energy profile of a migrating oxide ion was calculated by placing the ion at intermediate sites between adjacent oxygen vacancies along edges of a MO_6 octahedron. The migration energy (E_{mig}) for these pathways (listed in Table 8) show that $BaPrO_3$ has the highest value. It is important to note that these calculated migration energies (E_{mig}) relates to the intrinsic migration (or jump) of an oxygen vacancy, and does not include energies of defect formation or association. As with fluorite-oxides, the bulk activation energy for oxygen ion conduction in perovskites will usually consist of the migration term (Em) at high temperatures, but an additional binding term (E_{bind}) at low temperatures, leading to two slopes in the conductivity data. Hence, we recognise that direct comparison between our calculated migration energies and the experimental activation energies (E_a) is not straightforward. Also, the E_a values from experimental studies can show significant variation, which may reflect differences in synthesis conditions, phase purity or analysis of the conductivity data. Nevertheless, the calculated migration energy (0.65eV) for $BaZrO_3$ is consistent with the experimental activation energies ($\sim$ 0.7eV) for doped $BaZrO_3$ for high temperatures.[13]

It was found that for $BaPrO_3$ the migration pathway was not a linear pathway, but curved away from the M site cation, with a deviation from linear of about 0.3Å (Fig. 4). This is a common trait among perovskites which was first predicted for Sr/Mg doped $LaGaO_3$ using similar computational methods[53] and then observed experimentally using neutron diffraction and the maximum entropy method (MEM).[75] Unusually, $BaZrO_3$ was found to have a linear oxygen vacancy migration pathway, which would be interesting to examine using a similar neutron diffraction MEM analysis employed by Yashima *et al.*[75,76]

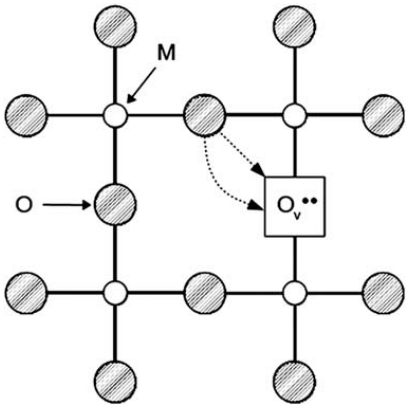

Fig. 4 Schematic representation of the linear and curved paths of oxygen migration in the ab plane of the $BaMO_3$ perovskite.

4 Conclusions

This study has provided atomic-scale insights into defect reactions and proton-dopant association in $BaZrO_3$ an $BaPrO_3$ materials, which are relevant to their proton transport properties for potential intermediate temperature SOFC applications. The main points are summarised as follows:

(1) The high defect energies indicate that significant intrinsic disorder (either Frenkel, Schottky or reduction) in $BaZrO_3$ is unlikely, which is consistent with the relative chemical stability of this system. In contrast, favourable redox energies are found for intrinsic reduction of $BaPrO_3$ (creating Pr^{3+} species), and oxidation of acceptor-doped $BaPrO_3$ (creating electronic holes). The latter result predicts p-type conductivity in doped $BaPrO_3$ in oxidising atmospheres, as observed experimentally.

(2) Binding energies for dopant-OH pairs in $BaZrO_3$ indicate the weakest association for Gd and Y dopants, and the strongest association for Sc. These results confirm that local proton trapping and mobility would be very sensitive to the type of acceptor dopant ion. The Gd-doped $BaZrO_3$ system may require further experimental investigation. Our results are compatible with recent Neutron-Spin-Echo measurements of hydrated Y-doped $BaZrO_3$, which report data that are indicative of proton trapping. For $BaPrO_3$ the high binding energies for all the dopant-OH pair clusters indicate strong proton trapping effects, which would be detrimental to proton conductivity.

(3) The water incorporation or hydration energy is found to be less exothermic for $BaZrO_3$ than for $BaPrO_3$, the higher exothermic value for the latter suggesting that water incorporation extends to higher temperatures, in accord with the available thermodynamic analysis. The simulations show significant local lattice relaxation around the OH defect and the OH-dopant clusters, with short-range distortions away from the average cubic symmetry of $BaZrO_3$, which will influence proton transport.

(4) Oxide ion migration is predicted to follow a curved path for $BaPrO_3$ (as observed for the $LaGaO_3$-based oxide-ion conductor), but a linear path for the $BaZrO_3$ system. This warrants further study by, for example, neutron diffraction and maximum entropy methods.

References

1 H. Iwahara, *Solid State Ionics*, 1992, **53-6**, 575.
2 H. Iwahara, T. Esaka, H. Uchida and N. Maeda, *Solid State Ionics*, 1981, **3–4**, 359.
3 K. D. Kreuer, *Annu. Rev. Mater. Res.*, 2003, **33**, 333.
4 K. D. Kreuer, S. J. Paddison, E. Spohr and M. Schuster, *Chem. Rev.*, 2004, **104**, 4637.
5 T. Norby, M. Wideroe, R. Glockner and Y. Larring, *Dalton Trans.*, 2004, **19**, 3012.
6 L. Malavasi, C. A. J. Fisher and M. S. Islam, *Chem. Soc. Rev.*, 2010, DOI: 10.1039/b915141a.
7 S. M. Haile, *Acta Mater.*, 2003, **51**, 5981.
8 K. D. Kreuer, S. Adams, W. Munch, A. Fuchs, U. Klock and J. Maier, *Solid State Ionics*, 2001, **145**, 295.
9 S. M. Haile, G. Staneff and K. H. Ryu, *J. Mater. Sci.*, 2001, **36**, 1149.
10 H. G. Bohn and T. Schober, *J. Am. Cer. Soc.*, 2000, **83**, 768.
11 I. Ahmed, C. S. Knee, M. Karlsson, S.-G. Eriksson, P. F. Henry, A. Matic, D. Engberg and L. Borjesson, *J. Alloys Compd.*, 2008, **450**, 103.
12 I. Ahmed, M. Karlsson, S.-G. Eriksson, E. Ahlberg, C. S. Knee, K. Larsson, A. K. Azad, A. Matic and L. Borjesson, *J. Am. Ceram. Soc.*, 2008, **91**, 3039.

View Online

Downloaded by University of Bath on 17 September 2010
Published on 22 June 2010 on http://pubs.rsc.org | doi:10.1039/C0JM00328J

13 I. Ahmed, S.-G. Eriksson, E. Ahlberg, C. S. Knee, H. Gotlind, L.-G. Johansson, M. Karlsson, A. Matic and L. Borjesson, *Solid State Ionics*, 2007, **178**, 515.
14 M. Karlsson, D. Engberg, M. E. Bjorketun, A. Matic, G. Wahnstrom, P. G. Sundell, P. Berastegui, I. Ahmed, P. Falus, B. Farago, L. Borjesson and S. Eriksson, *Chem. Mater.*, 2010, **22**, 740.
15 S. B. C. Duval, P. Holtappels, U. Stimming and T. Graule, *Solid State Ionics*, 2008, **179**, 1112.
16 N. Ito, H. Matsumoto, Y. Kawasaki, S. Okada and T. Ishihara, *Solid State Ionics*, 2008, **179**, 324.
17 M. Karlsson, A. Matic, C. S. Knee, I. Ahmed, S.-G. Eriksson and L. Borjesson, *Chem. Mater.*, 2008, **20**, 3480.
18 I. Antunes, A. Brandao, F. M. Figueiredo, J. R. Frade, J. Gracio and D. P. Fagg, *J. Solid State Chem.*, 2009, **182**, 2149.
19 M. Karlsson, A. Matic, D. Engberg, M. E. Bjorketun, M. M. Koza, I. Ahmed, G. Wahnstrom, L. Borjesson and S.-G. Eriksson, *Solid State Ionics*, 2009, **180**, 22.
20 F. Giannici, A. Longo, A. Balerna, K. D. Kreuer and A. Martorana, *Chem. Mater.*, 2009, **21**, 2641.
21 P. Babilo, T. Uda and S. M. Haile, *J. Mater. Res.*, 2007, **22**, 1322.
22 P. Babilo and S. M. Haile, *J. Am. Ceram. Soc.*, 2005, **88**, 2362.
23 Y. Yamazaki, P. Babilo and S. M. Haile, *Chem. Mater.*, 2008, **20**, 6352.
24 Y. Yamazaki, R. Hernandez-Sanchez and S. M. Haile, *Chem. Mater.*, 2009, **21**, 2755.
25 J. H. Shim, J. S. Park, J. An, T. M. Gur, S. Kang and F. B. Prinz, *Chem. Mater.*, 2009, **21**, 3290.
26 S. Zhang, L. Bi, L. Zhang, Z. Tao, W. Sun, H. Wang and W. Liu, *J. Power Sources*, 2009, **188**, 343.
27 J. R. Tolchard and T. Grande, *Solid State Ionics*, 2007, **178**, 593.
28 S. Tao and J. T. S. Irvine, *J. Solid State Chem.*, 2007, **180**, 3493.
29 A. K. Azad, C. Savaniu, S. Tao, S. Duval, P. Holtappels, R. M. Ibberson and J. T. S. Irvine, *J. Mater. Chem.*, 2008, **18**, 3414.
30 A. S. Patnaik and A. V. Virkar, *J. Electrochem. Soc.*, 2006, **153**, A1397–A1405.
31 K. D. Kreuer, *Solid State Ionics*, 1999, **125**, 285.
32 W. Munch, G. Seifert, K. D. Kreuer and J. Maier, *Solid State Ionics*, 1997, **97**, 39.
33 M. E. Bjorketun, P. G. Sundell and G. Wahnstrom, *Phys. Rev. B*, 2007, **76**, 054307.
34 B. Merinov and W. A. Goddard, *J. Chem. Phys.*, 2009, **130**, 194707.
35 M. E. Bjorketun, P. G. Sundell and G. Wahnstrom, *Faraday Discuss.*, 2007, **134**, 247.
36 P. G. Sundell, M. E. Bjorketun and G. Wahnstrom, *Phys. Rev. B*, 2007, **76**, 094301.
37 P. G. Sundell, M. E. Bjorketun and G. Wahnstrom, *Phys. Rev. B*, 2006, **73**, 104112.
38 Q. Zhang, G. Wahnstrom, M. E. Bjorketun, S. Gao and E. Wang, *Phys. Rev. Lett.*, 2008, **101**, 215902.
39 M. S. Islam, P. R. Slater, J. R. Tolchard and T. Dinges, *Dalton Trans.*, 2004, 3061.
40 K. A. Furoy, R. Haugsrud, M. Hansel, A. Magraso and T. Norby, *Solid State Ionics*, 2007, **178**, 461.
41 C. Y. Jones, J. Wu, L. P. Li and S. M. Haile, *J. Appl. Phys.*, 2005, **97**, 114908.
42 T. Fukui, S. Ohara and S. Kawatsu, *J. Power Sources*, 1998, **71**, 164.
43 C. S. Knee, A. Magraso, T. Norby and R. I. Smith, *J. Mater. Chem.*, 2009, **19**, 3238.
44 A. Magraso, A. Calleja, X. G. Capdevila and F. Espiell, *Solid State Ionics*, 2004, **166**, 359.
45 A. Magraso, F. Espiell, M. Segarra and J. T. S. Irvine, *J. Power Sources*, 2007, **169**, 53.
46 S. Mimuro, S. Shibako, Y. Oyama, K. Kobayashi, T. Higuchi, S. Shin and S. Yamaguchi, *Solid State Ionics*, 2007, **178**, 641.
47 A. Magraso, R. Haugsrud, M. Segarra and T. Norby, *J. Electroceram.*, 2009, **23**, 80.
48 P. J. Saines, B. J. Kennedy and R. I. Smith, *Mater. Res. Bull.*, 2009, **44**, 874.
49 R. A. Davies, M. S. Islam and J. D. Gale, *Solid State Ionics*, 1999, **126**, 323.
50 M. S. Islam, R. A. Davies, C. A. J. Fisher and A. V. Chadwick, *Solid State Ionics*, 2001, **145**, 333.
51 J. Wu, R. A. Davies, M. S. Islam and S. M. Haile, *Chem. Mater.*, 2005, **17**, 846.
52 G. C. Mather and M. S. Islam, *Chem. Mater.*, 2005, **17**, 1736.
53 M. S. Islam, *J. Mater. Chem.*, 2000, **10**, 1027.
54 E. Kendrick, J. Kendrick, K. S. Knight, M. S. Islam and P. R. Slater, *Nat. Mater.*, 2007, **6**, 871.
55 M. S. Islam and P. R. Slater, *MRS Bull.*, 2009, **34**, 935.
56 C. R. A. Catlow, *Solid State Chemistry: Techniques*, Clarendon Press, Oxford.
57 B. G. Dick and A. W. Overhauser, *Phys. Rev.*, 1958, **112**, 90.
58 N. F. Mott and M. J. Littleton, *J. Chem. Soc., Faraday Trans. 2*, 1989, **85**, 565.
59 J. D. Gale, *J. Chem. Soc., Faraday Trans.*, 1997, **93**, 629.
60 G. V. Lewis and C. R. A. Catlow, *J. Phys. C*, 1985, **18**, 1149.
61 M. S. Khan, M. S. Islam and D. R. Bates, *J. Mater. Chem.*, 1998, **8**, 2299.
62 P. Saul and C. R. A. Catlow, *Philos. Mag. B*, 1985, **51**, 107.
63 K. P. Schroder, J. Sauer, M. Leslie, C. R. A. Catlow and J. M. Thomas, *Chem. Phys. Lett.*, 1992, **188**, 320.
64 R. Glockner, M. S. Islam and T. Norby, *Solid State Ionics*, 1999, **122**, 145.
65 P. Panchmatia, A. Orera, J. Hanna, M. E. Smith, P. R. Slater and M. S. Islam, *J. Mater. Chem.*, 2010, **20**, 2766.
66 Y. Hinatsu, *J. Solid State Chem.*, 1996, **122**, 384.
67 A. J. Jacobson, B. Tofield and B. E. F. Fender, *Acta Crystallogr., Sect. B: Struct. Crystallogr. Cryst. Chem.*, 1972, **B28**, 956.
68 W. Munch, K. D. Kreuer, G. Seifert and J. Maier, *Solid State Ionics*, 2000, **136**, 183.
69 M. S. Islam, R. A. Davies and J. D. Gale, *Chem. Mater.*, 2001, **13**, 2049.
70 K. Wright, R. Freer and C. R. A. Catlow, *Phys. Chem. Miner.*, 1995, **20**, 500.
71 C. R. A. Catlow, *J. Phys. Chem. Solids*, 1977, **38**, 1131.
72 C. Karmonik, T. J. Udovic, R. L. Paul, J. J. Rush, K. Lind and R. Hempelmann, *Solid State Ionics*, 1998, **109**, 207.
73 R. Hempelmann, M. Soetratmo, O. Hartmann and R. Wappling, *Solid State Ionics*, 1998, **107**, 269.
74 W. G. Coors, *J. Power Sources*, 2003, **118**, 150.
75 M. Yashima, K. Nomura, H. Kageyama, Y. Miyazaki, N. Chitose and K. Adachi, *Chem. Phys. Lett.*, 2003, **380**, 391.
76 M. Yashima, *Solid State Ionics*, 2008, **179**, 797.

 This journal is © The Royal Society of Chemistry 2010

Appendix D

Published Paper - A Combined Total Scattering and Simulation Approach to Analyzing Defect Structure in Bi_3YO_6

Chem. Mater. **22** 4435 (2010)

CHEMISTRY OF MATERIALS
Article

Chem. Mater. **2010,** *22,* 4435–4445 4435
DOI:10.1021/cm101130a

A Combined Total Scattering and Simulation Approach to Analyzing Defect Structure in Bi_3YO_6

Isaac Abrahams,*,† Xi Liu,† Stephen Hull,‡ Stefan T. Norberg,‡,§ Franciszek Krok,∥ Anna Kozanecka-Szmigiel,∥ M. Saiful Islam,⊥ and Stephen J. Stokes⊥

†*Centre for Materials Research, School of Biological and Chemical Sciences, Queen Mary University of London, Mile End Road, London E1 4NS, United Kingdom,* ‡*ISIS Facility, Rutherford Appleton Laboratory, Chilton, Didcot, Oxon OX11 0QX, United Kingdom,* §*Department of Chemical and Biological Engineering, Chalmers University of Technology, SE-412 96 Gothenburg, Sweden,* ∥*Faculty of Physics, Warsaw University of Technology, ul. Koszykowa 75, 00-662, Warsaw, Poland, and* ⊥*Department of Chemistry, University of Bath, Bath BA2 7AY, United Kingdom*

Received April 22, 2010. Revised Manuscript Received June 24, 2010

The defect structure and electrical properties of the fast oxide ion-conducting solid electrolyte δ-Bi_3YO_6 have been studied using a combination of total neutron scattering analysis, energy minimization methods, and AC impedance spectroscopy. Conventional structural analysis using the Rietveld method reveals the oxide ions to be distributed over three crystallographic sites at room temperature, with a small change in this distribution at 800 °C. Analysis of short-range correlations using a total neutron scattering approach yields information on Bi and Y coordination environments. Careful analysis of the angular distribution functions derived from reverse Monte Carlo modeling of the total scattering data reveals physical evidence for a predominance of ⟨110⟩ vacancy ordering in this system. This ordering is confirmed as the lowest energy configuration in parallel energy minimization simulations.

1. Introduction

Many of the best anion-conducting solid electrolytes exhibit the fluorite structure and have applications in fuel cells, sensors, and oxygen pumps; well-known examples are yttrium-stabilized zirconia ($Zr_{1-x}Y_xO_{2-x/2}$, abbreviated as YSZ) and gadolinium-doped ceria ($Ce_{1-x}Gd_xO_{2-x/2}$, abbreviated as CGO).[1,2] The highest known oxide ion conductivity of any solid occurs in the defect fluorite δ-Bi_2O_3, with conductivities on the order of 1 S cm^{-1} at *ca.* 730 °C.[3] However, the stability window of this phase is rather limited and much research has been carried out with regard to stabilizing the high-temperature phase at substantially lower temperatures, mainly through solid-solution formation with other oxides.[4−8]

A variety of doped bismuth oxide phases have been isolated, some of which are closely related to the parent δ-Bi_2O_3. For example, the addition of Y_2O_3 to Bi_2O_3 has been shown to yield various phases.[3,9,10] The $Bi_2O_3-Y_2O_3$ binary system has been investigated by several authors, and their work has been extensively reviewed by Sammes et al.[7] The compound of composition Bi_3YO_6 shows particularly high oxide ion conductivity and was originally described as a pure δ-phase, stable at temperatures of <400 °C, by Datta and Meehan.[11] However, subsequent work by Watanabe's group[12−14] on compositions similar to that of Bi_3YO_6 suggests that, upon prolonged annealing at 650 °C, transformation of the δ-phase to a stable hexagonal phase occurs. This hexagonal phase converts rapidly back to the cubic phase at 720 °C and therefore they concluded that the room temperature δ-phase was formally a quenched metastable phase and that the kinetics of the cubic to hexagonal phase transition are very sluggish.

δ-Bi_3YO_6 is structurally very similar to δ-Bi_2O_3.[15,16] Y^{3+} being isovalent with Bi^{3+} results in the same nominal vacancy concentration in the yttrate as in the pure bismuth

*Author to whom correspondence should be addressed. Tel.: +44 207 882 3235. E-mail: i.abrahams@qmul.ac.uk.

(1) Steele, B. C. H. In *High Conductivity Solid Ionic Conductors*; Takahashi, T., Ed.; World Scientific: Singapore, 1989; p 402.
(2) Godickemeier, M.; Sasaki, K.; Gauckler, L. J. *J. Electrochem. Soc.* **1997**, *144*, 1635.
(3) Takahashi, T.; Iwahara, H.; Nagai, Y. *J. Appl. Electrochem.* **1972**, *2*, 97.
(4) Mairesse, G. In *Fast Ion Transport in Solids*; Scrosati, B., Magistris, A., Mari, C. M., Mariotto, G., Eds.; Kluwer Academic Publishers: Dordrecht, The Netherlands, 1993; p 271.
(5) Boivin, J. C.; Mairesse, G. *Chem. Mater.* **1998**, *10*, 2870.
(6) Shuk, P.; Wiemhöfer, H. D.; Guth, U.; Göpel, W.; Greenblatt, M. *Solid State Ionics* **1996**, *89*, 179.
(7) Sammes, N. M.; Tompsett, G. A.; Näfe, H.; Aldinger, F. *J. Eur. Ceram. Soc.* **1999**, *19*, 1801.
(8) Azad, A. M.; Larose, S.; Akbar, S. A. *J. Mater. Sci.* **1994**, *29*, 4135.
(9) Takahashi, T.; Iwahara, H.; Arao, T. *J. Appl. Electrochem.* **1975**, *5*, 187.
(10) Punn, R.; Feteira, A. M.; Sinclair, D. C.; Greaves, C. *J. Am. Chem. Soc.* **2006**, *128*, 15386.
(11) Datta, R. K.; Meehan, J. P. *Z. Anorg. Allg. Chem.* **1971**, *383*, 328.
(12) Watanabe, A.; Kikuchi, T. *Solid State Ionics* **1986**, *21*, 287.
(13) Watanabe, A. *Solid State Ionics* **1990**, *40/41*, 889.
(14) Watanabe, A. *Solid State Ionics* **1996**, *86−88*, 1427.
(15) Battle, P. D.; Catlow, C. R. A.; Drennan, J.; Murray, A. D. *J. Phys. C* **1983**, *16*, 561.
(16) Battle, P. D.; Catlow, C. R. A.; Heap, J. W.; Moroney, L. M. *J. Solid State Chem.* **1986**, *63*, 8.

© 2010 American Chemical Society
Published on Web 07/19/2010

oxide (1/4 of the available oxide ion sites in the fluorite structure are vacant in both systems). However, there are likely to be significant differences associated with the preferred coordination environments of Bi^{3+} and Y^{3+}, as evidenced by EXAFS studies.[17] Detailed characterization of the defect structure in these systems is key to understanding the ionic conduction mechanism. Nevertheless, since these phases are disordered on the crystallographic scale, conventional diffraction methods yield only an average picture. Short-range ordering manifests itself in the diffuse scattering, which appears as background features in powder diffraction patterns. Typically, the diffuse scattering is ignored in the analysis of crystalline diffraction patterns. However, recent advances in total scattering analysis have allowed for the inclusion of these data to yield a more complete picture of the short-range structure.[18]

Several studies have been carried out on modeling the undoped δ-Bi_2O_3 structure, in particular to assess the vacancy ordering. Jacobs and MacDonaill[19−22] investigated various models and found that ⟨111⟩-aligned vacancies were more stable than those aligned along ⟨100⟩, but that ⟨110⟩ vacancies are also present. Total energy calculations by Medvedeva et al.[23] also found ⟨111⟩ vacancy ordering to be the most stable. These findings are in contrast to those of Walsh et al.,[24] who used density functional theory (DFT) calculations to predict that ⟨100⟩ ordering is favored. In a recent detailed investigation by Aidhy et al.,[25] using molecular dynamics (MD) and *ab initio* methods, it was concluded that a combination of ⟨110⟩ and ⟨111⟩ vacancy alignment occurs. Even more recent publications, utilizing a combination of DFT and neutron total scattering data by Mohn et al.[26] and Hull et al.,[27] have shown that δ-Bi_2O_3 does not adopt a fluorite structure at the local scale, but instead favors an asymmetric Bi^{3+} coordination that is closely related to that found in the metastable β-Bi_2O_3 phase. Using maximum entropy methods (MEM) with powder neutron diffraction data, Yashima and Ishimura[28] found experimental evidence for diffusion pathways in both the ⟨111⟩- and ⟨100⟩-directions. These diffusion pathways were also consistent with an MEM analysis of the doped system δ-$Bi_{1.4}Yb_{0.6}O_3$ by the same authors.[29] Previous studies of diffuse neutron scattering in the bismuth yttrate fluorites were consistent with anion vacancy ordering in ⟨111⟩ and ⟨110⟩ directions.[16]

There are relatively few studies involving a combination of structural and computer modeling of doped bismuth oxides. Here, we present the results of a total scattering analysis of defect structure in δ-Bi_3YO_6, utilizing both Bragg and diffuse scattering, combined with energy minimization calculations, to give a more complete picture of the short-range ordering in this system.

2. Experimental Section

2.1. Sample Preparations. Samples of Bi_3YO_6 were prepared using appropriate amounts of Bi_2O_3 (Aldrich, 99.9%) and Y_2O_3 (Aldrich, 99.99%). Starting mixtures were ground in methylated spirits on a McCrone micronizing mill for 30 min. The dried mixtures were heated initially at 740 °C for 24 h, then cooled and reground. Powders were then reheated at 850 °C for 24 h and quenched in air to room temperature. For electrical measurements, reacted powders were pressed isostatically at a pressure of 400 MPa, then sintered at 800 °C for 10 h, before slow cooling in air to room temperature over a period of ∼12 h. Phase purity was confirmed by powder X-ray diffraction (XRD), as described below.

2.2. Electrical Measurements. Electrical parameters were determined by AC impedance spectroscopy up to *ca.* 800 °C, using a fully automated Solartron Model 1255/1286 system in the frequency range from 1 Hz to 5×10^5 Hz. Samples for impedance measurements were prepared as rectangular blocks (*ca.* 6 mm × 3 mm × 3 mm) cut from slow-cooled sintered pellets, using a diamond saw. Platinum electrodes were sputtered by cathodic discharge. Impedance spectra were recorded over two cycles of heating and cooling at stabilized programmed temperatures. Impedance at each frequency was measured repeatedly until consistency (2% tolerance in drift) was achieved or a maximum number of 25 repeats had been reached, as previously described.[30]

2.3. Crystallography. Powder XRD data were collected at room temperature and at 800 °C on a PANalytical X'Pert Pro diffractometer fitted with an X'Celerator detector, using nickel-filtered Cu Kα radiation (λ_1 = 1.54056 Å and λ_2 = 1.54439 Å) with an Anton-Paar HTK-15 high-temperature camera. Calibration was carried out with an external Si standard. Data were collected in flat plate θ/θ geometry over the 2θ range of 5°−120°, in steps of 0.033°, with a scan time of 200 s per step.

Powder neutron diffraction data were collected on the Polaris diffractometer at the ISIS facility located at the Rutherford Appleton Laboratory.[31] Data were collected on backscattering (130°−160°), 90° (85°−95°), low-angle (28°−42°), and very low angle (13°−15°) detectors. For the room-temperature total scattering experiment, the sample was contained in a cylindrical 11-mm-diameter vanadium can located in front of the backscattering detectors and a dataset of 1000 μA h collected. For the standard elevated temperature measurements, a sample was placed in an 11-mm-diameter vanadium can and placed in an evacuated furnace in front of the backscattering detectors. Short

(17) Battle, P. D.; Catlow, C. R. A.; Chadwick, A. V.; Cox, P.; Greaves, G. N.; Moroney, L. M. *J. Solid State Chem.* **1987**, *69*, 230.
(18) Keen., D. A. *J. Appl. Crystallogr.* **2001**, *34*, 172.
(19) Jacobs, P. W. M.; MacDonaill, D. A. *Solid State Ionics* **1986**, *18&19*, 209.
(20) Jacobs, P. W. M.; MacDonaill, D. A. *Solid State Ionics* **1987**, *23*, 279.
(21) Jacobs, P. W. M.; MacDonaill, D. A. *Solid State Ionics* **1987**, *23*, 295.
(22) Jacobs, P. W. M.; MacDonaill, D. A. *Solid State Ionics* **1987**, *23*, 307.
(23) Medvedeva, N. I.; Zhukov, V. P.; Gubanov, V. A.; Novikov, D. L.; Klein, M. L. *J. Phys. Chem. Solids* **1996**, *57*, 1243.
(24) Walsh, A.; Watson, G. W.; Payne, D. J.; Edgell, R. G.; Guo, J.; Glans, P.-A.; Learmont, T.; Smith, K. E. *Phys. Rev. B.* **2006**, *73*, 235104.
(25) Aidhy, D. S.; Nino, J. C.; Sinnott, S. B.; Wachsman, E. D.; Phillpot, S. R. *J. Am. Ceram. Soc.* **2008**, *91*, 2349.
(26) Mohn, C. E.; Stølen, S.; Norberg, S. T.; Hull, S. *Phys. Rev. Lett.* **2009**, *102*, 155502.
(27) Hull, S.; Norberg, S. T.; Tucker, M. G.; Eriksson, S. G.; Mohn, C. E.; Stølen, S. *Dalton Trans.* **2009**, 8737.
(28) Yashima, M.; Ishimura, D. *Chem. Phys. Lett.* **2003**, *378*, 395.
(29) Yashima, M.; Ishimura, D. *Appl. Phys. Lett.* **2005**, *87*, 221909.
(30) Dygas, J. R.; Kurek, P.; Breiter, M. W. *Electrochim. Acta* **1995**, *40*, 1545.
(31) Hull, S.; Smith, R. I.; David, W. I. F.; Hannon, A. C.; Mayers, J.; Cywinski, R. *Physica B* **1992**, *180−181*, 1000.

data collections of 30 μA h were made at temperatures from 300 °C to 800 °C, to allow for assessment of lattice expansion. For the total scattering study at 800 °C, a sample was sealed in an evacuated silica glass tube (8 mm diameter) and placed inside an 11-mm-diameter vanadium can inside an evacuated furnace in front of the backscattering detectors. An extended data collection of 1000 μA h was carried out at this temperature. For the total scattering analysis data corrections, diffraction data were collected on an empty silica tube inside a vanadium can for a similar time and under identical conditions to the sample. In addition, measurements of the empty furnace and a vanadium rod at room temperature were made, with the latter used to correct for the wavelength dependence of the incident neutron flux.

3. Data Analysis and Computer Simulations

3.1. Rietveld Analysis. Average structure refinement was carried out by conventional Rietveld analysis with the General Structure Analysis System (GSAS) suite of programs,[32] using a combination of X-ray and neutron datasets. A cubic model in space group $Fm\bar{3}m$ was used for all refinements. Bi and Y were located on the ideal 4*a* site (0,0,0) with oxide ions distributed over three sites: 8*c* at (0.25, 0.25, 0.25), 32*f* at approximately (0.3, 0.3, 0.3) and 48*i* at around (0.5, 0.2, 0.2).[33] For the data collected at 800 °C, the diffraction pattern of an empty silica tube was subtracted prior to refinement.

3.2. Total Neutron Scattering Analysis. Neutron diffraction datasets collected for Bi_3YO_6 at room temperature and at 800 °C were used in reverse Monte Carlo (RMC)[34] simulations to probe the instantaneous local ordering in the crystal structure. The effects of background scattering and beam attenuation were corrected for using the program Gudrun[35] and the resulting normalized total scattering structure factors, $S(Q)$ (where Q is the scattering vector defined as $2\pi/d$), were then used to obtain the corresponding total radial distribution function, $G(r)$, via Fourier transformation. The analysis of the total neutron scattering data (Bragg peaks plus diffuse scattering components) was carried out using the RMCProfile software.[36] All RMC simulations used configuration boxes of 10 × 10 × 10 unit cells, containing a total of 3000 Bi, 1000 Y, and 6000 O atoms. The initial model was based on the ideal fluorite structure with cations and anions randomly distributed over sites in the supercell corresponding to the regular 4*a* and 8*c* crystallographic sites, respectively, in the cubic $Fm\bar{3}m$ subcell. Fitting was carried out against the reciprocal space data, $S(Q)$, the real space data, $G(r)$, and the Bragg profile data, with the latter used to provide a constraint for the long-range crystallinity. The former was broadened by convolution with a box function to reflect the finite size of the simulation box:

$$S_{\mathrm{box}}(Q) = \frac{1}{\pi}\int_{-\infty}^{\infty} S_{\mathrm{expt}}(Q')\frac{\sin L(Q-Q')/2}{Q-Q'}\,\mathrm{d}Q' \quad (1)$$

where L is the smallest dimension of the RMC configuration and, as such, defines the upper limit of $G(r)$. Further details on the total scattering method have been described by Tucker et al.[36]

Calculations were performed using bond valence summation (BVS) constraints[37] and an O−O closest approach constraint ($g_{\mathrm{OO}}(r)$) to avoid unrealistically short O−O contacts. The BVS parameters used for the soft BVS constraint were all taken from Brese and O'Keeffe.[38] Cation swapping (one random cation swapping positions with a random cation of another atomic species) was tested and found to have no significant influence on the fit. Therefore, in the final calculations, only translational moves were permitted. The final fits to the $S_{\mathrm{box}}(Q)$ and $G(r)$ data for Bi_3YO_6 at room temperature and at 800 °C are shown in Figure 1.

3.3. Energy Minimization Simulations. The simulations were formulated within the framework of the Born model, the main features of which are the nature of the interatomic potentials and the description of perfect and defective lattices. The present account of these techniques will be brief, since comprehensive reviews have been given elsewhere.[39−42] The interactions between the ions were calculated taking into account long-range Coulombic forces and short-range forces that account for electron cloud overlap (Pauli repulsion) and dispersion (van der Waals) interactions. The short-range interactions were modeled with a Buckingham interatomic potential:

$$\phi_{\alpha\beta}(r) = \frac{Z_\alpha Z_\beta e^2}{4\pi\varepsilon_0 r} + A_{\alpha\beta}\exp\left(-\frac{r}{\rho_{\alpha\beta}}\right) - \frac{C_{\alpha\beta}}{r^6} \quad (2)$$

where $A_{\alpha\beta}$, $\rho_{\alpha\beta}$, and $C_{\alpha\beta}$ are potential parameters assigned to each ion−ion interaction; r is the distance between ions α and β, and Z_α and Z_β are their respective charges. The lattice energy calculations employ the now-standard Ewald summation procedures for the Coulombic interactions. Polarizability of the ions, which is an important parameter, especially for a lone-pair cation, was incorporated using the Dick−Overhauser[43] shell model.

An important feature of the calculations is the treatment of lattice relaxation about the point defect or dopant of interest. The Mott−Littleton approach used here involves the partitioning of the crystal lattice into two regions, so

(32) Larson, A. C.; Von Dreele, R. B. General Structure Analysis System; Los Alamos National Laboratory Report LAUR 8-748; Los Alamos National Laboratory: Los Alamos, NM, **1986**.
(33) Abrahams, I.; Kozanecka-Szmigiel, A.; Krok, F.; Wrobel, W.; Chan, S. C. M.; Dygas, J. R. *Solid State Ionics* **2006**, *177*, 1761.
(34) McGreevy, R. L. *J. Phys.: Condens. Matter* **2001**, *13*, R877.
(35) Soper, A. K. Unpublished software.
(36) Tucker, M. G.; Keen, D. A.; Dove, M. T.; Goodwin, A. L.; Hui, Q. *J. Phys.: Condens. Matter* **2007**, *19*, 335218.
(37) Norberg, S. T.; Tucker, M. G.; Hull, S. *J. Appl. Crystallogr.* **2009**, *42*, 179.
(38) Brese, N. E.; O'Keeffe, M. *Acta Crystallogr., Sect. B: Struct. Sci.* **1991**, *B47*, 192.
(39) Catlow, C. R. A.; Mackrodt, W. C. *Computer Simulation of Solids, Lecture Notes in Physics*; Springer: Berlin, 1982.
(40) Catlow, C. R. A. In *Solid State Chemistry-Techniques*; Cheetham, A. K., Day, P., Eds.; Clarendon Press: Oxford, U.K., 1987; p 231.
(41) Catlow, C. R. A. *Computer Modelling in Inorganic Crystallography*; Academic Press: San Diego, CA, 1997.
(42) Woodley, S. M.; Catlow, C. R. A. *Nat. Mater.* **2008**, *7*, 937.
(43) Dick, B. G.; Overhouser, A. W. *Phys. Rev.* **1958**, *112*, 90.

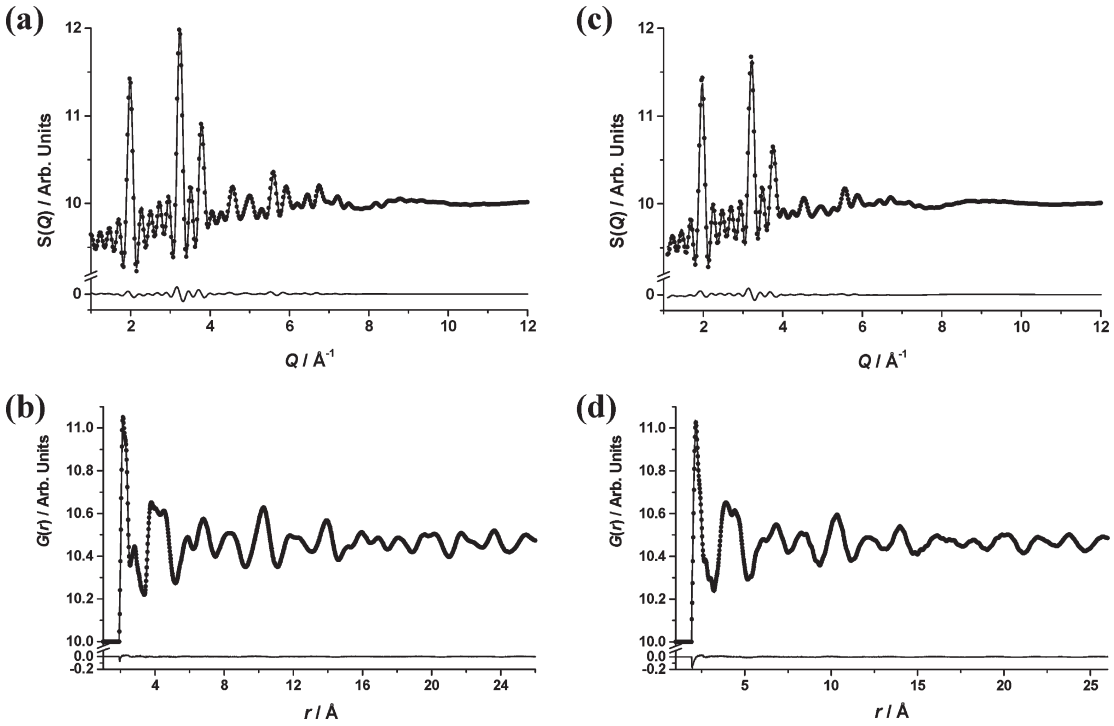

Figure 1. (a and c) Fitted total scattering $S(Q)$ and (b and d) total radial distribution $G(r)$ functions for Bi_3YO_6 at 25 °C (panels (a) and (b)) and 800 °C (panels (c) and (d)). Observed (points), calculated (line), and difference (lower) profiles are shown.

that ions within the spherical inner region surrounding the defect are relaxed explicitly. The remainder of the crystal, where the defect forces are relatively weak, are treated by more approximate quasi-continuum methods. In this way, local relaxation about the defect or impurity was effectively modeled and the crystal was not considered simply as a rigid lattice. These methods are embodied in the GULP simulation code,[44] and the techniques have been applied successfully to a range of materials including other bismuth-based oxides such as Bi_2WO_6 and $Bi_4Ti_3O_{12}$.[45−47]

Short-range parameters for Bi−O and Bi−Bi interactions and shell model parameters for each ion were taken directly from a previous study on Bi_2WO_6,[46] while the parameters of Y−O were taken from a study of binary and ternary oxides.[48] The parameters for the O−O interaction were obtained from work by Grimes et al.[49] The full set of interatomic potentials and shell model parameters used in the present study are listed in Table 1. For the present calculations, a supercell 27 times the size of the fluorite unit cell was constructed in space group $P1$, so that all atom sites within the cell could serve as locations for point defects. In creating this system, the anions were positioned only at the ideal fluorite anion site (8*c* in space group $Fm\bar{3}m$), to keep the occupancy of anion sites as simple as possible. Repetition of the unit cell in three dimensions ensured that the Y atoms were evenly distributed throughout the crystal lattice with maximum separation.

Table 1. Interatomic Potential and Shell Model Parameters Used for Bi_3YO_6

(a) Short-Range

interaction	A (eV)	ρ (Å)	C (eV Å^6)
$Bi^{3+}\cdots Bi^{3+}$	24244.5	0.3284	0
$Bi^{3+}\cdots O^{2-}$	49529.35	0.2223	0
$O^{2-}\cdots O^{2-}$	9547.96	0.2192	32
$Y^{3+}\cdots O^{2-}$	1519.279	0.3291	0

(b) Shell Model

species	shell charge (e)	force constant (eV Å^{-2})
Bi^{3+}	−5.51	359.55
O^{2-}	−2.04	6.3

4. Results and Discussion

4.1. Electrical Conductivity. The Arrhenius plot of total conductivity for Bi_3YO_6 is shown in Figure 2. The

(44) Gale, J. D. *J. Chem. Soc., Faraday Trans.* **1997**, *93*, 629.
(45) Pirovano, C.; Islam, M. S.; Vannier, R. N.; Nowogrocki, G.; Mairesse, G. *Solid State Ionics* **2001**, *140*, 115.
(46) Islam, M. S.; Lazure, S.; Vannier, R. N.; Nowogrocki, G.; Mairesse, G. *J. Mater. Chem.* **1998**, *8*, 655.
(47) Snedden, A.; Lightfoot, P.; Dinges, T.; Islam, M. S. *J. Solid State Chem.* **2004**, *177*, 3660.
(48) Bush, T. S.; Gale, J. D.; Catlow, C. R. A.; Battle, P. D. *J. Mater. Chem.* **1994**, *4*, 831.
(49) Grimes, R. W.; Busker, G.; McCoy, M. A.; Chroneos, A.; Kilner, J. A. *Ber. Bunsen. Phys. Chem.* **1997**, *101*, 1240.

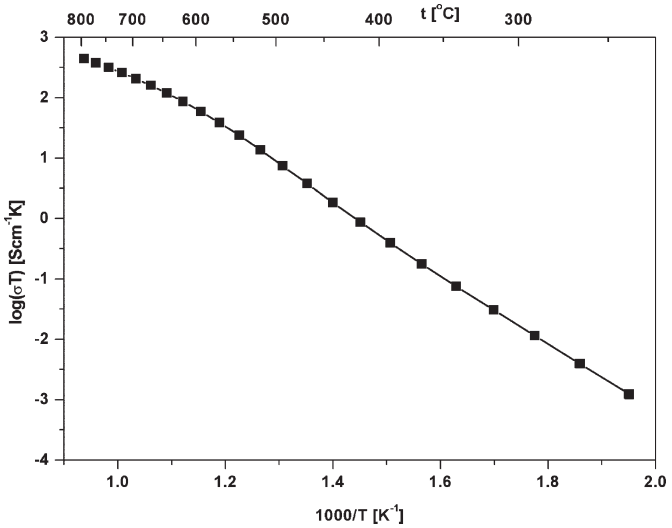

Figure 2. Arrhenius plot for total conductivity in Bi_3YO_6. Data corresponding to the second cooling cycle are shown.

conductivity data were fully reproducible on heating and cooling cycles, and those data corresponding to the second cooling cycle are shown. The plot can be interpreted as containing two linear regions: one at low temperature and one at high temperature, with a large transition region between *ca.* 425 °C and 650 °C. The activation energy in the high-temperature region ($\Delta E_{HT} = 0.67 \pm 0.02$ eV) is significantly lower than that at low temperatures ($\Delta E_{LT} = 1.19 \pm 0.01$ eV). Conductivities in the two regions characterized by the conductivity at 300 °C and 700 °C (σ_{300} and σ_{700}, respectively) are 3.7×10^{-5} S cm^{-1} and 2.7×10^{-1} S cm^{-1}, respectively, and confirm excellent conductivity for this phase, as previously reported.[33,50]

4.2. Average Structure of Bi_3YO_6. Figure 3 shows the diffraction profiles for Bi_3YO_6 at 25 and 800 °C, fitted using conventional Rietveld analysis, with the corresponding crystal and refinement parameters in Table 2. The refined structural parameters are summarized in Table 3, with significant contact distances given in Table 4. All Bragg peaks can be indexed on the $Fm\bar{3}m$ cubic cell and the absence of superlattice reflections confirms that there is no long-range ordering of either anions or cations at both the studied temperatures. On the crystallographic scale, the oxide ions are found to be distributed over three sites in the $Fm\bar{3}m$ cell, viz, the 8*c*, 32*f*, and 48*i* sites (O(1), O(2), and O(3), respectively). The fractional coordinates of the three oxide ion sites are in good agreement with those reported previously,[15,16] although the distribution of scattering between these sites varies somewhat. In addition, the average position for the cation site in the present study is found to lie very close to the ideal 4*a* site, rather than the slightly shifted 24*e* site refined in the previous studies. Only the 32*f* and 8*c* sites are found to be occupied in the parent compound δ-Bi_2O_3,[15,27,28,51−53] and it is therefore reasonable to suppose that oxide ions in the 48*i* site are exclusively associated with coordination to yttrium. Indeed, the location of the 48*i* site allows for a distorted octahedral coordination for the Y^{3+} cations (see Figure 4).

There is clear nonlinearity in the thermal variation of the cubic lattice parameter (see Figure 5), with the unit cell parameter being ~0.5% larger at 800 °C than would be expected from a simple linear expansion of the lattice. This is a common feature in substituted bismuth oxide-based fluorites.[7] There are no obvious changes in the diffraction patterns (Figure 3), which suggests that the observed nonlinear behavior may be associated with a subtle second-order transition. The thermal variation of the cation and anion isotropic thermal parameters is shown in Figure 6. The cation thermal parameter is closely correlated to the thermal expansion of the lattice parameter and is clearly dominated by thermal vibration. Similarly, the thermal variation of the anion thermal parameter reflects that of the cubic lattice parameter, but it is also significantly larger than that for the cations, because it describes significant disorder on the oxide ion sites, as well as thermal vibration.

At 800 °C, there is little significant change in the oxide ion distribution, compared to that at room temperature. Only the occupancy of the 48*i* site (O(3)) increases significantly (*ca.* 55%) at 800 °C, coupled with a 4% increase in the M−O(3) distance compared to modest rises of *ca.* 1% for M−O(2) and M−O(1) (Table 4). The increase in the 48*i* site occupancy appears to occur mainly at the expense of that of the 8*c* site (O(1)), although the value of the 8*c* site occupancy at 800 °C lies within two estimated standard deviations of the value at room temperature; therefore, the change cannot be regarded as

(50) Takahashi, T.; Iwahara, H. *Mater. Res. Bull.* **1978**, *13*, 1450.
(51) Gattow, G.; Schroeder, H. *Z. Anorg. Allg. Chem.* **1962**, *318*, 176.
(52) Hund, F. *Z. Anorg. Allg. Chem.* **1964**, *333*, 248.
(53) Harwig, H. A. *Z. Anorg. Allg. Chem.* **1978**, *444*, 151.

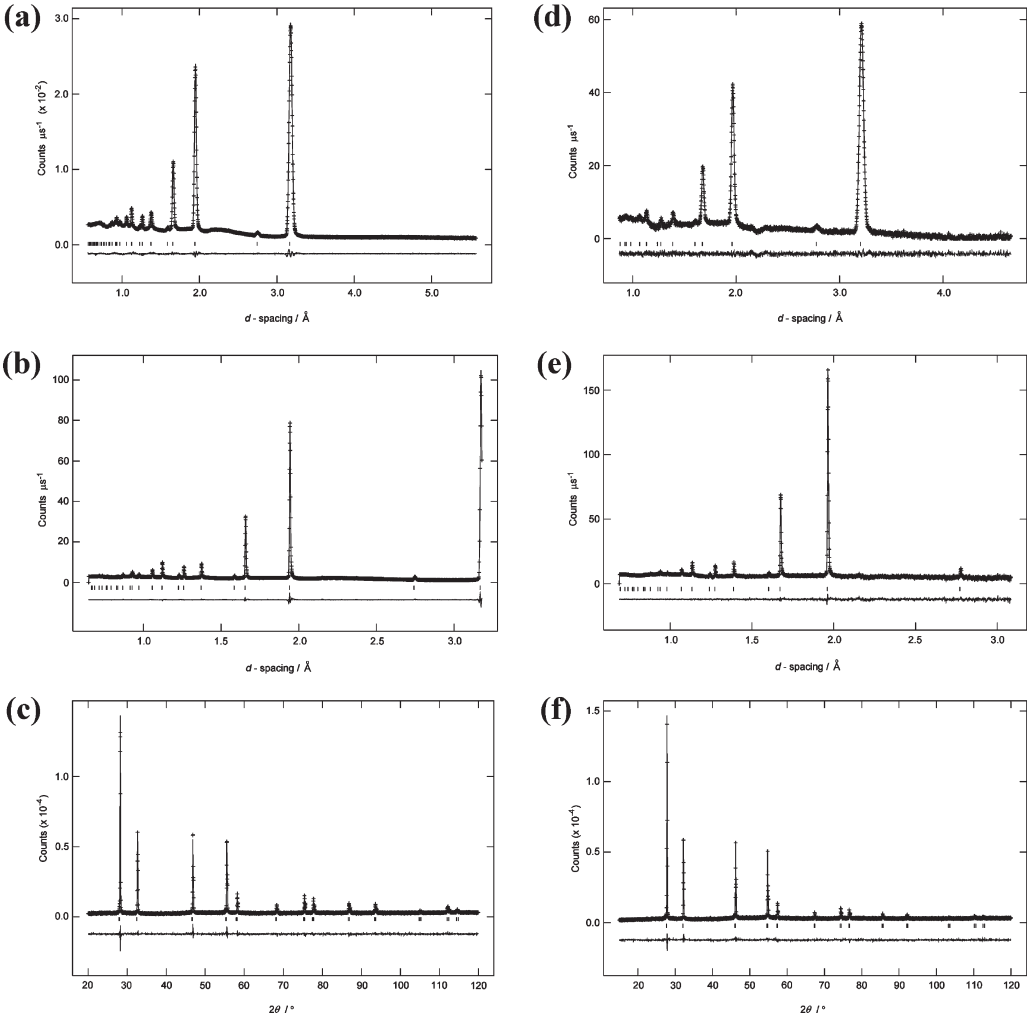

Figure 3. Diffraction profiles for Bi_3YO_6 at (a−c) 25 °C and (d−f) 800 °C, fitted using the Rietveld method. Observed (denoted by cross (+) symbols), calculated (denoted as a solid line), and difference (lower) profiles are shown with reflection positions indicated by markers. Neutron low-angle (panels (a) and (d)), neutron backscattering (panels (b) and (e)), and X-ray (panels (c) and (f)) data are shown.

significant. The observed change in 48*i* site occupancy may be used to explain the nonlinear thermal expansion of the cubic lattice parameter by considering ions on the site to be the interstitial of a Frenkel defect. As the occupancy of this site increases, one would expect an increase in the local distortion of the lattice, translating to a larger lattice parameter than that which would be expected from a simple thermal expansion. Although the increase in Frenkel defects must generate a higher vacancy concentration on the fluorite oxide ion sites (either 32*f* or 8*c*), these additional vacancies are effectively trapped in the yttrium coordination sphere; therefore, this increase in Frenkel defect concentration effectively reduces charge carrier concentration with a resultant reduction in conductivity.

4.3. Short-Range Structure. Bond valence sums from the RMC calculations yielded average valences for Bi, Y, and O of +3.08, +2.98, and −2.03 at room temperature and +2.99, +2.98, and −1.99 at 800 °C, respectively. Selected pair correlation functions for Bi_3YO_6 at 25 °C and at 800 °C are shown in Figure 7. Apart from the expected thermal shift, there is very little obvious difference between the individual pair correlations at the two studied temperatures.

Figure 8 shows the distribution of contact distances around bismuth and yttrium. Using the first minimum in the $g_{ij}(r)$ pair correlation function as a cutoff, the mode Bi−O and Y−O contact distances were found to be 2.456 Å and 2.425 Å at room temperature and 2.362 Å and 2.279 Å at 800 °C, respectively, yielding Bi−O and Y−O coordination numbers of 6.05 and 6.31 at 25 °C and 5.30 and 5.29 at 800 °C, respectively. The structural model resulting from the RMC calculations was analyzed to

Table 2. Crystal and Refinement Parameters for Long-Range Structure of Bi_3YO_6 at 25 and 800 °C

chemical formula	Bi_3YO_6	Bi_3YO_6
formula weight	811.84 g mol^{-1}	811.84 g mol^{-1}
temperature	25 °C	800 °C
crystal system	cubic	cubic
space group	$Fm\bar{3}m$	$Fm\bar{3}m$
unit cell dimension	a = 5.49458(9) Å	a = 5.55982(7) Å
volume	165.884(8) $Å^3$	171.863(7) $Å^3$
Z	1	1
density (calculated)	8.127 Mg cm^{-3}	7.844 Mg cm^{-3}
sample description	yellow powder	yellow powder
R-factors[a]		
(a) X-ray		
R_p	0.0573	0.0584
R_{wp}	0.0754	0.0738
R_{ex}^2	0.0462	0.0536
R_F^2	0.0841	0.0991
(b) Neutron backscattering		
R_p	0.0183	0.0425
R_{wp}	0.0152	0.0227
R_{ex}^2	0.0039	0.0241
R_F^2	0.1509	0.0462
(c) Neutron low angle		
R_p	0.0189	0.0571
R_{wp}	0.0241	0.0423
R_{ex}^2	0.0112	0.0515
R_F^2	0.1218	0.0279
total number of variables	118	118
number of profile points used		
X-ray	2990	3134
neutron backscattering	3302	2996
neutron low angle	4082	3261

[a] For definitions of the R-factors, see ref 32.

Table 3. Refined Parameters for Long-Range Structure of Bi_3YO_6 at (a) 25 and (b) 800 °C

(a) @ 25 °C

atom	site	x	y	z	Occ	U_{iso} ($Å^2$)
Bi	4*a*	0.0	0.0	0.0	0.75	0.0436(1)
Y	4*a*	0.0	0.0	0.0	0.25	0.0436(1)
O(1)	8*c*	0.25	0.25	0.25	0.391(5)	0.0606(4)
O(2)	32*f*	0.3076(6)	0.3076(6)	0.3076(6)	0.074(1)	0.0606(4)
O(3)	48*i*	0.5	0.1920(12)	0.1920(12)	0.011(1)	0.0606(4)

(b) @ 800 °C

atom	site	x	y	z	Occ	U_{iso} ($Å^2$)
Bi	4*a*	0.0	0.0	0.0	0.75	0.0687(3)
Y	4*a*	0.0	0.0	0.0	0.25	0.0687(3)
O(1)	8*c*	0.25	0.25	0.25	0.388(27)	0.080(2)
O(2)	32*f*	0.3089(23)	0.3089(23)	0.3089(23)	0.073(5)	0.080(2)
O(3)	48*i*	0.5	0.1656(13)	0.1656(13)	0.017(1)	0.080(2)

Table 4. Significant Contact Distances in Bi_3YO_6 at 25 and 800 °C

	Contact Distance (Å)	
bond	25 °C	800 °C
Bi/Y−O(1)	2.37922(3)	2.40747(3)
Bi/Y−O(2)	2.2565(6)	2.282(2)
Bi/Y−O(3)	1.994(2)	2.075(4)

determine further details of local coordination environments. M−O bond distances were evaluated based on the sum of the ionic radii (with radii of 1.17, 1.089, and 1.38 Å for Bi^{3+}, Y^{3+}, and O^{2-}, respectively[54]). This approach allows for the exclusion of nonbonded interactions, particularly in the case of coordination to Bi, where the nonbonding $6s^2$ pair of electrons result in stereochemically distorted environments around Bi. Figure 9 shows a plot of the averages of the first eight contacts around bismuth and yttrium at the two studied temperatures. The plots are clearly sigmoidal in character, and the point of inflection corresponds to the change between bonding and nominally nonbonding interactions. This change is seen to occur between the fourth and fifth contacts for bismuth and at the fifth contact for yttrium at both temperatures, corresponding to Bi−O distances of 2.59 and 2.60 Å at room temperature and 800 °C, respectively, and 2.60 and 2.64 Å for Y−O at these two temperatures, respectively. The values for Bi−O are close to the sum of the respective ionic radii; however, the values for Y−O are considerably larger (2.55 Å for Bi−O and 2.40 Å for Y−O), indicating significant distortion of the Y−O polyhedra. Using these values as the maximum bond length criteria, the resulting mean bond lengths were found to be 2.261 and 2.212 Å at 25 °C and 2.268 and 2.219 Å at 800 °C for Bi−O and Y−O, respectively. The average coordination numbers, using these bonding criteria, were determined to be 4.28 and 4.66 at 25 °C and 4.38 and 4.74 at 800 °C for bismuth and yttrium, respectively.

In the case of bismuth, these values are consistent with stereochemical activity of the $6s^2$ electrons resulting in lower coordination geometries, while the values for yttrium are lower than expected. This is almost certainly due to the relatively poor neutron scattering contrast between yttrium and bismuth, with the higher coordination number of yttrium resulting from the bond-valence constraints rather than discernible differences in the scattering data. Interestingly, ^{89}Y NMR studies on this compound,[55] show a single broad resonance characteristic of a wide range of environments for Y.

There is little difference between the room temperature and 800 °C results other than an increase in the average bond lengths and a small increase in the coordination numbers. This suggests that the overall structure is relatively unchanged.

The average O−M site coordination number is 3.991 at room temperature and 3.628 at 800 °C, using the first minimum in the $g_{ij}(r)$ pair correlation function as a cutoff. These values are slightly lower than the ideal fluorite value of 4 and reflect the fact that a significant number of oxide ions are displaced into positions corresponding to the 48*i* site (O(3)) in the crystallographic model. The lower value at 800 °C is in agreement with the average structure refinements, which showed a significant increase in the occupancy of the 48*i* site. Using the maximum bond length criteria described above, the average O−M coordination numbers drop to 3.26 and 3.29 at 25 and 800 °C, respectively. These values now reflect more accurately the crystallographic model, which shows

(54) Shannon, R. D. *Acta Crystallogr., Sect. A: Cryst., Phys., Diffr., Theor. Gen. Crystallogr.* **1976**, *A32*, 751.

(55) Battle, P. D.; Montez, B.; Oldfield, E. *J. Chem. Soc. Chem. Commun.* **1988**, 584.

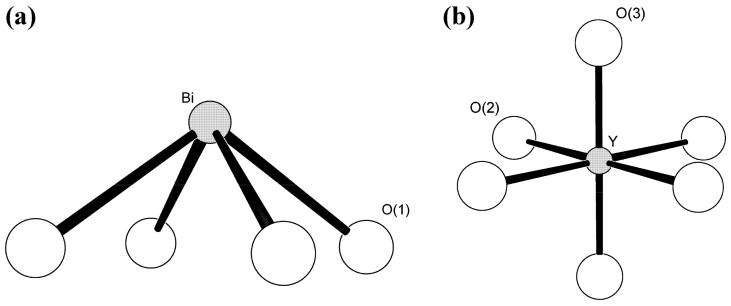

Figure 4. Proposed coordination geometries around (a) Bi and (b) Y in Bi_3YO_6, based on the average structure at 25 °C.

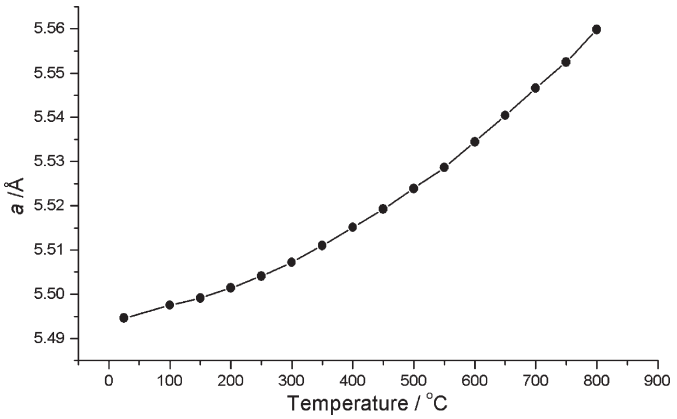

Figure 5. Thermal variation of cubic lattice parameter (a) in Bi_3YO_6. Estimated standard deviations are smaller than the symbols.

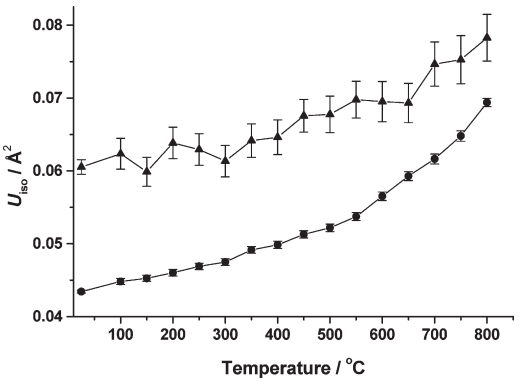

Figure 6. Thermal variation of (●) cation and (▲) anion isotropic thermal parameters in Bi_3YO_6. Error bars correspond to $\pm 2\sigma$ (where σ is the estimated standard deviation).

significant occupancy of the 32*f* site (O(2)). Oxygen atoms on this site are bonded to three metal atoms only.

The O−M−O angular distribution functions (ADFs) for Bi_3YO_6 at room temperature and at 800 °C are shown in Figure 10. Three maxima are observed, which can be explained by considering the cation coordination in the ideal fluorite structure (see Figure 11a). If one considers the cubic coordination around a single cation in the fluorite structure, there are three different O−M−O angles of 70°, 109°, and 180°. The relative numbers of each of these angles are in the ratio 6:6:2 and correspond to O−M−O angles between pairs of O atoms located on an edge, face, and body diagonal, respectively. In δ-Bi_2O_3, 1/4 of the oxide ion sites are vacant, which means the average bismuth coordination number is 6 in the ideal model, i.e., each Bi atom has two oxide ion vacancies in its coordination environment. As described above, the ordering of these vacancies has been the subject of much research with conflicting results.[19−25] The vacancies can be aligned randomly, in which case the ideal 6:6:2 ratio would be unaffected, or be aligned in ⟨111⟩-, ⟨100⟩-, or ⟨110⟩-directions, resulting in various ratios. Figure 11 summarizes the predicted angular distribution ratios for different vacancy ordering models in δ-Bi_2O_3.

The situation in δ-Bi_3YO_6 is somewhat different, because there is finite occupancy of the 48*i* site (O(3)) and a significant occupation of the 32*f* site (O(2)), which means that the system is far from the ideal case. If one considers the oxide ions located on the 48*i* site to be Frenkel interstitials, then the number of vacancies in the fluorite anion site (considered to be a combination of 8*c* and 32*f* sites) is closer to three vacancies around each metal atom. Again, several models can be proposed to describe the distribution of three vacancies (Figure 12).

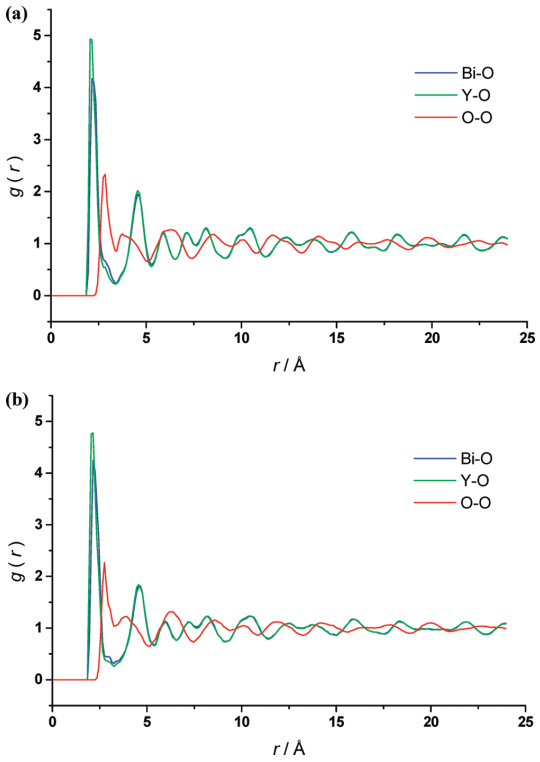

Figure 7. Selected pair correlation functions $g_{ij}(r)$ for Bi_3YO_6 at (a) 25 and (b) 800 °C.

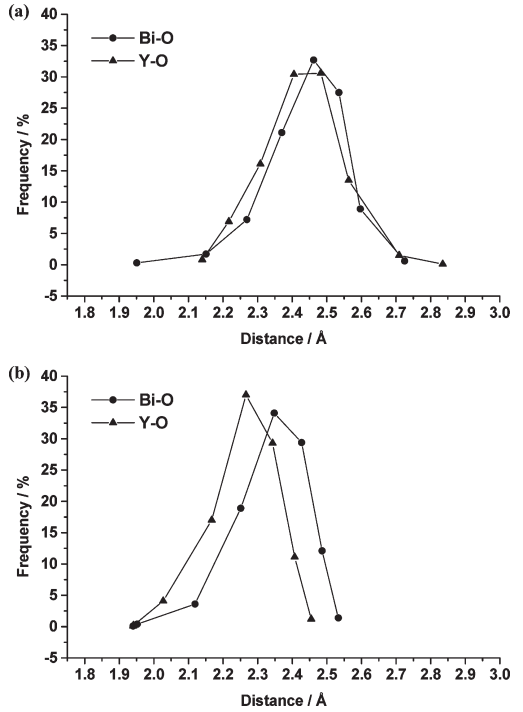

Figure 8. Contact distance distribution in Bi_3YO_6 at (a) 25 and (b) 800 °C.

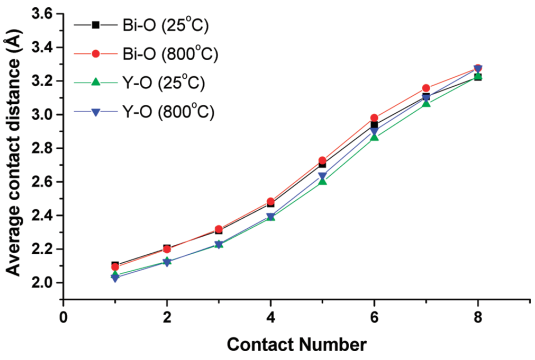

Figure 9. Average contact distances for the first eight contacts around the metal cations in Bi_3YO_6.

The peak positions of the O−M−O ADFs (Figure 10) represent the average angles over the peak ranges. The integrals of the functions over the angles from 0° to 180° give the angle ratio in each model, as summarized in Table 5. The observed values at room temperature clearly appear to be consistent with a predominantly ⟨110⟩ (or ⟨110⟩⟨011⟩) distribution of 2−3 vacancies around each metal atom. The 800 °C data show a significant increase in the middle angle, with respect to the other two angles. This is consistent with the observed increase in the 48*i* occupancy at this temperature. Again, the data are consistent with predominantly ⟨110⟩ ordering of vacancies.

4.4. Energy Minimization and Defect Simulations. As noted, large supercells of composition Bi_3YO_6 were examined by atomistic simulation methods to complement the structural studies. Energy minimization (structural optimization) of the oxygen vacancy ordering configurations shown in Figure 11 was carried out.

Comparison of the lattice energies of the ordering models listed in Table 6 reveals that ⟨111⟩ ordering is the least stable, with the ⟨110⟩ configuration slightly lower in energy than the ⟨100⟩ configuration and the disordered state. This is consistent with the structural analysis, indicating evidence for ⟨110⟩ vacancy ordering in δ-Bi_3YO_6. It is worth noting that previous *ab initio* studies of similar intrinsic oxygen vacancy ordering in pure δ-Bi_2O_3 found that ⟨111⟩ ordering was least favorable and ⟨100⟩ ordering was only 0.06 eV more stable than that of ⟨110⟩ ordering.[24] Furthermore, a more intensive molecular dynamics and *ab initio* study of pure δ-Bi_2O_3 by Aidhy et al.[25] found similar results, but also included an ordered 2 × 2 × 2 supercell, suggested by Boyapati et al.,[56] that contained a combination of ⟨111⟩ and ⟨110⟩ vacancy ordering.

The calculated unit cell parameters for Bi_3YO_6 for the different ordering models shown in Figure 11 are also

(56) Boyapati, S.; Wachsman, E. D.; Jiang, N. *Solid State Ionics* **2001**, *140*, 149.

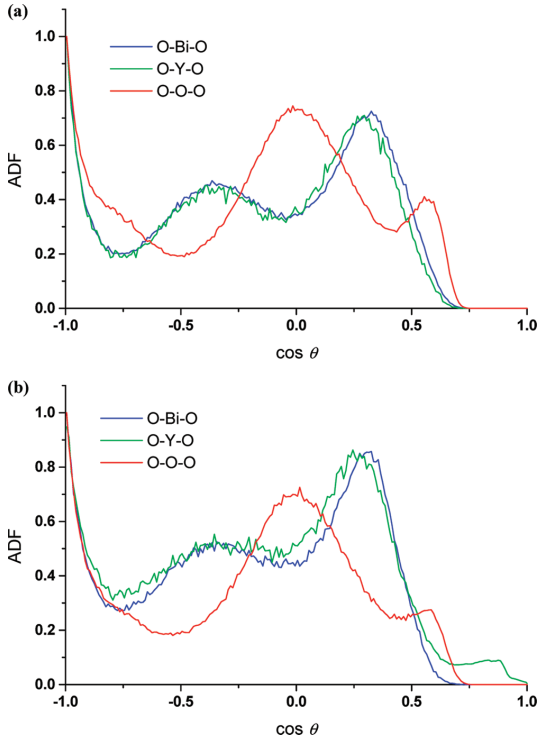

Figure 10. O−M−O angular distribution functions for Bi_3YO_6 at (a) 25 and (b) 800 °C.

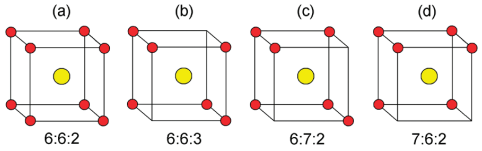

Figure 11. Models for oxide ion vacancy ordering in the idealized structure of δ-Bi_2O_3, showing (a) ideal fluorite, (b) ⟨111⟩, (c) ⟨110⟩, and (d) ⟨100⟩ ordering. Angle ratios for 70°, 109°, and 180° angles are given. Bi and O are indicated by large yellow and small red circles, respectively.

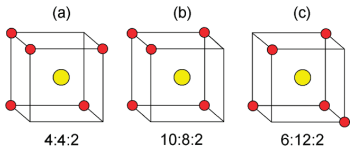

Figure 12. Models for oxide ion vacancy ordering of three vacancies in the idealized structure of δ-Bi_3YO_6, showing (a) ⟨111⟩ ⟨110⟩ ⟨100⟩, (b) ⟨100⟩ ⟨110⟩, and (c) ⟨110⟩⟨101⟩ ordering. Angle ratios for 70°, 109°, and 180° angles are given. Bi/Y and O are indicated by large yellow and small red circles, respectively.

listed in Table 6 and compared to the experimentally observed values. Interestingly, small differences in unit cell volume are observed for the different vacancy ordering configurations, with the ⟨110⟩ configuration yielding the largest unit cell volume of the ordered states, but still significantly lower than that for the disordered state.

Table 5. O−M−O Angle Ratios Derived from RMC Model of Bi_3YO_6

@ 25 °C		@ 800 °C	
angle (deg)	ratio	angle (deg)	ratio
71.44	6.0	72.78	5.0
107.99	8.0	106.28	9.1
180	2.0	180	2.0

Table 6. Calculated Lattice Energies and Calculated and Experimental Lattice Parameters for Different Vacancy Ordering Models in Bi_3YO_6

parameter	expt	Calc. ⟨100⟩	Calc. ⟨110⟩	Calc. ⟨111⟩	Calc. disordered
U_{latt} (eV)		−275.51	−275.71	−270.45	−275.49
volume (Å^3)	165.88	158.90	160.31	159.89	165.39
a (Å)	5.495	5.375	5.331	5.430	5.479
b (Å)	5.495	5.508	5.643	5.430	5.483
c (Å)	5.495	5.375	5.331	5.430	5.505
β (deg)	90.0	86.9	88.8	88.2	89.8

A significant feature of these supercell calculations is the observed relaxation of the O atoms from starting points equivalent to the 8*c* lattice position in the $Fm\bar{3}m$ subcell, to positions equivalent to the 32*f* site in the cubic subcell. The average deviation from the 8*c* lattice site was 0.47 Å. Therefore, the modeling work reproduces a structural feature observed in the experimental studies that was not incorporated into the input simulation structure and provides a valid starting point for the defect calculations.

The energies of isolated point defects (vacancies and interstitials) were calculated, with the possibility of oxygen vacancies on the various sites, as well as several possible interstitial sites. The most favorable interstitial site for oxide ions was found to be on the "intrinsic vacancy" sites at 8*c*. The 48*i* site was also considered for interstitial ions; however, the mean energy value was observed to be less favorable, by more than 1 eV. The total energies for Frenkel and Schottky-type disorder for the various species were then derived by combining the individual defect energies and the appropriate lattice energies according to the following reaction equations:

Oxygen Frenkel disorder:

$$O_O^{\times} \rightarrow V_O^{\bullet\bullet} + O_i'' \quad (3)$$

Bismuth Frenkel disorder:

$$Bi_{Bi}^{\times} \rightarrow V_{Bi}''' + Bi_i^{\bullet\bullet\bullet} \quad (4)$$

Bi_3YO_6 full Schottky disorder:

$$3Bi_{Bi}^{\times} + Y_Y^{\times} + 6O_O^{\times} \rightarrow 3V_{Bi}''' + V_Y''' + 6V_O^{\bullet\bullet} + Bi_3YO_6 \quad (5)$$

Bi_2O_3 partial Schottky disorder:

$$2Bi_{Bi}^{\times} + 3O_O^{\times} \rightarrow 2V_{Bi}''' + 3V_O^{\bullet\bullet} + Bi_2O_3 \quad (6)$$

Y_2O_3 partial Schottky disorder:

$$2Y_Y^{\times} + 3O_O^{\times} \rightarrow 2V_Y''' + 3V_O^{\bullet\bullet} + Y_2O_3 \quad (7)$$

The resulting defect formation energies are given in Table 7 and indicate two main features. First, the results

Table 7. Calculated Energies of Intrinsic Defects in Bi_3YO_6

defect	equation	defect energy (eV)
O Frenkel (8*c*)	3	0.54
O Frenkel (48*i*)	3	1.91
Bi Frenkel	4	25.93
Bi_3YO_6 Schottky	5	15.93
Bi_2O_3 partial Schottky	6	10.56
Y_2O_3 partial Schottky	7	11.60

suggest that cation Frenkel and all the Schottky-type defects are highly unlikely, which agrees well with experiment. Second, oxygen Frenkel disorder is clearly the most favorable intrinsic defect. This is consistent with our structural analysis, as well as a highly mobile oxygen sublattice in the Bi_3YO_6 system at higher temperatures.

5. Conclusions

The combination of a total scattering analysis and computer simulation is extremely powerful and appears to yield a more realistic description of the defect structure in disordered systems, which can be used to explain observed physical behavior. The analysis reveals detail of the local coordination environments around the cations, which is consistent with stereochemical activity of the Bi $6s^2$ nonbonding pair of electrons. The relatively poor neutron scattering contrast between Y and Bi results in difficulty in separating the scattering contributions of these atoms. The main advantage of this form of analysis over conventional Rietveld refinement appears to be the information on short-range ordering of vacancies.

Analysis of the angular distribution functions for Bi_3YO_6 shows, for the first time, physical evidence for predominantly ⟨110⟩ vacancy ordering in a bismuth oxide-based fluorite. Changes in the oxide ion distribution, which are a result of an increase in oxygen Frenkel defects, appear to be correlated to nonlinear behavior in the thermal expansion of the cubic lattice parameter, as well as Arrhenius plots of conductivity. A new interatomic potential model for Bi_3YO_6 has been developed in which the lowest energy vacancy-ordering model is found to be the ⟨110⟩ configuration. Defect calculations show that oxygen Frenkel disorder is the lowest energy intrinsic disorder, which is consistent with a highly mobile oxygen sublattice.

Acknowledgment. We gratefully acknowledge the Science and Technology Facilities Council (STFC) for a CMPC studentship grant to X.L. The authors thank the ISIS Facility for neutron beam time and Dr. R.M. Wilson for his help in X-ray data collection. M.S.I. and S.J.S. thank the Engineering and Physical Sciences Research Council (EPSRC) for their funding (EP/D077745/1) and Prof C. Greaves for useful discussions. S.T.N. wishes to thank Vetenskapsrådet (the Swedish Research Council) for financial support.

Appendix E

Interatomic Potentials

Table E.1: Interatomic potentials

$M\cdots O^{2-}$	A	ρ	C	Y	k	ref
Li^{+}	632.10	0.2906	0	1.00	99999	
Na^{+}	1677.83	0.2934	0	1.00	99999	[229]
Ba^{2+}	931.70	0.3949	0	1.46	14.78	[160]
Ca^{2+}	1228.90	0.3372	0	1.26	34	[160]
Mg^{2+}	821.60	0.3242	0	2.00	99999	[160]
Pb^{2+}	72276.42	0.2223	0	-4.00	172.7	[230]
Co^{2+}	696.30	0.3362	0.0	2.00	99999	[160]
Mn^{2+}	715.80	0.3464	0.0	3.00	81.2	[160]
Ni^{2+}	683.50	0.3332	0.0	2.00	8.77	[231]
Sr^{2+}	1400.00	0.3500	0	1.33	21.53	[160]
Ti^{2+}	633.30	0.3372	0.0	2.00	99999	[160]
Ga^{3+}	2901.12	0.2742	0	3.00	99999	[46]
Gd^{3+}	1336.80	0.3551	0	3.00	99999	[228]
La^{3+}	1545.21	0.3590	0	-0.25	145	[46]
Nd^{3+}	1379.90	0.3601	0	3.00	99999	[228]
Sc^{3+}	1299.40	0.3312	0	3.00	99999	[228]
Yb^{3+}	1309.60	0.3462	0	3.00	99999	[228]
Y^{3+}	1345.1	0.3491	0	3.000	99999	[228]
In^{3+}	1495.6	0.3310	4.33	-6.100	1680	[232]
Mn^{3+}	1267.50	0.3214	0.0	3.00	95	[56]
Ti^{4+}	877.20	0.3810	9.0	-35.86	95	[233]
Nb^{5+}	1796.30	0.3460	0.0	-4.50	1358.58	[234]
Ta^{5+}	1315.57	0.3691	0.0	-4.60	5916.77	[235]

Table E.2: Candidate potential sets used in the $Bi_{28}Re_2O_{49}$ study

Interaction	A/eV	ρ/Å	C/eV Å^6	Y/e	k/eV Å^{-2}
Constant Potentials					
Bi^{3+}	49529.35	0.22	0.00	-5.51	359.55
$Bi^{3+}\cdots Bi^{3+}$	24244.5	0.33	0.00	-	-
Potential Set (1)					
$Re^{7+}\cdots O^{2-}$	1023.16	0.4383	0.00	-	-
$Re^{7+}\cdots Re^{7+}$	0.000968	0.3284	0.00	-	-
$O^{2-}\cdots O^{2-}$	22764.3	0.149	27.88	-2.86	74.92
Potential Set (2)					
$Re^{7+}\cdots O^{2-}$	1023.16	0.4383	0.00	-	-
$Re^{7+}\cdots Re^{7+}$	0.000968	0.3284	0.00	-	-
$O^{2-}\cdots O^{2-}$	15123.6	0.223	28.43	-2.47	23.09
Potential Set (3)					
$Re^{7+}\cdots O^{2-}$	3275.29	0.35	0.00	-	-
$O^{2-}\cdots O^{2-}$	22764.3	0.149	27.88	-2.86	74.92
Potential Set (4)					
$Re^{7+}\cdots O^{2-}$	12268.18	0.241751	0.00	-	-
$Re^{7+}\cdots Re^{7+}$	0.000968	0.3284	0.00	-	-
$O^{2-}\cdots O^{2-}$	22764.3	0.149	27.88	-2.86	74.92

References

[1] J. Houghton, ed., *Climate change 2001: The scientific basis* (Cambridge University Press, 2001).

[2] M. Winter, R. J. Brodd, *Chem. Rev.* **104**, 4245 (2004).

[3] B. C. H. Steele, A. Heinzel, *Nature* **414**, 345 (2001).

[4] J. B. Goodenough, *Annu. Rev. Mater. Res.* **33**, 91 (2003).

[5] S. M. Haile, *Acta Mater.* **51**, 5981 (2003).

[6] D. J. L. Brett, A. Atkinson, N. P. Brandon, S. J. Skinner, *Chem. Soc. Rev.* **37**, 1568 (2008).

[7] A. Orera, P. R. Slater, *Chem. Mater.* **22**, 675 (2010).

[8] A. J. Jacobson, *Chem. Mater.* **22**, 660 (2010).

[9] J. A. Kilner, *Faraday Discussions* **134**, 9 (2007).

[10] V. V. Kharton, F. M. B. Marques, A. Atkinson, *Solid State Ionics* **174**, 135 (2004).

[11] H. L. Tuller, *Phys. Chem. Chem. Phys.* **11**, 3023 (2009).

[12] N. Q. Minh, *Solid State Ionics* **174**, 271 (2004).

[13] J. W. Fergus, *J. Power Sources* **162**, 30 (2006).

[14] O. H. Kwon, G. M. Choi, *Solid State Ionics* **177**, 3057 (2006).

[15] K. D. Kreuer, *J. Memb. Science* **185**, 29 (2001).

[16] L. Malavasi, C. A. J. Fisher, M. S. Islam, *Chem. Soc. Rev.* **in press** (2010).

[17] H. Iwahara, T. Esaka, H. Uchida, N. Maeda, *Solid State Ionics* **3-4**, 359 (1981).

[18] K. Kitazawa, R. L. Coble, *J. Am. Cer. Soc.* **57**, 360 (1974).

[19] L. D. Burke, H. Rickert, R. Steiner, *Z. Phys. Chem.* **74**, 146 (1971).

[20] T. Kawada, J. Mizusaki, *Handbook of Fuel Cells - Fundamentals, Technology and Applications*, vol. 4 (John Wiley & Sons, New Jersey, USA, 2003).

[21] S. Q. Hui, J. Roller, S. Yick, X. Zhang, C. Deces-Petit, Y. S. Xie, R. Maric, D. Ghosh, *J. Power Sources* **172**, 493 (2007).

[22] X. Guo, R. Waser, *Prog. Mater. Sci.* **51**, 151 (2006).

[23] T. I. Politova, J. T. S. Irvine, *Solid State Ionics* **168**, 153 (2004).

[24] T. Norby, *Solid State Ionics* **125**, 1 (1999).

[25] K. D. Kreuer, *Annu. Rev. Mater. Res.* **33**, 333 (2003).

[26] B. C. H. Steele, *Solid State Ionics* **134**, 3 (2000).

[27] A. Lashtabeg, S. J. Skinner, *J. Mater. Chem.* **16**, 3161 (2006).

[28] O. Yamamoto, Y. Takeda, R. Kanno, M. Noda, *Solid State Ionics* **22**, 241 (1987).

[29] J. Juo, H. U. Anderson, D. M. Sparlin, *J. Solid State Chem.* **83**, 52 (1989).

[30] S. C. Singhai, *Solid State Ionics* **135**, 305 (2000).

[31] S. J. Skinner, *Int. J. Inorg. Mater.* **3**, 113 (2001).

[32] T. Setoguchi, K. Okamoto, K. Eguchi, H. Arai, *J. Solid State Chem.* **139**, 2875 (1992).

[33] J. W. Fergus, *Solid State Ionics* **171**, 1 (2004).

[34] H. G. Scott, *J. Mater. Sci.* **10**, 1527 (1975).

[35] A. W. Smith, F. W. Meszaros, C. D. Kamata, *J. Am. Cer. Soc.* **57**, 360 (1974).

[36] K. Momma, F. Izumi, *J. Appl. Crystallogr.* **41**, 653 (2008).

[37] M. Filal, C. Petot, M. Mokchah, C. Chateau, J. L. Carpentier, *Solid State Ionics* **80**, 27 (1995).

[38] V. Butler, C. R. A. Catlow, B. E. F. Fender, *Solid State Ionics* **8**, 109 (1983).

[39] L. Minervini, M. O. Zacate, R. W. Grimes, *Solid State Ionics* **116**, 339 (1999).

[40] J. A. Kilner, *Solid State Ionics* **129**, 13 (2000).

[41] S. Omar, E. D. Wachsman, J. L. Jones, J. C. Nino, *J. Am. Cer. Soc.* **92**, 2674 (2009).

[42] T. Ishihara, H. Matsuda, Y. Takata, *J. Am. Cer. Soc.* **116**, 3801 (1994).

[43] M. Feng, J. B. Goodenough, *Eur. J. Solid State Inorg. Chem.* **31**, 663 (1994).

[44] H. Iwahara, H. Uchida, K. Ono, K. Ogaki, *J. Electrochem. Soc.* **135**, 529 (1988).

[45] H. Iwahara, *Solid State Ionics* **28-30**, 573 (1988).

[46] M. S. Khan, M. S. Islam, D. R. Bates, *J. Phys. Chem. B* **102**, 3099 (1998).

[47] M. Yashima, K. Nomura, H. Kageyama, Y. Miyazaki, N. Chitose, K. Adachi, *Chem. Phys. Lett.* **380**, 391 (2003).

[48] C. R. A. Catlow, *Solid State Chemistry: Techniques* (Clarendon Press, Oxford, 1987).

[49] C. R. A. Catlow, G. D. Price, *Nature* **347**, 243 (1990).

[50] C. R. A. Catlow, R. G. Bell, J. D. Gale, *J. Mater. Chem.* **4**, 781 (1994).

[51] M. S. Islam, L. J. Winch, *Phys. Rev. B* **52**, 10510 (1995).

[52] M. S. Islam, M. S. D. Read, S. D'Arco, *Faraday Discussions* p. 367 (1997).

[53] M. S. Islam, D. J. Ilett, S. C. Parker, *J. Phys. Chem.* **98**, 9637 (1994).

[54] T. X. T. Sayle, S. C. Parker, C. R. A. Catlow, *Surf. Sci.* **316**, 329 (1994).

[55] T. S. Bush, C. R. A. Catlow, A. V. Chadwick, M. Cole, R. M. Geatches, G. N. Greaves, S. M. Tomlinson, *J. Mater. Chem.* **2**, 309 (1992).

[56] M. Cherry, M. S. Islam, C. R. A. Catlow, *J. Solid State Chem.* **118**, 125 (1995).

[57] R. A. Davies, M. S. Islam, A. V. Chadwick, G. E. Rush, *Solid State Ionics* **130**, 115 (2000).

[58] E. Kendrick, J. Kendrick, K. S. Knight, M. S. Islam, P. R. Slater, *Nature Mater.* **6**, 871 (2007).

[59] J. D. Gale, *Faraday Trans.* **93**, 629 (1997).

[60] B. Slater, J. O. Titiloye, F. M. Higgins, S. C. Parker, *Curr. Opin. Solid State Mater. Sci.* **5**, 417 (2001).

[61] M. S. Islam, D. J. Driscoll, C. A. J. Fisher, P. R. Slater, *Chem. Mater.* **17**, 5085 (2005).

[62] P. P. Ewald, *Ann. Physik.* **64**, 253 (1921).

[63] M. P. Tosi, *Solid State Phys.* **16**, 1 (1964).

[64] A. R. Leach, *Molecular modelling : principles and applications* (Harlow : Longman, 1996).

[65] B. Dick, A. Overhauser, *Phys. Rev.* **112**, 90 (1958).

[66] R. G. Gordon, Y. S. Kim, *J. Chem. Phys.* **56**, 3122 (1972).

[67] P. T. Wedepohl, *Proc. Phys. Soc.* **92**, 79 (1967).

[68] B. C. H. Steele, *High Conductivity Solid Ionic Conductors* (World Scientific: Singapore, 1989).

[69] M. Godickemeier, K. Sasaki, L. J. Gauckler, *J. Electrochem. Soc.* **144**, 1635 (1997).

[70] T. Takahashi, H. Iwahara, Y. Nagai, *J. Applied Electrochem.* **2**, 97 (1972).

[71] T. Takahashi, H. Iwahara, *Mater. Res. Bull.* **13**, 1447 (1978).

[72] J. C. Boivin, G. Mairesse, *Chem. Mater.* **10**, 2870 (1998).

[73] P. Shuk, H. D. Wiemhofer, U. Guth, W. Gopel, M. Greenblatt, *Solid State Ionics* **89**, 179 (1996).

[74] N. M. Sammes, G. A. Tompsett, H. Näfe, F. Aldinger, *J. Eur. Cer. Soc.* **19**, 1801 (1999).

[75] R. Punn, A. M. Feteira, D. C. Sinclair, C. Greaves, *J. Am. Chem. Soc.* **128**, 15386 (2006).

[76] G. Gattow, H. Schroder, *Z. Anorg. Allg. Chem.* **318**, 176 (1962).

[77] C. N. R. Rao, G. V. Subba Rao, S. Ramdas, *J. Phys. Chem.* **73**, 672 (1963).

[78] L. G. Sillen, *Ark. Kemi. Mineral. Geol.* **12A**, 1 (1937).

[79] B. T. M. Willis, *Acta Crys.* **18**, 75 (1965).

[80] P. D. Battle, C. R. A. Catlow, J. W. Heap, L. M. Moroney, *J. Solid State Chem.* **63**, 8 (1986).

[81] M. Yashima, D. Ishimura, *Chem. Phys. Lett.* **378**, 395 (2003).

[82] T. Takahashi, H. Iwahara, T. Arao, *J. Applied Electrochem.* **5**, 187 (1975).

[83] P. D. Battle, C. R. A. Catlow, A. V. Chadwick, P. Cox, G. N. Greaves, L. M. Moroney, *J. Solid State Chem.* **69**, 230 (1987).

[84] M. Verkerk, A. J. Burggraaf, *J. Electrochem. Soc.* **128**, 75 (1981).

[85] G. Meng, C. Chen, X. Han, P. Yang, D. Peng, *Solid State Ionics* **28-30**, 533 (1988).

[86] A. V. Chadwick, A. J. Francklin, *Phil. Mag. A* **68**, 787 (1993).

[87] A. J. Francklin, A. V. Chadwick, J. W. Couves, *Solid State Ionics* **70**, 215 (1994).

[88] N. Portefaix, P. Conflant, J. C. Boivin, J. P. Wignacourt, M. Drache, *J. Solid State Chem.* **134**, 219 (1997).

[89] R. Datta, J. Meehan, *Z. Anorg. Allgem. Chem.* **383**, 328 (1971).

[90] P. D. Battle, C. R. A. Catlow, J. Drennan, A. D. Murray, *J. Phys. C* **16**, 561 (1983).

[91] I. Abrahams, A. Kozanecka-Szmigiel, F. Krok, W. Wrobel, S. Chan, J. Dygas, *Solid State Ionics* **177**, 1761 (2006).

[92] I. Abrahams, X. Liu, S. Hull, S. T. Norberg, F. Krok, A. Kozanecka-Szmigiel, M. S. Islam, S. J. Stokes, *Chem. Mater.* **22**, 4435 (2010).

[93] P. W. M. Jacobs, D. A. Macdonaill, *Solid State Ionics* **23**, 279 (1987).

[94] P. W. M. Jacobs, D. A. Macdonaill, *Solid State Ionics* **23**, 295 (1987).

[95] P. W. M. Jacobs, D. A. Macdonaill, *Solid State Ionics* **23**, 307 (1987).

[96] N. Medvedeva, V. Zhukov, V. Gubanov, D. Novikov, M. Klein, *J. Phys. Chem. Solids* **57**, 1243 (1996).

[97] A. Walsh, G. Watson, D. Payne, R. Edgell, J. Guo, P. Glans, T. Learmonth, K. Smith, *Phys. Rev. B* **73** (2006).

[98] D. S. Aidhy, J. C. Nino, S. B. Sinnott, E. D. Wachsman, S. R. Phillpot, *J. Am. Cer. Soc.* **91**, 2349 (2008).

[99] C. E. Mohn, S. Stolen, S. T. Norberg, S. Hull, *Phys. Rev. Lett.* **102**, 155502 (2009).

[100] S. Hull, S. T. Norberg, M. G. Tucker, S. G. Eriksson, C. E. Mohn, S. Stolen, *Dalton Trans.* p. 8737 (2009).

[101] M. S. Islam, S. Lazure, R. N. Vannier, G. Nowogrocki, G. Mairesse, *J. Mater. Chem.* **8**, 655 (1998).

[102] T. S. Bush, J. D. Gale, C. R. A. Catlow, P. D. Battle, *J. Mater. Chem.* **4**, 831 (1994).

[103] R. W. Grimes, G. Busker, M. A. McCoy, A. Chroneos, J. A. Kilner, S. P. Chen, *Phys. Chem. Chem. Phys.* **101**, 1204 (1997).

[104] M. S. Islam, P. R. Slater, J. R. Tolchard, T. Dinges, *Dalton Trans.* p. 3061 (2004).

[105] A. Snedden, P. Lightfoot, T. Dinges, M. S. Islam, *J. Solid State Chem.* **177**, 3660 (2004).

[106] T. Takahashi, H. Iwahara, *J. Appl. Electrochem.* **3**, 65 (1973).

[107] T. Takahashi, T. Esaka, H. Iwahara, *J. Appl. Electrochem.* **7**, 31 (1977).

[108] C. D. Ling, R. L. Withers, J. G. Thompson, S. Schmid, *Acta Crys.* **B55**, 306 (1999).

[109] S. A. Warda, W. Pietzuch, W. Massa, U. Kesper, D. Reinen, *J. Solid State Chem.* **149**, 209 (2000).

[110] A. Watanabe, N. Ishizawa, M. Kato, *J. Solid State Chem.* **60**, 252 (1985).

[111] M. G. Francesconi, A. L. Kirbyshire, C. Greaves, O. Richard, G. van Tendeloo, *Chem. Mater.* **10**, 626 (1998).

[112] V. I. Smirnov, V. G. Ponomareva, Y. M. Yukhin, N. F. Uvarov, *Solid State Ionics* **156**, 79 (2003).

[113] T. E. Crumpton, C. Greaves, *J. Mater. Chem.* **14**, 2433 (2004).

[114] T. E. Crumpton, J. F. W. Mosselmans, C. Greaves, *J. Mater. Chem.* **15**, 164 (2005).

[115] N. Cormack, R. M. Jones, P. W. Tasker, C. R. A. Catlow, *J. Solid State Chem.* **44**, 174 (1982).

[116] H. Iwahara, *Solid State Ionics* **53-6**, 575 (1992).

[117] K. D. Kreuer, S. J. Paddison, E. Spohr, M. Schuster, *Chem. Rev.* **104**, 4637 (2004).

[118] T. Norby, M. Wideroe, R. Glockner, Y. Larring, *Dalton Trans.* **19**, 3012 (2004).

[119] T. Norby, *MRS Bull.* **34**, 923 (2009).

[120] K. D. Kreuer, S. Adams, W. Munch, A. Fuchs, U. Klock, J. Maier, *Solid State Ionics* **145**, 295 (2001).

[121] S. M. Haile, G. Staneff, K. H. Ryu, *J. Mater. Sci.* **36**, 1149 (2001).

[122] H. G. Bohn, T. Schober, *J. Am. Cer. Soc.* **83**, 768 (2000).

[123] I. Ahmed, C. S. Knee, M. Karlsson, S.-G. Eriksson, P. F. Henry, A. Matic, D. Engberg, L. Borjesson, *J. Alloys Comp.* **450**, 103 (2008).

[124] I. Ahmed, M. Karlsson, S.-G. Eriksson, E. Ahlberg, C. S. Knee, K. Larsson, A. K. Azad, A. Matic, L. Borjesson, *J. Am. Cer. Soc.* **91**, 3039 (2008).

[125] I. Ahmed, S.-G. Eriksson, E. Ahlberg, C. S. Knee, H. Gotlind, L.-G. Johansson, M. Karlsson, A. Matic, L. Borjesson, *Solid State Ionics* **178**, 515 (2007).

[126] M. Karlsson, D. Engberg, M. E. Bjorketun, A. Matic, G. Wahnstrom, P. G. Sundell, P. Berastegui, I. Ahmed, P. Falus, B. Farago, L. Borjesson, S. Eriksson, *Chem. Mater.* **22**, 740 (2010).

[127] S. B. C. Duval, P. Holtappels, U. Stimming, T. Graule, *Solid State Ionics* **179**, 1112 (2008).

[128] N. Ito, H. Matsumoto, Y. Kawasaki, S. Okada, T. Ishihara, *Solid State Ionics* **179**, 324 (2008).

[129] M. Karlsson, A. Matic, C. S. Knee, I. Ahmed, S.-G. Eriksson, L. Borjesson, *Chem. Mater.* **20**, 3480 (2008).

[130] I. Antunes, A. Brandao, F. M. Figueiredo, J. R. Frade, J. Gracio, D. P. Fagg, *J. Solid State Chem.* **182**, 2149 (2009).

[131] M. Karlsson, A. Matic, D. Engberg, M. E. Bjorketun, M. M. Koza, I. Ahmed, G. Wahnstrom, L. Borjesson, S.-G. Eriksson, *Solid State Ionics* **180**, 22 (2009).

[132] F. Giannici, A. Longo, A. Balerna, K. D. Kreuer, A. Martorana, *Chem. Mater.* **21**, 2641 (2009).

[133] P. Babilo, T. Uda, S. M. Haile, *J. Mater. Res.* **22**, 1322 (2007).

[134] P. Babilo, S. M. Haile, *J. Am. Cer. Soc.* **88**, 2362 (2005).

[135] Y. Yamazaki, P. Babilo, S. Haile, *Chem. Mater.* **20**, 6352 (2008).

[136] Y. Yamazaki, R. Hernandez-Sanchez, S. M. Haile, *Chem. Mater.* **21**, 2755 (2009).

[137] J. H. Shim, J. S. Park, J. An, T. M. Gur, S. Kang, F. B. Prinz, *Chem. Mater.* **21**, 3290 (2009).

[138] S. Zhang, L. Bi, L. Zhang, Z. Tao, W. Sun, H. Wang, W. Liu, *J. Power Sources* **188**, 343 (2009).

[139] J. R. Tolchard, T. Grande, *Solid State Ionics* **178**, 593 (2007).

[140] S. Tao, J. T. S. Irvine, *J. Solid State Chem.* **180**, 3493 (2007).

[141] A. K. Azad, C. Savaniu, S. Tao, S. Duval, P. Holtappels, R. M. Ibberson, J. T. S. Irvine, *J. Mater. Chem.* **18**, 3414 (2008).

[142] A. S. Patnaik, A. V. Virkar, *J. Electrochem. Soc.* **153**, A1397 (2006).

[143] K. D. Kreuer, *Solid State Ionics* **125**, 285 (1999).

[144] W. Munch, G. Seifert, K. D. Kreuer, J. Maier, *Solid State Ionics* **97**, 39 (1997).

[145] M. E. Bjorketun, P. G. Sundell, G. Wahnstrom, *Phys. Rev. B* **76**, 054307 (2007).

[146] B. Merinov, W. A. Goddard, *J. Chem. Phys.* **130**, 194707 (2009).

[147] M. E. Bjorketun, P. G. Sundell, G. Wahnstrom, *Faraday Discussions* **134**, 247 (2007).

[148] P. G. Sundell, M. E. Bjorketun, G. Wahnstrom, *Phys. Rev. B* **76**, 094301 (2007).

[149] P. G. Sundell, M. E. Bjorketun, G. Wahnstrom, *Phys. Rev. B* **73**, 104112 (2006).

[150] Q. Zhang, G. Wahnstrom, M. E. Bjorketun, S. Gao, E. Wang, *Phys. Rev. Lett.* **101**, 215902 (2008).

[151] K. A. Furoy, R. Haugsrud, M. Hansel, A. Magraso, T. Norby, *Solid State Ionics* **178**, 461 (2007).

[152] C. Y. Jones, J. Wu, L. P. Li, S. M. Haile, *J. Appl. Phys.* **97**, 114908 (2005).

[153] T. Fukui, S. Ohara, S. Kawatsu, *J. Power Sources* **71**, 164 (1998).

[154] C. S. Knee, A. Magraso, T. Norby, R. I. Smith, *J. Mater. Chem.* **19**, 3238 (2009).

[155] A. Magraso, A. Calleja, X. G. Capdevila, F. Espiell, *Solid State Ionics* **166**, 359 (2004).

[156] A. Magraso, F. Espiell, M. Segarra, J. T. S. Irvine, *J. Power Sources* **169**, 53 (2007).

[157] S. Mimuro, S. Shibako, Y. Oyama, K. Kobayashi, T. Higuchi, S. Shin, S. Yamaguchi, *Solid State Ionics* **178**, 641 (2007).

[158] A. Magraso, R. Haugsrud, M. Segarra, T. Norby, *J. Electroceram.* **23**, 80 (2009).

[159] P. J. Saines, B. J. Kennedy, R. I. Smith, *Mater. Res. Bull.* **44**, 874 (2009).

[160] G. V. Lewis, C. R. A. Catlow, *J. Phys. C* **18**, 1149 (1985).

[161] M. S. Khan, M. S. Islam, D. R. Bates, *J. Mater. Chem.* **8**, 2299 (1998).

[162] G. Balducci, M. S. Islam, J. Kaspar, P. Fornasiero, M. Graziani, *Chem. Mater.* **12**, 677 (2000).

[163] P. Saul, C. R. A. Catlow, *Phil. Mag. B* **51**, 107 (1985).

[164] K. P. Schroder, J. Sauer, M. Leslie, C. R. A. Catlow, J. M. Thomas, *Chem. Phys. Lett.* **188**, 320 (1992).

[165] R. A. Davies, M. S. Islam, J. D. Gale, *Solid State Ionics* **126**, 323 (1999).

[166] R. Glockner, M. S. Islam, T. Norby, *Solid State Ionics* **122**, 145 (1999).

[167] M. S. Islam, R. A. Davies, C. A. J. Fisher, A. V. Chadwick, *Solid State Ionics* **145**, 333 (2001).

[168] G. C. Mather, M. S. Islam, *Chem. Mater.* **17**, 1736 (2005).

[169] P. Panchmatia, A. Orera, J. Hanna, M. E. Smith, P. R. Slater, M. S. Islam, *J. Mater. Chem.* **20**, 2766 (2010).

[170] Y. Hinatsu, *J. Solid State Chem.* **122**, 384 (1996).

[171] A. J. Jacobson, B. Tofield, B. E. F. Fender, *Acta Crys.* **B28**, 956 (1972).

[172] T. Nakamura, *Chem. Lett.* **5**, 429 (1974).

[173] R. D. Shannon, *Acta Crys.* **A32**, 751 (1976).

[174] T. Tsuji, N. Miyajima, M. Ochida, *Solid State Ionics* **79**, 183 (1995).

[175] T. Tsuji, T. Suzuki, H. Iwahara, *Solid State Ionics* **70**, 291 (1994).

[176] M. S. Islam, R. A. Davies, J. D. Gale, *Chem. Mater.* **13**, 2049 (2001).

[177] K. Wright, R. Freer, C. R. A. Catlow, *Phys. Chem. Miner.* **20**, 500 (1995).

[178] C. R. A. Catlow, *J. Phys. Chem. Solids* **28**, 1131 (1977).

[179] M. S. Islam, R. A. Davies, *J. Mater. Chem.* **14**, 86 (2004).

[180] C. Karmonik, T. J. Udovic, R. L. Paul, J. J. Rush, K. Lind, R. Hempelmann, *Solid State Ionics* **109**, 207 (1998).

[181] R. Hempelmann, M. Soetratmo, O. Hartmann, R. Wappling, *Solid State Ionics* **107**, 269 (1998).

[182] W. G. Coors, *J. Power Sources* **118**, 150 (2003).

[183] M. S. Islam, *J. Mater. Chem.* **10**, 1027 (2000).

[184] M. S. Islam, P. R. Slater, *MRS Bull.* **34**, 935 (2009).

[185] M. Yashima, *Solid State Ionics* **179**, 797 (2008).

[186] N. A. Spaldin, M. Fiebig, *Science* **309**, 391 (2005).

[187] W. Eerenstein, N. D. Mathur, J. F. Scott, *Nature* **442**, 759 (2006).

[188] R. Ramesh, N. A. Spaldin, *Nature Mater.* **6**, 21 (2007).

[189] S.-W. Cheong, M. Mostovoy, *Nature Mater.* **6**, 13 (2007).

[190] X. Qi, J. Dho, R. Tomov, M. G. Blamire, J. L. MacManus-Driscoll, *App. Phys. Lett.* **86**, 062903 (2005).

[191] A. M. dos Santos, S. Parashar, A. R. Raju, Y. S. Zhao, A. K. Cheetham, C. N. R. Rao, *Solid State Comm.* **122**, 49 (2002).

[192] T. Kimura, T. Goto, H. Shintani, K. Ishizaka, T. Arima, Y. Tokura, *Nature* **426**, 55 (2003).

[193] M. Fiebig, T. Lottermoser, D. Frohlich, A. V. Goltsev, R. V. Pisarev, *Nature* **419**, 818 (2002).

[194] J. Wang, J. B. Neaton, H. Zheng, V. Nagarajan, S. B. Ogale, B. Liu, D. Viehland, V. Vaithyanathan, D. G. Schlom, U. V. Waghmare, N. A. Spaldin, K. M. Rabe, M. Wuttig, R. Ramesh, *Science* **299**, 1719 (2003).

[195] J. B. Neaton, C. Ederer, U. V. Waghmare, N. A. Spaldin, K. M. Rabe, *Phys. Rev. B* **71**, 014113 (2005).

[196] C. Ederer, N. A. Spaldin, *Phys. Rev. B* **71**, 224103 (2005).

[197] I. Vrejoiu, M. Alexe, D. Hesse, U. Gosele, *Adv. Fun. Mater.* **18**, 3892 (2008).

[198] J. Seidel, L. W. Martin, Q. He, Q. Zhan, Y. H. Chu, A. Rother, M. E. Hawkridge, P. Maksymovych, P. Yu, M. Gajek, N. Balke, S. V. Kalinin, S. Gemming, F. Wang, G. Catalan, J. F. Scott, N. A. Spaldin, J. Orenstein, R. Ramesh, *Nature Mater.* **8**, 229 (2009).

[199] C.-H. Yang, J. Seidel, S. Y. Kim, P. B. Rossen, P. Yu, M. Gajek, Y. H. Chu, L. W. Martin, M. B. Holcomb, Q. He, P. Maksymovych, N. Balke, S. V. Kalinin, A. B. Baddorf, S. R. Basu, M. L. Scullin, R. Ramesh, *Nature Mater.* **8**, 485 (2009).

[200] Y.-H. Chu, L. W. Martin, M. B. Holcomb, M. Gajek, S.-J. Han, Q. He, N. Balke, C.-H. Yang, D. Lee, W. Hu, Q. Zhan, P.-L. Yang, A. Fraile-Rodriguez, A. Scholl, S. X. Wang, R. Ramesh, *Nature Mater.* **7**, 478 (2008).

[201] P. Kharel, S. Talebi, B. Ramachandran, A. Dixit, V. M. Naik, M. B. Sahana, M. S. R. Rao, G. Lawes, *J. Phys.: Condens. Matter* **21**, 036001 (2009).

[202] K. Brinkman, T. IiJima, H. Takamura, *Jap. J. Appl. Phys.* **46**, L93 (2007).

[203] Y. K. Jun, S. B. Lee, M. Kim, S. H. Hong, *J. Mater. Res.* **22**, 3397 (2007).

[204] V. A. Murashav, D. N. Rakov, V. M. Ionov, L. S. Dubenko, Y. U. Titov, *Ferroelectrics* **162**, 11 (1994).

[205] Y. F. Popov, A. M. Kadomtseva, G. P. Vorobev, A. K. Zvezdin, *Ferroelectrics* **162**, 135 (1994).

[206] D. Lebeugle, D. Colson, A. Forget, M. Viret, *App. Phys. Lett.* **91**, 022907 (2007).

[207] M. Li, J. L. MacManus-Driscoll, *App. Phys. Lett.* **87**, 252510 (2005).

[208] J. Wang, A. Scholl, H. Zheng, S. Ogale, D. Viehland, D. Schlom, N. Spaldin, K. Rabe, M. Wuttig, L. Mohaddes, J. Neaton, U. Waghmare, T. Zhao, R. Ramesh, *Science* **307** (2005).

[209] C.-F. Chung, J.-P. Lin, J.-M. Wu, *App. Phys. Lett.* **88**, 242909 (2006).

[210] J. M. Moreau, C. Michel, R. Gerson, W. J. James, *J. Phys. Chem. Solids* **32**, 1315 (1971).

[211] F. Kubel, H. Schmid, *Acta Crys. B* **46**, 698 (1990).

[212] F. A. Kröger, *The Chemistry of Imperfect Crystals* (Interscience (Wiley), 1974).

[213] A. Jones, M. S. Islam, *J. Phys. Chem. C* **112**, 4455 (2008).

[214] C. Tealdi, L. Malavasi, C. A. J. Fisher, M. S. Islam, *J. Phys. Chem. B* **110**, 5395 (2006).

[215] A. Chainani, M. Mathew, D. D. Sarma, *Phys. Rev. B* **48**, 14818 (1993).

[216] M. Abbate, F. M. F. Degroot, J. C. Fuggle, A. Fujimori, O. Strebel, F. Lopez, M. Domke, G. Kaindl, G. A. Sawatzky, M. Takano, Y. Takeda, H. Eisaki, S. Uchida, *Phys. Rev. B* **46**, 4511 (1992).

[217] C. L. Chang, G. Chern, M. F. Tai, Y. W. Su, C. L. Dong, S. Y. Liu, C. S. Hwang, P. K. Tseng, *Jpn. J. Appl. Phys., Part 1* **38**, 108 (1999).

[218] W. H. Jung, E. Iguchi, *J. Phys.: Condens. Matter* **7**, 1215 (1995).

[219] H. Naganuma, J. Miura, S. Okamura, *App. Phys. Lett.* **93**, 052901 (2008).

[220] H. Uchida, R. Ueno, H. Funakubo, S. Koda, *J. Appl. Phys.* **100**, 014106 (2006).

[221] Y. Wang, R. Y. Zheng, C. H. Sim, J. Wang, *J. Appl. Phys.* **105**, 016106 (2009).

[222] G. L. Yuan, S. W. Or, *App. Phys. Lett.* **88**, 062905 (2006).

[223] M. Azuma, H. Kanda, A. A. Belik, Y. Shimakawa, M. Takano, *J. Magn. Magn. Mater.* **310**, 1177 (2007).

[224] M. S. Islam, *Solid State Ionics* **154**, 75 (2002).

[225] M. Lerch, H. Boysen, T. Hansen, *J. Phys. Chem. Solids* **62**, 444 (2001).

[226] A. K. Cheetham, A. R. Rae Smith, *Acta Crys.* **B41**, 225 (1985).

[227] J. R. Tolchard, M. S. Islam, P. R. Slater, *J. Mater. Chem.* **13**, 1956 (2003).

[228] G. M. Freeman, C. R. A. Catlow, *J. Solid State Chem.* **85**, 65 (1990).

[229] C. A. J. Fisher, V. M. H. Prieto, M. S. Islam, *Chem. Mater.* **20**, 5907 (2008).

[230] C. Pirovano, M. S. Islam, R. N. Vannier, G. Nowogrocki, G. Mairesse, *Solid State Ionics* **140**, 115 (2001).

[231] M. S. D. Read, M. S. Islam, G. W. Watson, F. E. Hancock, *J. Mater. Chem.* **11**, 2597 (2001).

[232] C. A. J. Fisher, M. Islam, R. J. Brook, *J. Solid State Chem.* **128**, 137 (1997).

[233] M. Cherry, M. S. Islam, J. D. Gale, C. R. A. Catlow, *J. Phys. Chem.* **99**, 14614 (1995).

[234] R. C. Baetzold, *Phys. Rev. B* **48**, 5789 (1993).

[235] H. Donnerberg, M. Exner, C. R. A. Catlow, *Phys. Rev. B* **47**, 14 (1993).